Exploring the Moon in the Thermal Infrared: The Space Environment Goniometer

Tristram Warren

Hertford College

University of Oxford

A thesis submitted for the degree

Doctor of Philosophy

Trinity 2015

Exploring the Moon in the Thermal Infrared: The Space Environment Goniometer

Thesis submitted for the degree of Doctor of Philosophy in the University of Oxford.

Abstract

Measurements of the light scattering behaviour of the regolith of airless bodies in the Solar System, across wavelengths from the visible to the far infrared are essential to understanding their physical properties. This thesis describes the design, build and calibration of a novel instrument to measure the angular directionality of thermal infrared emission from surfaces (direction emissivity, DE). This work was originally motivated by the need for new DE measurements to support analysis of data collected by the thermal and far infrared Diviner Lunar Radiometer instrument (8 – 400 μm) currently in orbit around the Moon.

To fully interpret the brightness temperatures measured by the Diviner instrument a three dimensional thermal physical model is required. These models typically assume that infrared radiation is scattered isotropically from the lunar surface. Although generally the models are in very good agreement with Diviners measured brightness temperatures, there are some discrepancies particularly in permanently shadowed regions near the lunar poles. One possible reason for these discrepancies is that the thermal infrared DE of the lunar surface is not isotropic as is typically assumed by many of these models. The “Oxford Space Environment Goniometer” (OSEG) was developed to measure the DE of surface across wavelengths from the visible to the thermal and far infrared.

Analysis and modelling of initial DE measurements made with the OSEG show that the DE is dependent on the optical properties and roughness of the surface. DE measurements of the lunar regolith analogue material JSC-1AF have been incorporated into a three dimensional thermal physical model to show that the predicted surface temperatures of a polar lunar-like permanently shadowed region can differ by 10 K compared to assuming an isotropic DE.

Tristram Warren

Hertford College

Trinity Term 2015

Acknowledgements

I would firstly like to thank my supervisor Dr Neil Bowles for allowing me the opportunity to carry out this project, I will never be able to thank him enough for his help and guidance over the last four years. I am also incredibly grateful to Dr Ian Thomas for his help and wisdom whilst showing me the ropes during the earlier phases of the project. Thanks to Andy Clack and Jon Temple in the electronic workshop for fixing all my mistakes during the last four years and for their help and support in the design and construction of the project.

Many thanks to both Dr Kerri Donaldson Hanna and Dr Jessica Arnold for reading and commenting on drafts of this thesis. I will forever be indebted to all the group members including Ian, Kerri and Jessy for attending the Friday morning group meetings and keeping Neil to less than two hours of ranting.

I would like to thank all my friends for their support. In particular Tom for letting me win when we played sport and Kate for games nights. An absolutely massive thanks must go to Jenna for all her hard work in helping me write this thesis despite the fact I have no idea what an RNA drosophila fly is.

I also owe a big thanks to Dr Becky Parker, I feel that I might be the start of a small army of PhD graduates who she has helped inspire to pursue research.

Finally, I would like to thank my parents, whom I hope already know how grateful I am for everything they have done for me not just over the last four years of this project, but the last quarter of a century.

Table of Contents

1 Introduction

1.1 The Lunar Thermal Environment

The Moon is Earth's largest natural satellite. Having a lower density (3.341 g/cm^3 (Pieth & Kohler 2009)) and radius (1737.4 km) than the Earth, the Moon's gravity is approximately one sixth that of the Earth's. As a result the Moon is unable to retain an appreciable atmosphere. The surface of the Moon is covered in a very fine (10 – 100 μm (Hapke 1968)) powdered soil known as regolith (Figure 1). The regolith is believed to have formed over billions of years, as the Moon's surface is constantly bombarded with meteorites, micrometeorites and space debris, a process known as 'impact gardening' (McKay et al. 1991). This bombardment process has slowly broken down the lunar bedrock into the regolith observed today. Due to the lack of atmospheric erosion processes on the Moon (e.g. water and wind) the individual grains that make up the regolith have a very 'pointy' structure. This combined with the low gravity of the Moon results in the regolith being highly porous and is often referred to as having a "fairy castle" structure (Figure 1) (Hapke & Van Horn 1963; Hapke 1964). This structure means individual grains of the regolith make very little contact with one another and therefore the lunar regolith has a very low thermal conductivity, of the order 1.5×10^{-3} W/mK (Keihm & Langseth 1973).

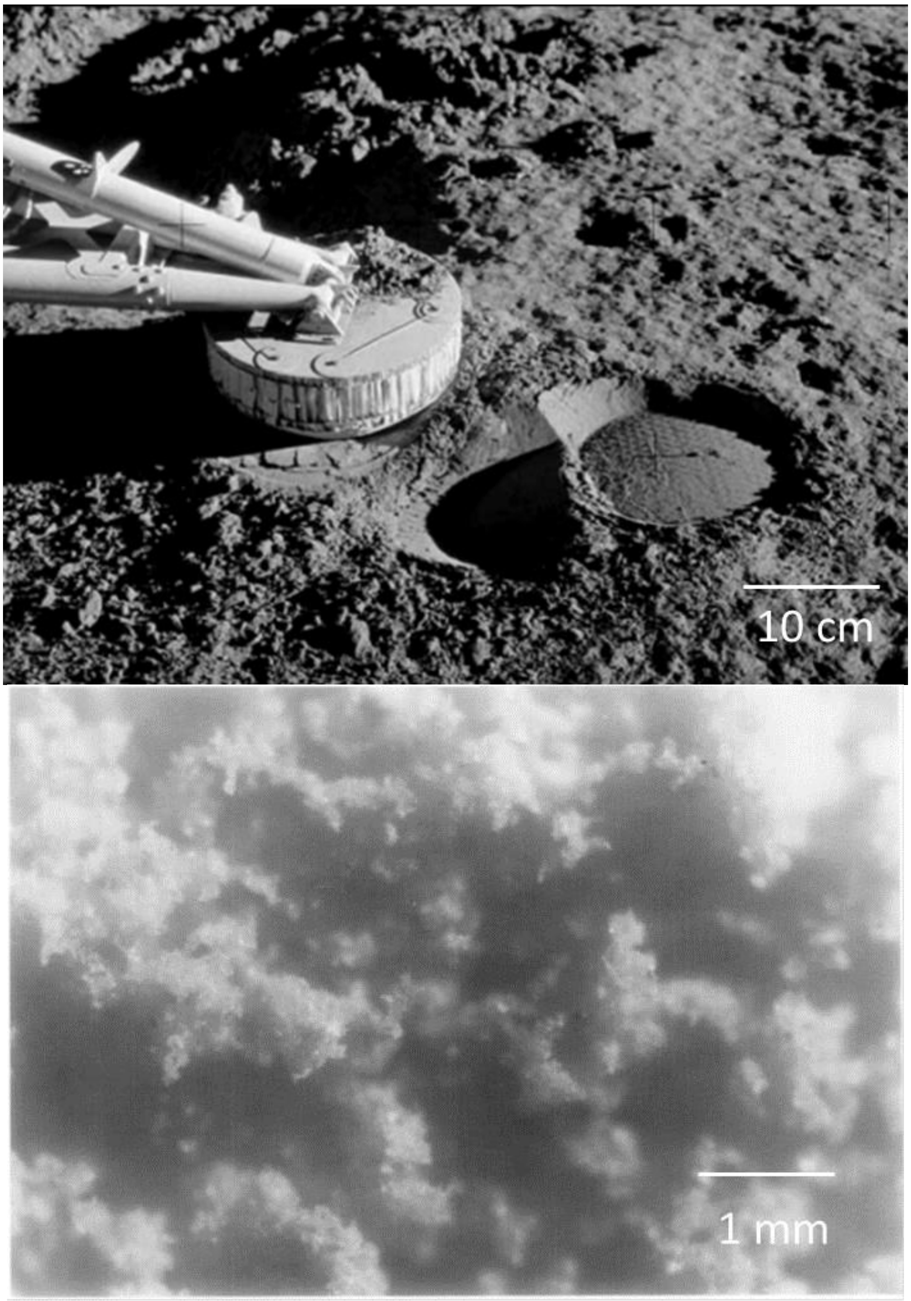

Figure 1: (Top) Surveyor-3 mission photograph taken on the surface of the Moon, showing the fluffy top soil of the Moon known as regolith (Credit NASA). (Bottom) Example of a "fairy castle" structure similar to that found on the lunar surface. After (Salisbury & Wald 1992)

The low thermal conductivity of the lunar regolith and the lack of interstitial atmospheric gases between regolith grains mean radiation is the dominant mode of heat transport in the lunar regolith. This sets up a unique and complex thermal environment at the surface and subsurface of the Moon, where huge (>100 K) thermal gradients can exist between areas of the Moon in shadow and areas in direct sunlight. The lunar thermal environment can be split into three distinct regimes: daytime, night-time and polar regions (>80^{o} latitude). The surface temperatures in each distinct regime are controlled by a different physical process:

1. Daytime temperatures are controlled by the flux of the incoming solar radiation.
2. The night-time thermal environment is controlled by the cooling rate of lunar rocks and regolith.
3. Temperatures in the polar regions are controlled by the local topography.

1.1.1 The Lunar Daytime Thermal Environment

When the surface of the Moon is illuminated during the daytime, the surface temperature is controlled by the flux of the solar radiation. At low latitudes (<80^{o}) the illuminated surfaces of the Moon are heated for the entire length of the lunar day (approximately 14 Earth days) and therefore reach temperatures of approximately 400 K. The simple model shown in Figure 2 illustrates that the latitudinal and diurnal variation in lunar daytime temperatures is almost completely controlled by the angular distance to the sub-solar point, i.e. by the amount of solar flux received by the surface (Vasavada et al. 2012). The Vasavada et al. (1999) model (Figure 2) qualitatively agrees with surface temperature measurements (Figure 3) made by the Diviner Lunar Radiometer Experiment (further described in section 2.1).

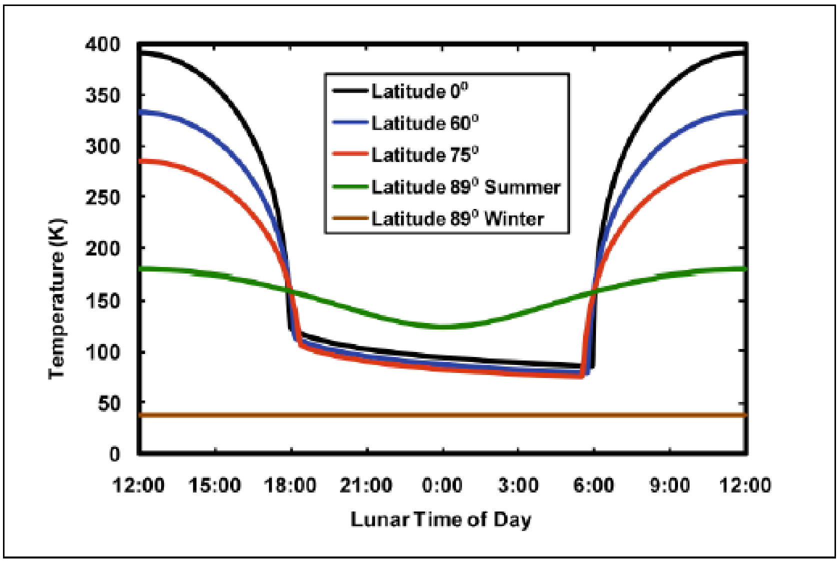

Figure 2: Model calculations of lunar surface temperature variations as a function of local time and latitude. Local time is expressed in hours, which correspond to 1/24 of a lunar month. Taken from (Vasavada et al. 1999).

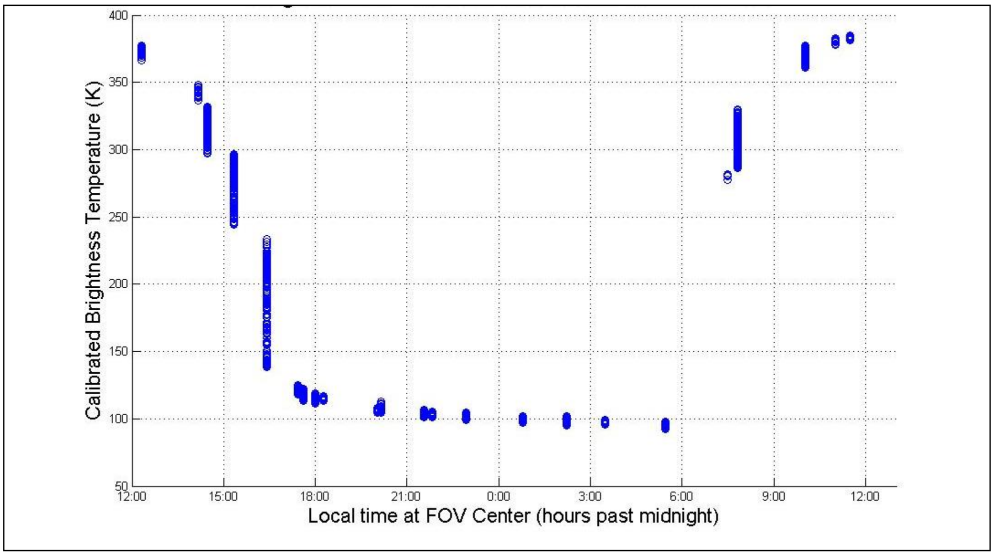

Figure 3: Diviner Channel Seven brightness temperature data for a latitude of 79.2°. Brightness temperature data downloaded from NASA's Planetary Data System (PDS http://pds.nasa.gov/) demonstrate the daytime surface temperature of the Moon is a function of the sub-solar point at one point on the lunar surface.

1.1.2 The Lunar Night-time Thermal Environment

The lunar surface during night-time is one of extreme cold (<100 K). With no oceans or appreciable atmosphere to buffer temperatures, the only heat source to balance the loss of thermal radiation to space during the 14 Earth day lunar night is the heat stored in the lunar subsurface. However, the low thermal conductivity of the lunar soil greatly reduces the heat flow from the subsurface to the surface. This sets up a large temperature gradient (Figure 4) in the lunar soil between the surface and the sub-surface.

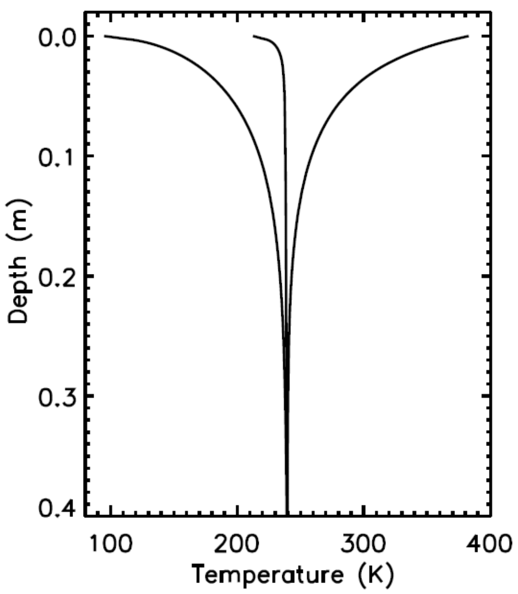

Figure 4: Model calculated minimum (left curve), average (middle curve) and maximum (right curve) sub-surface temperatures of the lunar surface, showing a large thermal gradient between the surface and the sub-surface. These depth profiles are for the lunar equator and were calculated using a 3D thermal physical model assuming an average bulk density of 1600 kg/m^3 and conductivity of 0.004 W/m/K. Taken from Vasavada et al. (2012).

1.1.3 The Lunar Pole Thermal Environment

The obliquity angle of an object is the angle between an object's rotational axis and its orbital axis (Figure 5). Compared to the Earth's obliquity angle of 23^o, the Moon has a very small obliquity angle of 1.53^o (Ward 1975). As a consequence the incidence angle of solar light at the lunar poles is very oblique; the incoming rays of sunlight are almost parallel to the ground. Subsequently, the thermal environment at the poles is driven by the local topography. At the lunar poles depending on the exact topography some crater rims on the surface cast shadows, hiding the base of craters from direct sunlight (Figure 6). The crater bases are therefore in permanent darkness and are known as Permanent Shadowed Regions (PSRs) (Watson et al. 1961; Arnold 1979). PSRs have been imaged using the Wide Angle Camera (WAC) on the Lunar Reconnaissance Orbiter (LRO) spacecraft (Figure 7). Permanently Illuminate Regions (PIRs) can also exist, such as crater rims that are always in direct sunlight.

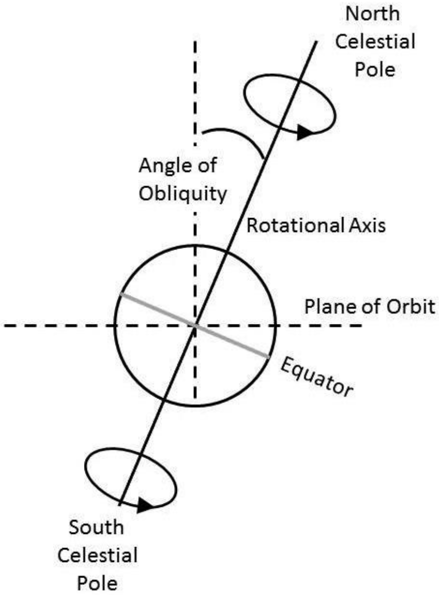

Figure 5: Definition of obliquity angle.

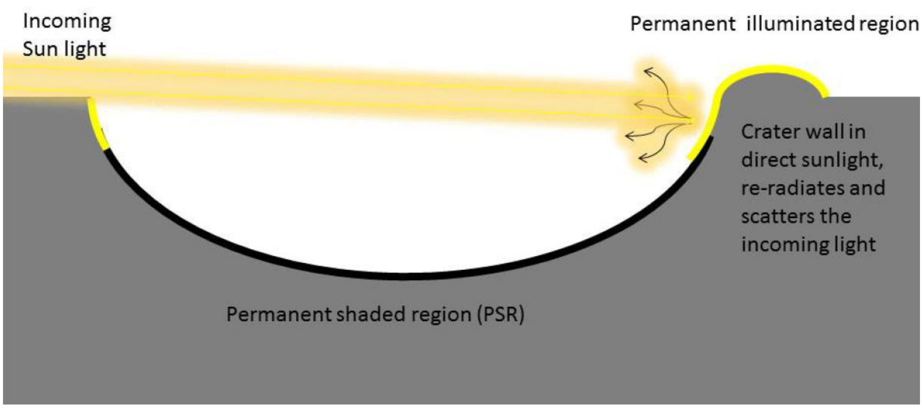

Figure 6: Schematic showing an imaginary bowl shaped crater at a lunar pole to illustrate how PSR and PIR are formed. Some craters at the lunar poles do not see direct sunlight as the incoming solar radiation is almost

parallel to the ground. The only radiation seen by the base of the crater in the schematic is from scattered radiation from the crater walls.

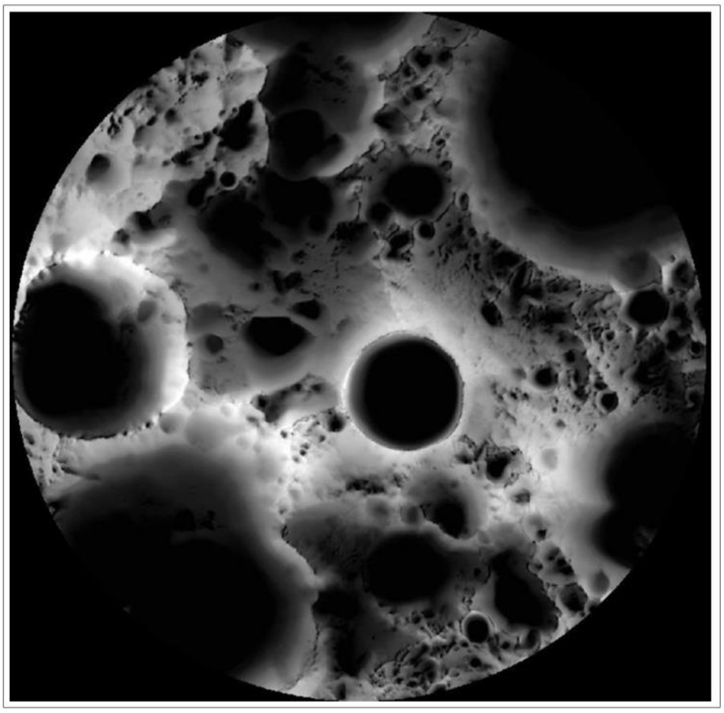

Figure 7: A multi-temporal illumination map of the lunar South Pole. Produced using data from the Wide Angle Camera (WAC) on the Lunar Reconnaissance Orbiter spacecraft by collecting 1700 images over six lunar days covering the same area. Each image was map projected and converted to a binary image (if the ground was illuminated that pixel was set to one and if shadowed zero) to differentiate between sunlit and shadowed regions. All the binary images were then stacked. For each pixel it was determined what percentage of time during the six months that spot was illuminated. Shackleton crater (19km diameter) is in the centre, the South Pole is located approximately at 9 o'clock on its rim. Mapped area extends from 88^{o}S to 90^{o}S. Taken from (LROC team 2014).

PSRs are primarily heated by reflected solar and re-radiated thermal infrared radiation from distant crater walls that are in direct sunlight, with a smaller contribution from the geothermal heat from the Moon's interior. Models and measurements (described in more detail in section 1.3) have shown the temperature range in these PSRs to be extremely cold <100 K (Vasavada et al. 1999). PSRs can be seen in maps of maximum brightness temperature of the North and South Pole as observed by the Diviner radiometer (Figure 8 and Figure 9) (Diviner instrument is described in section 1.2).

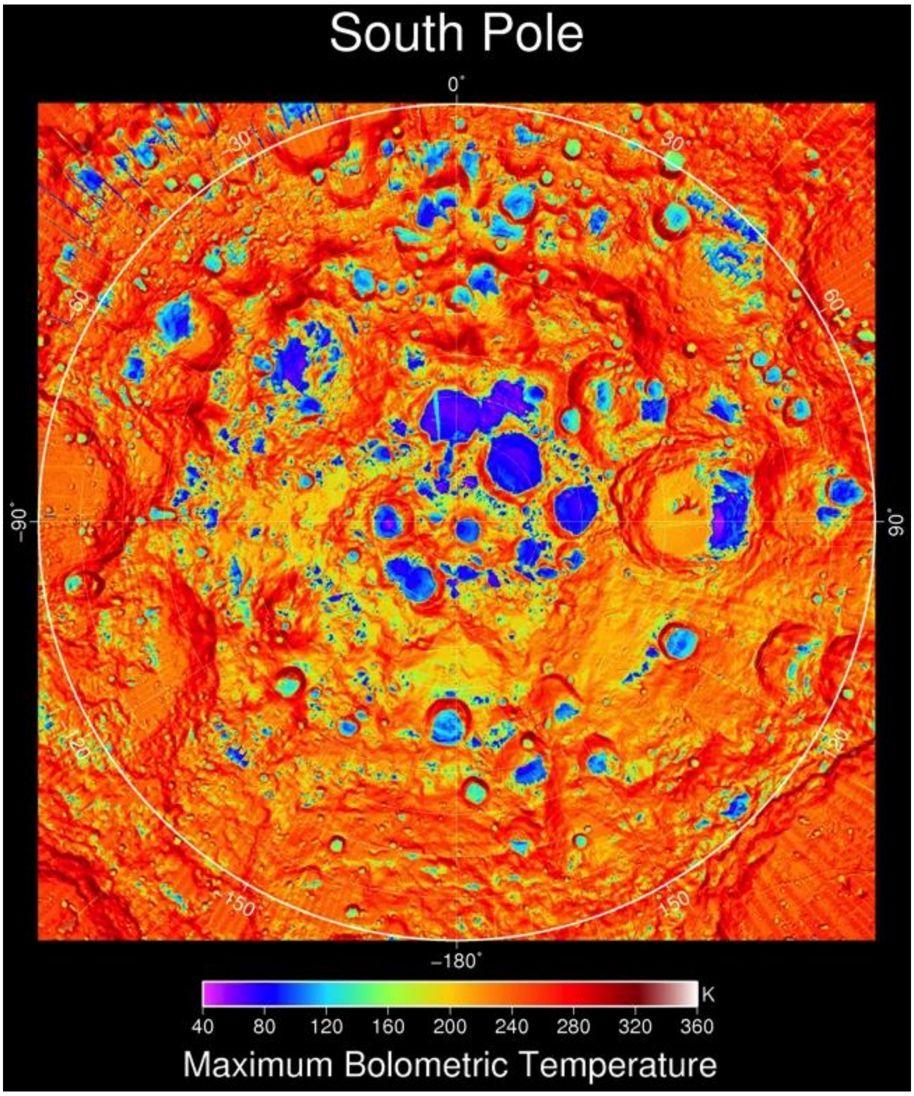

Figure 8: Maximum daytime temperature of the lunar South Pole as measured by Diviner. PSRs can clearly be seen as blue and purple regions as their maximum surface temperatures are less than 100 K (Paige 2015).

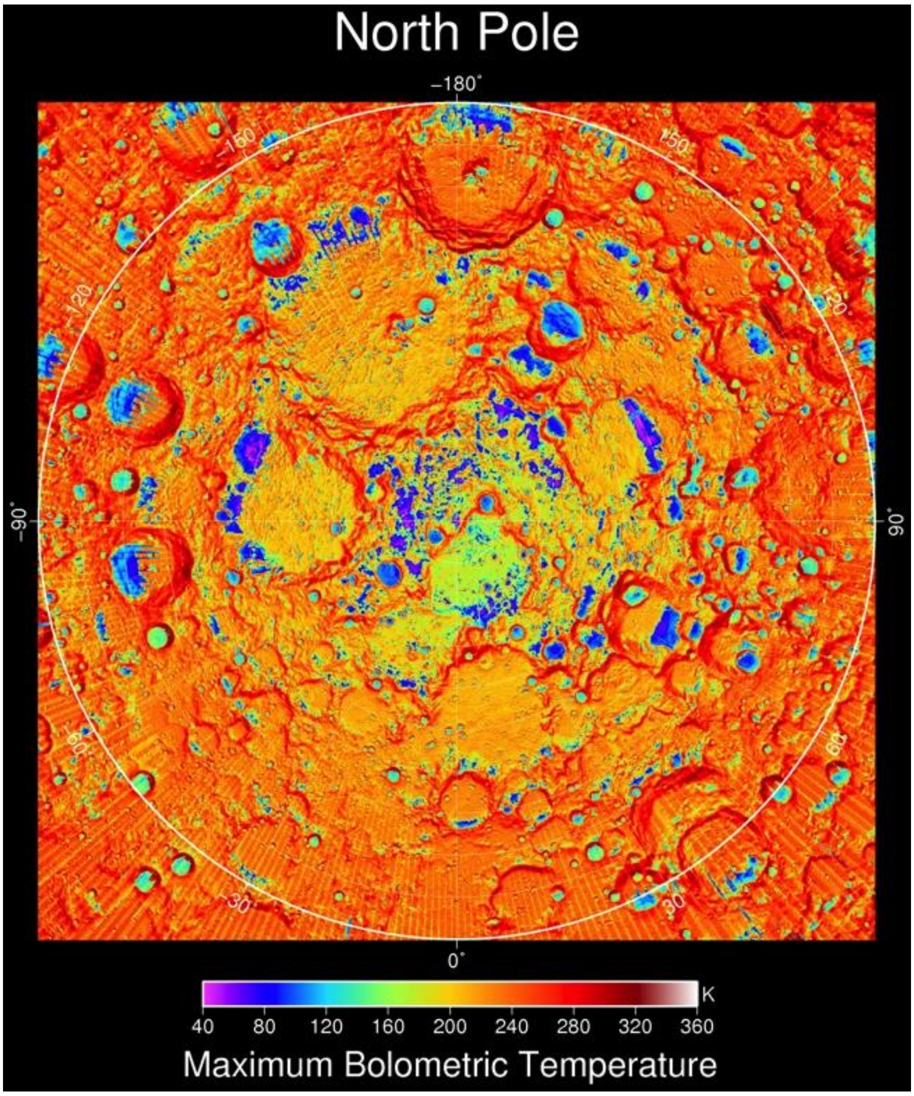

Figure 9: Maximum daytime temperature of the lunar North Pole as measured by Diviner. PSR can clearly be seen as blue and purple regions as their maximum surface temperatures are less than 100 K (Paige 2015).

1.1.4 Lunar Cold Traps

A Jeans atmospheric escape calculation shows that for water-ice to be permanently trapped on the lunar surface the temperature must not exceed 112 K (Figure 10). At temperatures greater than 112 K the thermal velocity of the molecules will be too large to be retained by the Moon’s gravity and will escape the surface (Arnold 1979). Therefore, at the poles of the Moon it is possible water could be trapped either on the surface or in the sub-surface. Water-ice and other volatiles are speculated to have been delivered to the lunar surface by comets, meteorites and planetary outgassing. Such water molecules could have migrated to the poles of the Moon and still be trapped there today (Watson et al. 1961; Siegler et al. 2011). The presence of cold-trapped water ice and other volatiles at the lunar poles would have very important implications for our understanding of the volatile history of the Moon and the Solar System. Beyond the scientifically intriguing aspects, deposits of ice on the Moon could have many practical aspects for future manned lunar exploration (Duke et al. 2006; Paige et al. 2010).

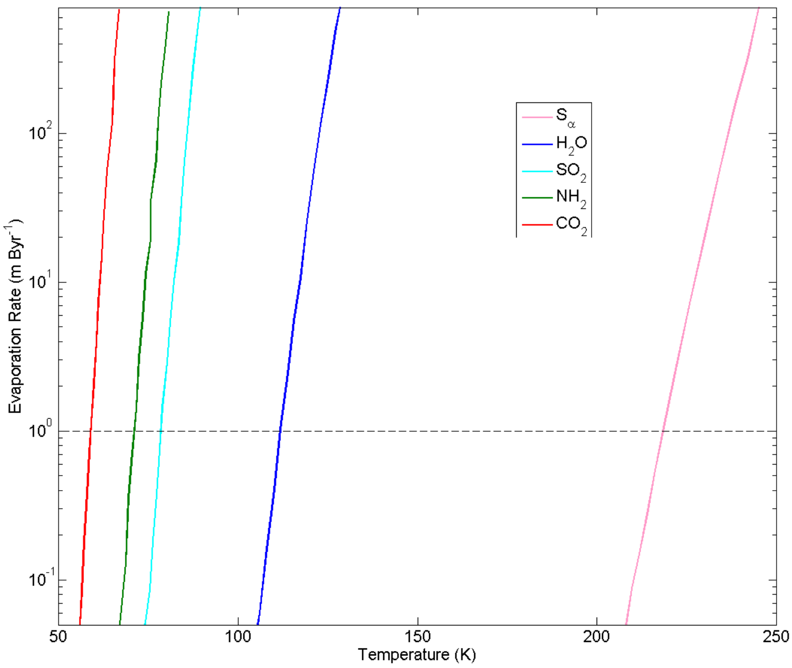

Figure 10: Evaporation rates into a vacuum as functions of temperature for CO_2, NH_3, SO_2, cubic H_2O, and S_α (solid orthorhombic sulphur) ices. Vapour pressure data were taken from (Lide 1993; Moses & Nash 1991; Bryson III et al. 1974). The calculation of evaporation rates follows Watson et al. (1961). The dashed line marks the rate at which one meter of ice would survive for one billion years. The curves cross this this line at 59, 71, 78, 112, and 218 K. This is known as a jeans escape calculation, where the possibility for escape occurs when the thermal energy of a molecule becomes greater than the gravitational potential energy. An escape flux or evaporation rate from the surface can be calculated for each molecule by assuming isothermal conditions and a Maxwellian spatial distribution. After Vasavada et al. (1999).

1.1.5 The Moon's Orbital Evolution

The amount of trapped water or ice residing in PSRs at the poles of the Moon is dependent on the past orbital evolution of the Moon as well as the delivery rate to a PSR. A past deviation in the Moon's rotational axis from the ecliptic plane by more than approximately 30^{o} would mean no large-scale PSRs could have existed at that point, and the probability of water existing in large quantities today in PSRs is significantly reduced (Siegler et al. 2011).

However, it is believed that the Moon's orbit has not changed significantly during the past billion years and as a consequence PSRs are believed to have been in permanent darkness for at least billions of years (Watson et al. 1961; Arnold 1979; Siegler et al. 2011). In order to estimate the amount of trapped water or water ice, the temperature of the lunar surface and sub-surface in PSRs must be accurately measured and modelled. The Diviner radiometer (described in the next section) is providing measurements of these regions across thermal infrared wavelengths in order to measure the surface's bolometric brightness temperature.

The bolometric brightness temperature (T_B) measured by Diviner is a measure of the spectrally integrated flux of infrared radiation emerging from the surface (equation 1). The bolometric brightness temperature is a radiometric averaged temperature of a surface that is made up of elements at different temperatures.

$$\sigma T_B^4 = \pi \int \varepsilon(\lambda) B(\lambda, T_s) d\lambda \qquad 1$$

Where σ is the Stephan Boltzmann constant, $\varepsilon(\lambda)$ is the wavelength dependent emissivity of the surface, $B(\lambda, T_s)$ is the Planck function, λ is wavelength and T_s is the surface kinetic temperature (Paige et al. 2010). Appendix 5 contains a list of all commonly used symbols in this thesis.

1.2 The Diviner Lunar Radiometer Experiment (Diviner)

The Diviner Lunar Radiometer Experiment (Figure 12) is a nine-channel, mainly nadir viewing, pushbroom mapping radiometer currently in orbit around the Moon on-board NASA's Lunar Reconnaissance Orbiter (LRO, Figure 11) (Paige et al. 2009). Diviner was launched in 2009 and spent two months in a commissioning orbit before being placed into a low (50 km) polar orbit, in order to achieve higher resolution mapping of the lunar surface. The LRO mission spent a year in this 'mapping' orbit during its first extended science mission and is currently in a highly elliptical orbit for its second extended science mission.

The precession of the LRO's polar orbit means the Diviner data set has lunar surface coverage at many different local times of day. At the time of writing, during the mapping and extended mission orbits Diviner has acquired observations over twelve complete diurnal cycles (Greenhagen. 2015). Diviner daytime and night-time observations have essentially global coverage, and more than 80% of the surface has been measured at seven or more different local times (Greenhagen 2015). The Diviner instrument has three main science and measurement objectives:

1. To characterise each different thermal regime of the lunar surface the: daytime, night-time and polar regions (>80^{o}).

2. To map PSR at the lunar poles that could be sufficiently cold to retain surface water.
3. To map the thermally derived properties of the lunar surface such as the thermal properties, rock abundance and mineralogy.

Figure 11: Photograph of NASA's Lunar Reconnaissance Orbiter, with all individual instruments labelled. Taken from Chin et al. (2007).

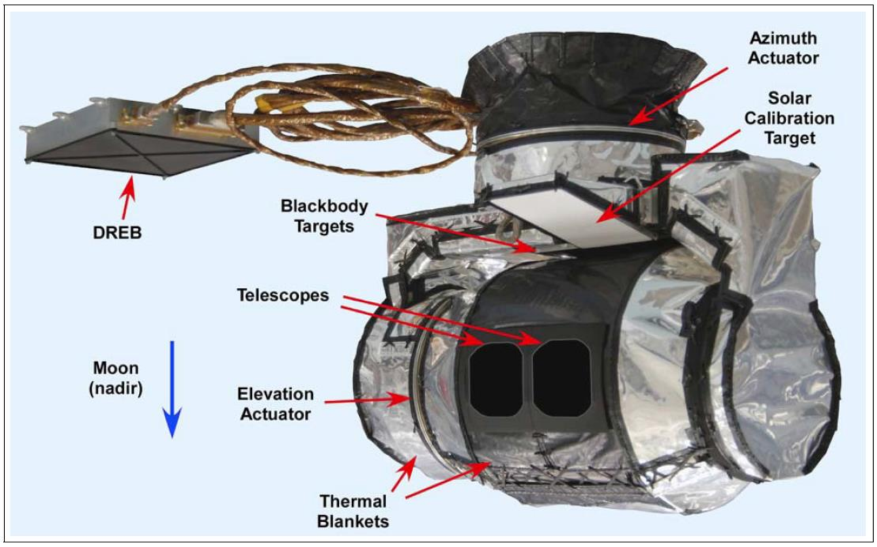

Figure 12: Diviner instrument with major components labelled. Taken from Paige et al. (2009).

To achieve these goals, Diviner has nine spectral channels (Figure 13 and Table 1) ranging from the ultraviolet/visible (0.35 µm) to the far infrared (400 µm), with two broadband solar reflectance channels across the 0.35 – 2.8 µm spectral range (Diviner channels A1 and A2), three narrow band mineralogy channels centred on 7.81, 8.28 and 8.55 µm (Diviner channels A3, A4 and A5) and four broadband thermal channels from 13 – 23, 25 – 41, 50 – 100 and 100 – 400 µm (Diviner channels A6, B1 , B2 and B3) (Paige et al. 2009).

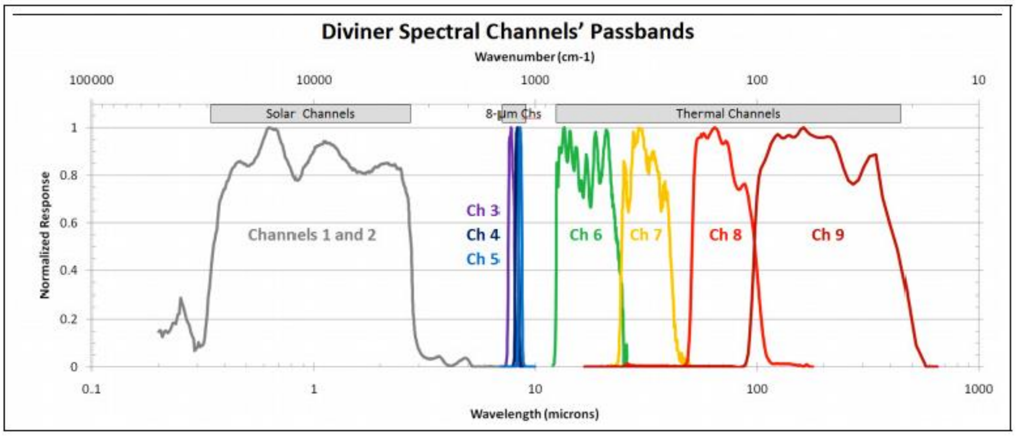

Figure 13: Diviner spectral channels' passbands. Taken from Paige et al. (2009).

Table 1: Table of Diviner channel descriptions. Taken from Paige et al. (2009)**.**

Number	Name	Wavelength (μm)	Purpose
1	A1	0.35–2.8	High Sensitivity Solar
2	A2	0.35-2.8	Mid Sensitivity Solar
3	A3	7.55-8.05	Christiansen Feature
4	A4	8.1-8.4	Christiansen Feature
5	A5	8.4-8.7	Christiansen Feature
6	A6	13-23	Thermal
7	B1	25-41	Thermal
8	B2	50-100	Thermal
9	B3	100-400	Thermal

Using the four broadband thermal channels global bolometric surface temperature maps of the lunar surface have been made at different local times of day to characterise the thermal behaviour during the daytime, night-time and at the polar regions (Paige et al. 2010). PSRs at the lunar poles have been mapped using the broadband thermal channels in detailed maximum bolometric brightness temperature maps (Figure 8 and Figure 9 in section 1.1.3). To achieve the third Diviner science objected (to map the thermally derived properties of the lunar surface) the measured bolometric surface temperatures of the lunar surface are compared to thermal physical models of the surface. Diviner was the first multispectral thermal infrared instrument to globally map the thermally derived properties of the lunar surface (Paige et al. 2010; Greenhagen et al. 2010)

1.3 Thermal Modelling of the Lunar Surface

Comparing the Diviner bolometric surface temperature measurements with the results of three-dimensional thermal physical models allows constraints to be placed on the bulk properties of the lunar surface. Such properties include surface temperature, rock abundance, surface roughness, emissivity, density and composition (Paige et al. 2009; Vasavada et al. 1999; Bandfield et al. 2011; Glotch et al. 2011; Thomas et al. 2012; Greenhagen et al. 2010). Three-dimensional thermal physical models of the lunar surface, such as the model developed by Vasavada et al. (1999), represent craters as a grid of surface elements (Figure 14). The one dimensional thermal diffusion equation is then solved for each element with the assumption that each element re-radiates isotropically. If the modelled surface is flat then the re-radiation has no effect, however, if the surface is curved, like a cratered surface, then the re-radiation causes other elements of the surface to warm up. The re-radiation effect is of particular importance at higher latitudes on the surface, where the local topography is the main driver in the observed surface temperatures in the polar thermal regime.

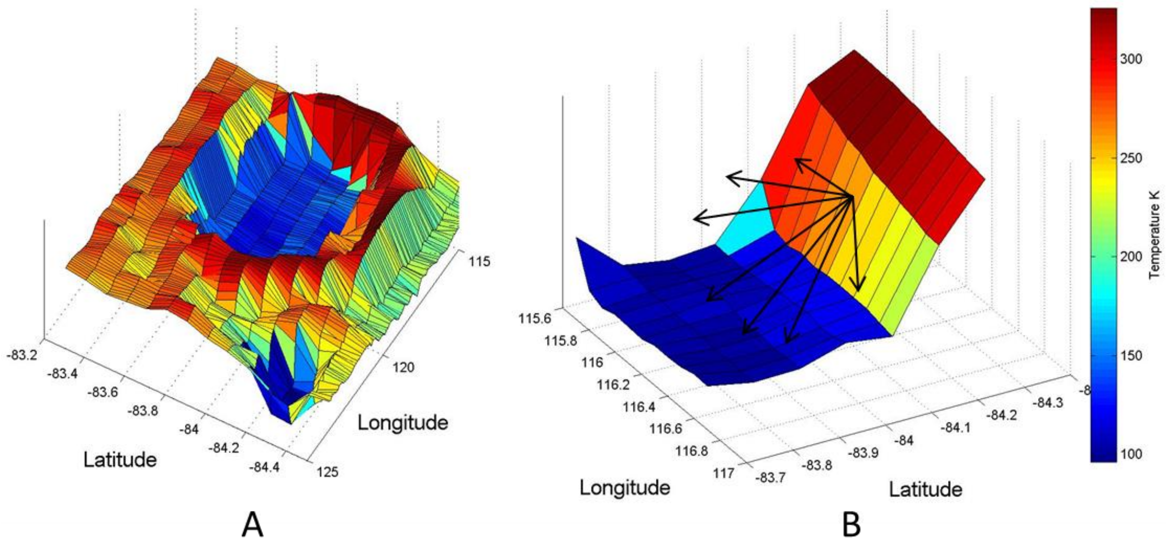

Figure 14: (A) Grid technique used in three dimensional thermal physical models for a crater on the lunar surface of the Moon. (B) Each element is assumed to scatter and re-emit in an isotropic fashion. Note this image was made by downloading Diviner average surface temperature data of Shackleton crater from the PDS archive. The data was then gridded in MATLAB to demonstrate the gridding technique used in 3D thermal physical models.

1.3.1 Complexities of Thermal Modelling the Lunar Surface

Modelling the bolometric temperatures observed by Diviner is complicated by the extreme thermal gradients across the surface of the Moon. As previously explained in section 1.1.2, the night side of the Moon is very cold (<100 K) and the dayside extremely hot (~400 K). On the small scale (<1 m) any shaded region on the dayside surface will be very cold compared to regions in direct sunlight. The surface of the Moon is not smooth, but full of topographic features at all scales (e.g. from impact basins and craters to rocks and pebbles) (Figure 15). Computer stereo-photogrammetry of images from the Apollo Lunar Surface Closeup Camera has been used to show that the lunar surface is rough at all scales from 85 μ – 85 mm (Helfenstein & Shepard 1999).

These topographic features lead to cold, shaded regions at all scales on the lunar surface. The projected field of view (FOV) of the Diviner instrument on the lunar surface during the 'mapping' orbit was ~320 by 160 m and varied between 150 – 1300 m during the extended mission. Given the size of the radiometer's footprint, it is clear that Diviner's FOV contains regions of different temperatures (Figure 16). Therefore the bolometric temperature measured by Diviner is a weighted average of the all the different temperatures in the FOV. The non-uniformity of the Moon's surface temperature inside Diviner's footprint complicates thermal modelling of the lunar surface. The thermal gradient over the depth of the lunar soil (section 1.1.2) also has an effect on the bolometric temperature measured by Diviner, as different channels sound to different depths depending of the spectral range of each channel and the lunar surface properties (Thomas et al. 2012).

Figure 15: Image taken by Apollo 17 of the Taurus Littrow landing site showing the lunar surface to be full of topographic features at a range of scales, all casting shadows on the surface. The temperature difference between areas in direct illumination and areas in shadow can be as much as 100 K (Paige et al. 2010)**.** Taken from (NASA 1972).

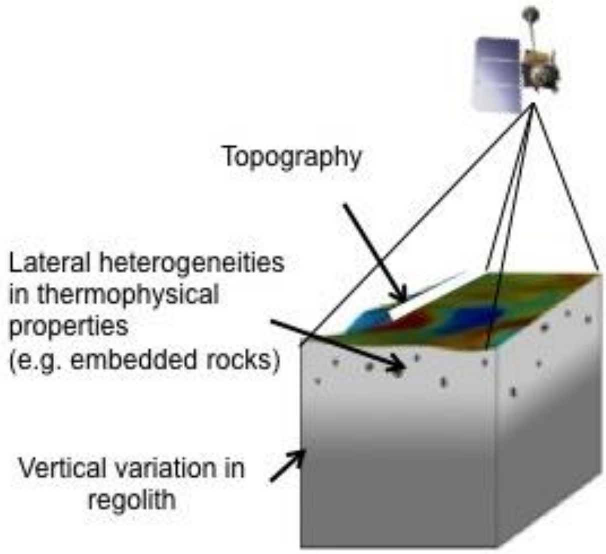

Figure 16: Diagram showing that Diviner's footprint contains a mixture of brightness temperatures. Taken from (Williams 2011)**.**

1.3.2 Thermal Modelling of the Lunar Surface – Comparison between Models and the Measured Diviner Data

A state of the art three-dimensional thermal physical model that accounts for re-radiation effects from the lunar surface is compared to the Diviner surface temperature observations in Paige et al. (2010) and the results are displayed in Figure 17, Figure 18 and Figure 19. In general the model is in excellent agreement with the observed data. The only two noticeable discrepancies are:

1. For daytime temperatures in PSRs that have measured temperatures in the range of 60 – 120 K (Figure 19), the model underestimates temperatures by approximately 15 K. Paige et al. (2010) suggests that one possible reason for this discrepancy is that the current model assumes that radiation emitted from the lunar surface is isotropic, however infrared emission from rough sunlight crater walls is thought to be directionally anisotropic.
2. For night-time temperatures where the model overestimates the amount of area on the lunar surface with temperatures between 60 and 80 K and underestimates the lunar surface area with temperatures greater than 80 K and less than 60 K (Figure 18). These discrepancies in the surface area could also be due to directionally anisotropic emission from the lunar surface.

Both discrepancies could also be explained by a temperature dependent emissivity. Later on in section 6.1.5 it is shown that the emissivity of surfaces can drop significantly (0.3) when they are cooled to below 100 K. However, Paige et al. (2010) states that most likely reason for the discrepancies is due to the unrealistic scattering properties used in the model. Accurate three dimensional thermal physical models of the lunar environment require a realistic treatment of scattered solar and re-emitted infrared radiation. This could be achieved by using the Hapke model (described in section 1.5.1) to simulate how radiation is reflected, emitted and re-radiated from the lunar surface.

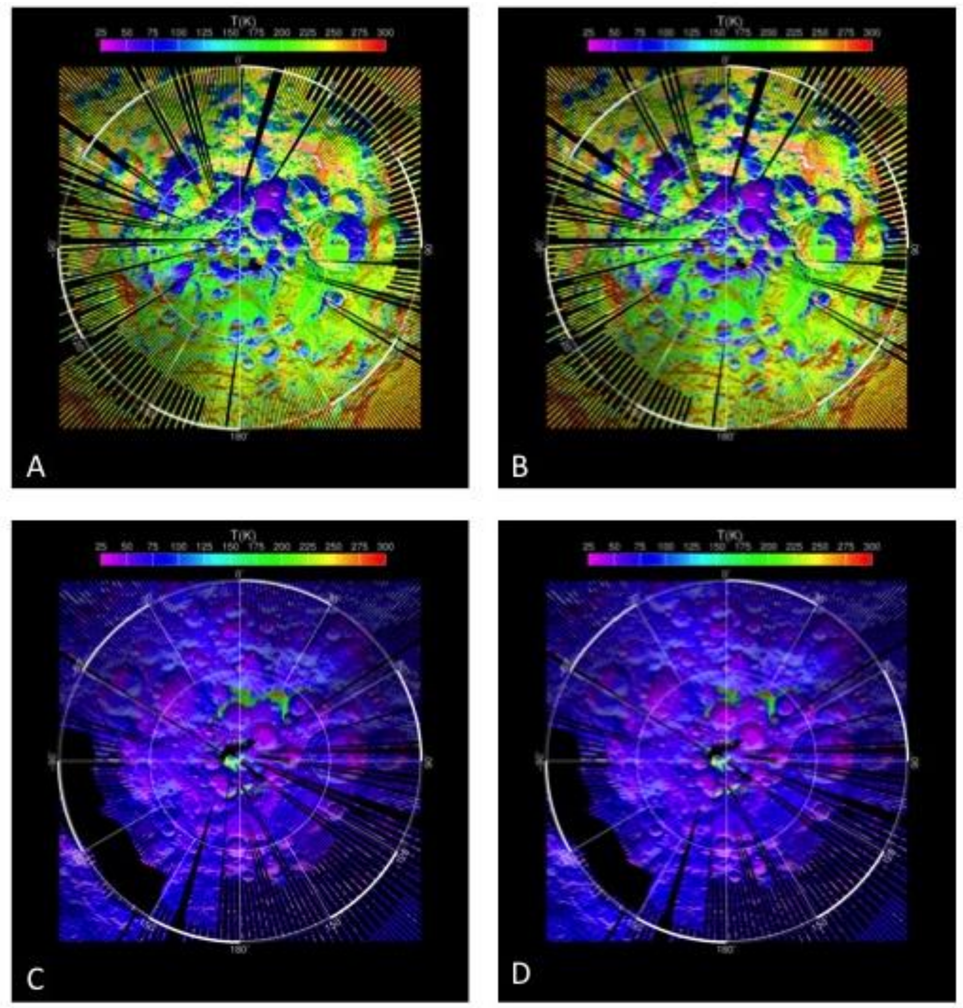

Figure 17: Maps of measured and model-calculated surface temperatures in the lunar South Polar Region, where the outer circle is 80° south latitude. Observations were acquired between 6 September and 3 October 2009 as the Moon approached southern summer solstice. (A) Diviner-measured daytime bolometric brightness temperatures acquired between 11.4 and 13.6 hours local time. (B) Model-calculated daytime surface temperatures at the same locations and times as the Diviner data in (A). (C) Diviner-measured night-time bolometric brightness temperatures acquired between 21.41 and 1.66 hours local time. (D) Model-calculated night-time surface temperatures at the same locations and times as the Diviner data in (C). Taken from (Paige et al. 2010).

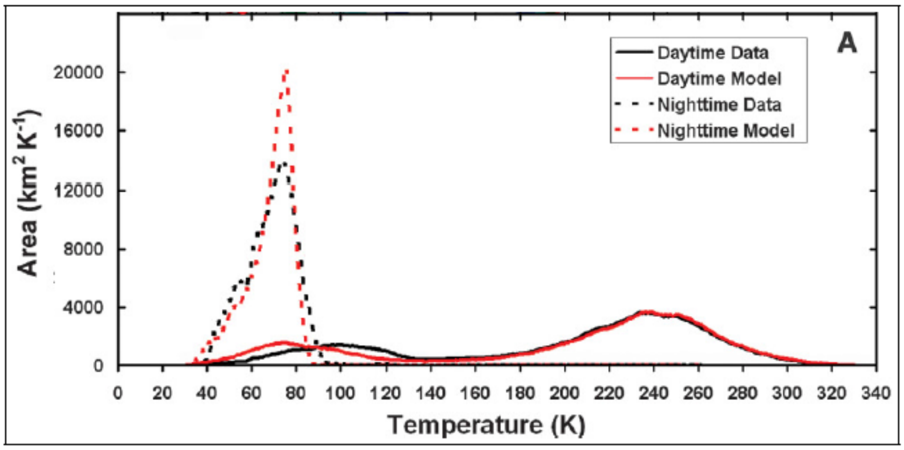

Figure 18: Normalised histograms of measured daytime and night-time bolometric brightness temperatures for the lunar South Pole (as seen in Figure 17). Model-calculated surface temperatures (red) at the same locations and times as those of the Diviner observations (black). A discrepancy can be seen in the daytime for surface temperatures of 1140 – 60 K, where the model under predicts the temperatures. A second discrepancy can be seen in the night-time for surface temperatures at 70 K where the model over estimates the amount of area at 70 K and underestimates the area between 40 – 60 K and 80 – 90 K. Taken from Paige et al. (2010).

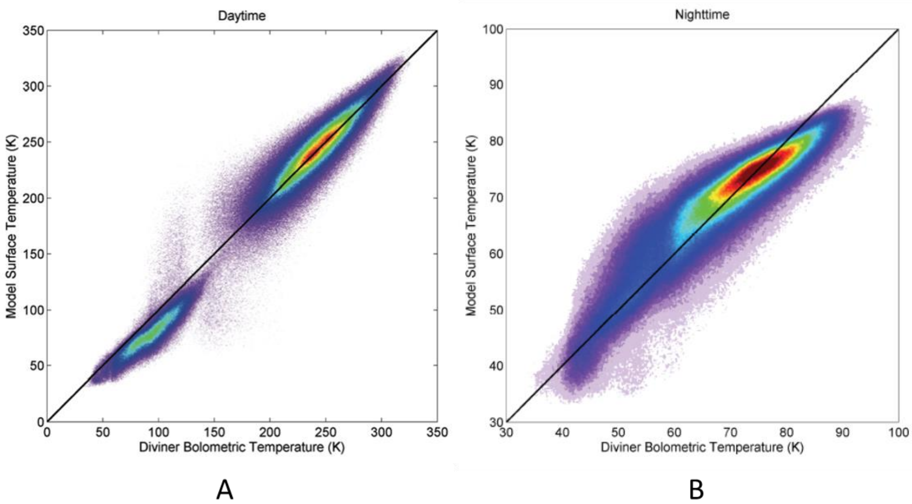

Figure 19: (A) Scatter plot of model calculated daytime surface temperatures against measured Diviner bolometric temperatures from the results shown in Figure 17A and Figure 17B. (B) Scatter plot of model calculated night-time surface temperatures against measured Diviner bolometric temperatures from the results shown in Figure 17C and Figure 17D. Taken from Paige et al. (2010)

1.4 Light Scattering Definitions

As described in the previous section, accurate light scattering models from the visible to the thermal and far infrared are required to accurately model the surface temperatures of airless bodies like the Moon and asteroids. Before describing three commonly used light scattering models (Hapke BRDF, Hapke DE and Fresnel), this section defines the vocabulary used to describe how radiation is scattered from a surface at different wavelengths and observational angles.

1.4.1 Bidirectional Reflectance Distribution Function

The bidirectional reflectance distribution function (BRDF) describes how visible and near infrared light is scattered from a surface for all viewing angles (phase, reflection and incidence, see Figure 20). It is defined (equation 2) as the ratio of the scattered radiance at the detector to the collimated incident irradiance illuminating the surface (Hapke 2014). For airless bodies, the most commonly used BRDF model is the Hapke model described in detail in section 1.5.1 .

$$r(\theta_r, \theta_{i,}\theta_p) = \frac{E_r(\theta_r, \theta_p)}{L_i(\theta_{i,}\theta_p)} \quad (2)$$

Where $r(\theta_r, \theta_i, \theta_p)$ is the BRDF, θ_r, θ_i and θ_p are the angles of reflection, incidence and phase defined in Figure 20. L_i is the irradiance incidence on the surface at incidence angle θ_i and E_r is the radiance reflected from the surface at reflection angle θ_r.

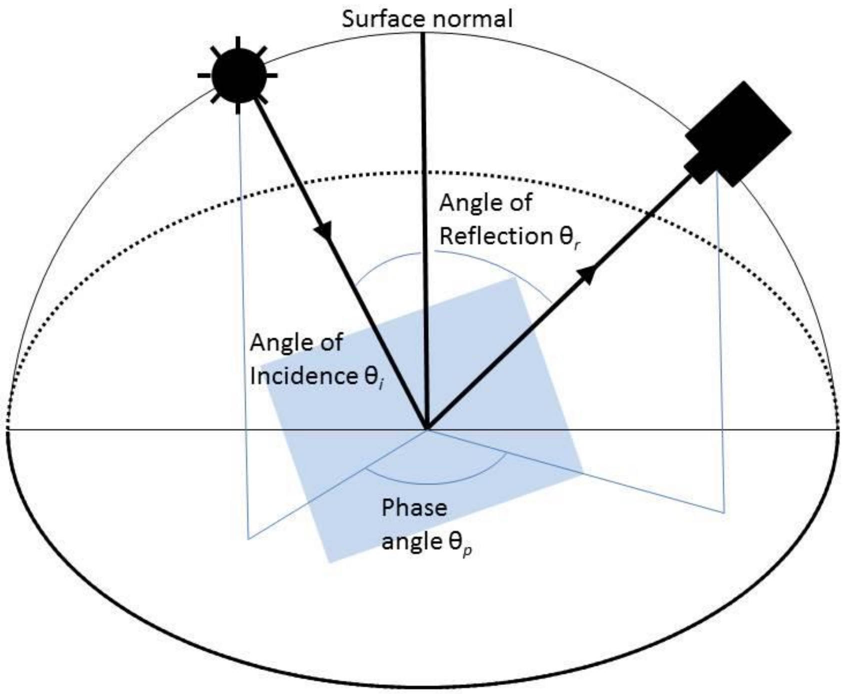

Figure 20: Definition of all scattering angles for the Bidirectional Reflectance Distribution Function (BRDF).

1.4.2 Directional Emissivity

The Directional Emissivity (DE) describes how thermal and far infrared radiation is emitted, reflected and re-radiated from a surface for all viewing angles (phase, emission and incidence, see Figure 21 and Figure 22). This is also referred to as the emission phase function (EPF) (Bandfield et al. 2015). There is no consensus on the terminology used to define the DE and a single uniform term for DE is difficult to define. Therefore for clarity in this thesis the DE is split into three different categories:

1. Pure directional emissivity
2. Re-radiated directional emissivity
3. Reflected and re-radiated emissivity

The pure directional emissivity describes how the emission of a hot surface (>0 K) heated from below varies with emission angle (Figure 21). The pure DE is defined (equation 3) as the ratio of the radiance emitted from the sample to the radiance that would be emitted by an ideal blackbody under the same conditions (e.g. surface temperature, wavelength range and viewing angle). As the sample is heated from below there is no incidence plane as there is no light source and the phase angle must be defined from an arbitrary plane (Figure 21).

$$\varepsilon_d(\theta_e, \theta_p, T, \lambda) = \frac{E(\theta_e, \theta_p, T, \lambda)}{U_b(T, \lambda)} \quad \textbf{3}$$

Where ε_d is the directional emissivity, E is the radiance emitted by the surface, U_b is the total radiance emitted by a blackbody at the same temperature as the surface and θ_e, θ_p are the emission and phase angles defined in Figure 21. T is the temperature of the surface and λ is the wavelength range being viewed.

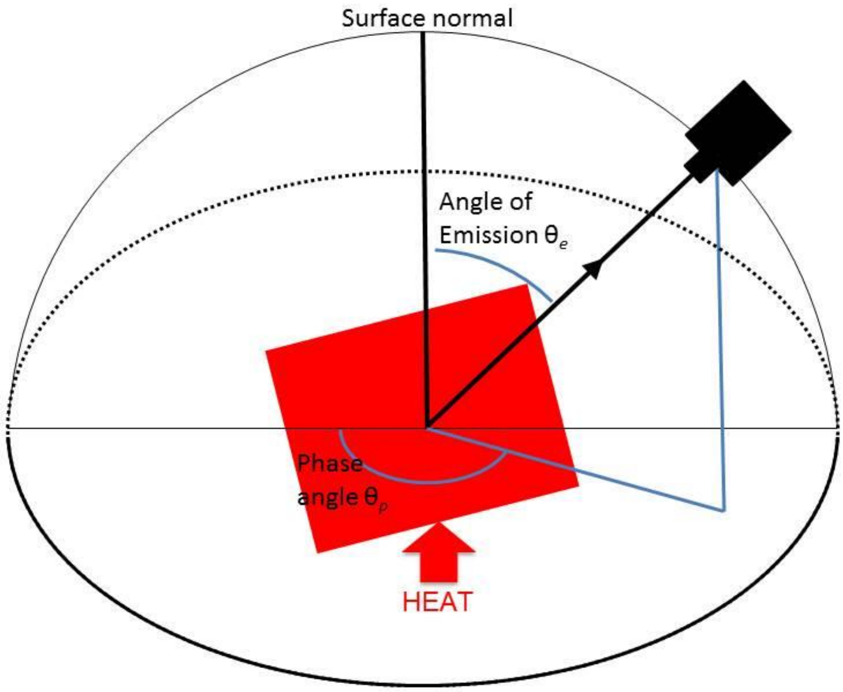

Figure 21: Definition of scattering angles for directional emissivity when the surface is heated from below and is not illuminated. As there is no illumination source the phase angle is defined from an arbitrary plane.

Instead of being heated from below a surface can also be heated from above by a light source. In this case the radiation from the light source is absorbed and then re-radiated (emitted) from the surface. The directional re-radiated emissivity describes how the surface re-radiates the absorbed light. The directional re-radiated emissivity is defined similarly to the pure DE in equation 4 as the ratio of the radiance emitted by the sample to the radiance emitted by a blackbody under the same conditions (e.g. surface temperature, wavelength range and viewing angle). It is important that the wavelength of the light source used does not overlap with the detector wavelength sensitivity. If the wavelength of the light source does overlap with the detector wavelength sensitivity then some reflected radiation would be detected. The definition of directional re-radiated emissivity is strictly limited to how the surface re-emits radiation and does not include any contribution from reflected radiation.

$$\varepsilon_{dr}(\theta_e, \theta_p, \theta_i, T, \lambda) = \frac{E(\theta_e, \theta_p, \theta_i, T, \lambda)}{U_b(T, \lambda)} \qquad \textbf{4}$$

Where ε_{dr} is the directional re-radiated emissivity, E is the radiance emitted by the surface, U_b is the total radiance emitted by a blackbody at the same temperature as the surface and $\theta_e, \theta_p, \theta_i$ are the angles defined in Figure 22. T is the temperature of the surface and λ is the wavelength range being viewed.

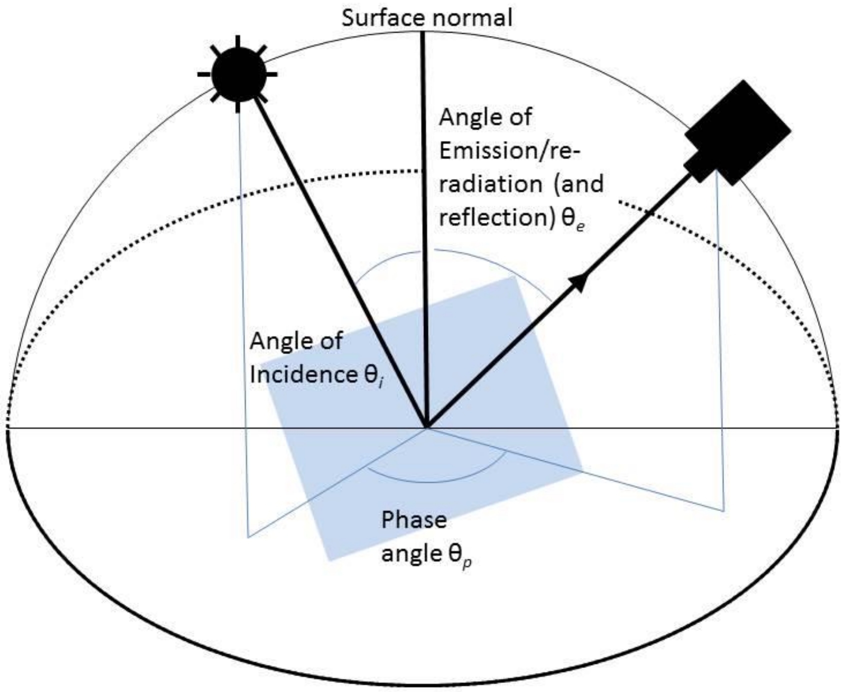

Figure 22: Definition of all scattering angles for the directional re-radiated emissivity when the surface is heated from above by illumination.

When the sample is heated from above by a light source with a wavelength that overlaps with the detectors wavelength sensitivity some of the incident radiation is reflected as well as absorbed and re-emitted from the surface. In this case the directional reflected and re-radiated emissivity describes how thermal radiation is reflected, re-radiated and emitted from the surface. This type of DE is not considered in this thesis.

1.5 Light Scattering Models

Now the different light scattering vocabulary has been defined, this section introduces three commonly used models to predict the scattering behaviour of surfaces. The BRDF of Apollo soil samples have previously been measured and modelled extensively across the visible to near infrared wavelengths (Shepard 2002; Foote & Paige 2009; Pommerol et al. 2011). In the planetary science community most BRDFs of surfaces are modelled using the Hapke BRDF model, described in this section. The Hapke BRDF model is only valid in the visible and near infrared and therefore is not strictly applicable to the thermal and far infrared DE (further details in section 1.5.2), however many of the concepts in the model may apply in the thermal infrared.

Hapke has also developed a simplistic model for the DE in the thermal infrared that models the emission of a particulate medium as a function of emission angle (Hapke 2014). However as Hapke states, there have been very few laboratory measurements of the DE of either Apollo lunar soil samples or lunar analogue materials thus Hapke's DE model has not been verified against the necessary lab measurements. Most DE measurements made thus far in the laboratory have been of metals and glass for the application of solar panels (Silva & Jones 1987; Koirala 2004; Lohrengel 1987). These previous studies have used the Fresnel equations to model their measured DE of surfaces. This section therefore describes three light scattering models:

1. Hapke’s BRDF model
2. Hapke’s DE model
3. Fresnel Equations

1.5.1 Hapke BRDF Model

The Hapke BRFDF model was developed for photometric calculations across visible to near infrared wavelengths and has a fundamental assumption that the particle size of the medium is greater than the wavelength of the incoming and scattered radiation (Hapke 2014). Therefore for typical grain sizes (>10 μm), the Hapke BRDF model is only strictly valid in the visible and near infrared. The radiative transfer equation mathematically describes how electromagnetic radiation is transferred. The Hapke (2014) model is based on the fundamental physics of the radiative transfer equation and modified by the addition of:

- Models of the opposition surge, (section 1.5.1.2).
- Empirical phase functions, (section 1.5.1.4).
- Semi-empirical surface roughness corrections, (section 1.5.1.5).
- Models of single scattering albedo (dependent on estimates of effective particle size, internal transmission factor and path length).

- Estimates of porosity factor.

The Hapke equation has been developed over time and has become increasingly more complex with the current model employing ten parameters (Hapke 2014). A relatively simple version (equation 5) of the Hapke analytical approximation derived by Hapke (1993) employs seven parameters (Table 2). In addition to the seven parameters described in Table 2, the latest Hapke (2014) model includes a porosity correction factor (K) and uses four parameters to describe the opposition surge instead of two. The latest model splits the opposition surge B_0 and h parameter (the amplitude and half width of the opposition surge respectively) into $B_{0,CB}$, h_{CB} and $B_{0,SH,}$ $h_{SH,}$ which describe the contribution to the opposition surge (see section 1.5.1.2) from the shadow hiding (SHOE) and coherent backscattering mechanisms (CBOE) respectively (see section 1.5.1.2 for details on the SHOE and CBOE mechanisms).

$$r(\theta_i, \theta_{r,}\theta_p) = \frac{\omega}{4\pi}\frac{\mu_0}{\mu_0 + \mu}\left[1 + B(\theta_p)\right]\left[p(\theta_p) + H(\mu_0)H(\mu) - 1\right]S(\theta_i, \theta_{r,}\theta_p, \bar{\theta}) \quad \mathbf{5}$$

Where $r(\theta_i, \theta_{r,}\theta_p)$ is the bidirectional reflectance distribution function (BRDF), θ_i, $\theta_{r,}$ and θ_p are all angles defined in Figure 20, $\mu_0 = \cos(\theta_i)$ and $\mu = \cos(\theta_r)$, w is the single scattering albedo, $B(\theta_p)$ is the opposition effect defined in equation 7, $H(x)$ is the H function, approximated by equation 6, $p(\theta_p)$ is the particle phase function parameter and $S(\theta_i, \theta_{r,}\theta_p, \bar{\theta})$ is the shadowing function

(Hapke 1993). A brief description of the main Hapke parameters in equation 5 are given in the following sections (1.5.1.1 – 1.5.1.5).

Table 2: Summary of model parameters in Hapke (1993).

Model Parameter	Description
$\boldsymbol{\omega}$	Average Particle Single Scattering Albedo: a measure of the efficiency of a typical regolith grain to scatter and absorb light.
$\boldsymbol{g_1, g_2, f(\theta_p)}$	Parameters of the three-term Henyey-Greenstein particle phase function. g_1 and g_2 respectively describe the narrowness of the backscatter and forward scattering lobe and f is a partition coefficient that describes the relative contributions of each. It measures the directional scattering dependence of regolith grains.
$\boldsymbol{B_0(\theta_p), h}$	Amplitude and angular half width (radians), respectively of the opposition effect
$\boldsymbol{\bar{\theta}}$	Arbitrary parameter describing the average slope angle of the surface

1.5.1.1 H function

In Hapke (1993) the H function is defined as:

$$H(x) = \frac{1 + 2x}{1 + 2\gamma x} \qquad \textbf{6}$$

Where γ is the albedo factor, defined as $\gamma = \sqrt{1 - \omega}$ and ω is the single scattering albedo.

1.5.1.2 Opposition Surge Function

The opposition surge $B(g)$, often referred to as the opposition effect, is the rapid, nonlinear increase in brightness with decreasing phase angle observed near $\theta_p = 0$. This is often observed as the brightening of a rough surface when illuminated from directly behind the observer and can be seen as a bright halo around the shadow of the astronauts' head in the Apollo photograph in Figure 23. This effect is also observed in the Hapke modelled BRDF of an Apollo sample (Figure 24) measured by the Bloomsburg University Goniometer (BUG, described in section 1.5.5).

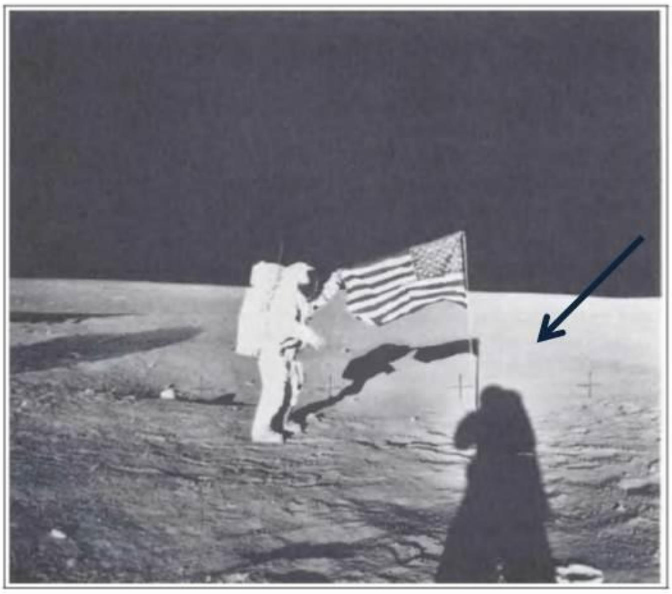

Figure 23: Photograph taken by an Apollo 11 astronaut of his own shadow on the lunar surface next to the flagpole. The bright glow around the shadow of his head is the opposition effect. After Hapke (2014).

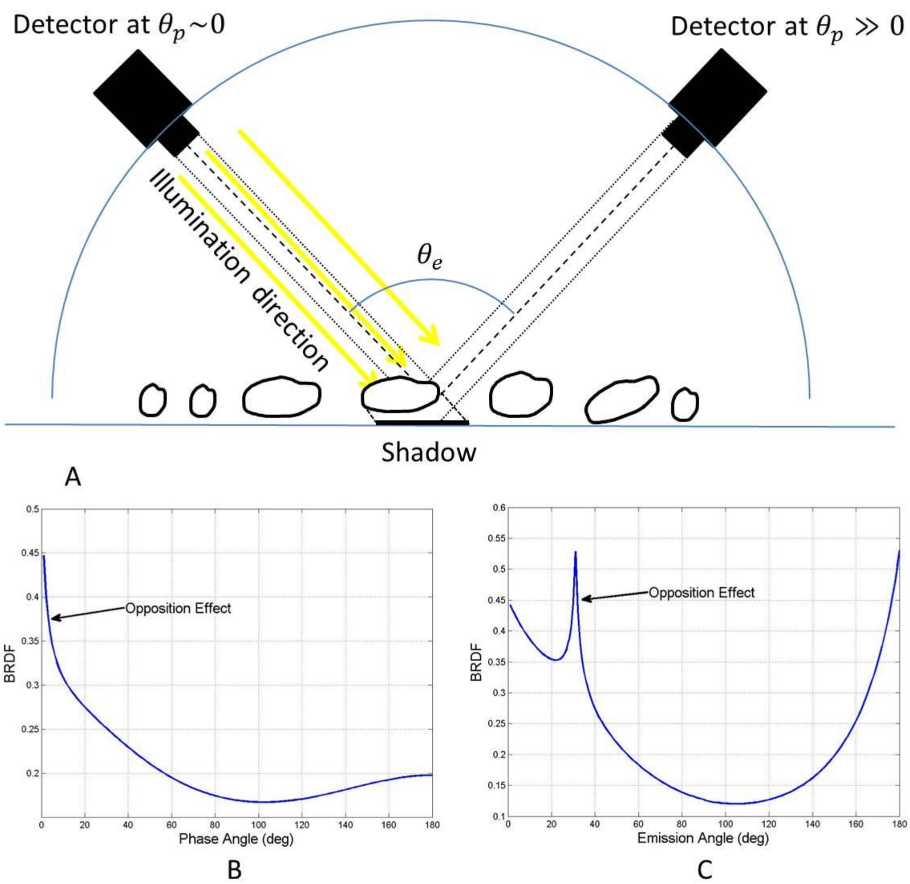

Figure 24: Schematic of the opposition effect. (A) Diagram showing how the SHOE mechanism works. At near zero phase angles, when the detector is aligned with the illumination direction shadows cast by the particles are hidden from view. At all other phase angles the shadows can be seen by the detector. This causes a large spike in reflection at phase angles near zero degrees. (B) Hapke modelled BRDF data of an Apollo soil (10084) sample measured by the BUG goniometer where the opposition can be seen as the large increase in BRDF at low phase angles (Johnson & Shepard 2009). (C) The same Hapke modelled data, but plotted against emission angle in the principle plane, the opposition surge can be seen at 30^{o}, corresponding to directly behind the illumination source.

The cause of the opposition effect has been a subject of great debate. Originally it was believed that this effect was caused by shadow hiding where, in a medium with particles that are large compared with the wavelength, particles near the surface cast shadows on the deeper grains (Hapke 1993). These shadows are visible at large phase (>10^o) angles, but at close to zero (<10^o) phase angles they are hidden by the particles that cast them (Figure 24). However, it was later shown that coherent backscattering could also explain the opposition surge (Hapke et al. 1998). In the coherent backscattering phenomenon, portions of waves travelling in opposite directions along multiple scattered paths within a non-uniform medium interfere constructively with each other to cause a peak at a phase angle of zero. Current theory suggests that the opposition surge is a combination of shadow hiding (SHOE) and coherent backscattering mechanisms (CBOE). CBOE is believed to dominate at small phase angles (<5^o) and SHOE at larger phase angles (>5^o) (Helfenstein & Shepard 2011). In Hapke (1993) the opposition effect is modelled by equation 7.

$$\bar{B}(\theta_p) = \frac{B_0}{1 + \frac{1}{h}\tan(\frac{\theta_p}{2})} \qquad \mathbf{7}$$

Where h is the width of the opposition surge and B_0 is the strength of the opposition surge.

1.5.1.3 Single-Scattering Albedo

The average particle single scattering albedo, w, is defined in equation 8 as the ratio of the amount of light at a given wavelength scattered from a representative incremental volume of a medium to the combined amount of light scattered from and absorbed by it (Hapke 1993).

$$\omega = \frac{\sigma_{sca}}{\sigma_{sca} + \sigma_{abs}} \quad \mathbf{8}$$

Where σ_{sca} is the scattering coefficient, the fraction of light scattered from the medium and σ_{abs} is the absorption coefficient, the fraction of light absorbed by the medium. The allowed values for the single-scattering albedo for a particular medium is then $0 \leq \omega \leq 1$.

1.5.1.4 Single-Particle Phase Function

The single particle phase function, $p(\theta_p)$, is normally modelled as either a Legendre polynomial series or a Henyey-Greenstein (HG) function of one, two or three terms. HG is usually preferred over a Legendre polynomial series as it can describe complex scattering with the same accuracy and fewer parameters (Shepard & Helfenstein 2007). The three term HG (3T-HG) function is defined in equation 9.

$$p(\theta_p) = \frac{1-f}{2} \frac{1-g_1^2}{\left(1+2g_1\cos(\theta_p)+g_1^2\right)^{1.5}} + \frac{1+f}{2} \frac{1-g_2^2}{(1-2g_2\cos(\theta_p)+g_2^2)^{1.5}} \quad \mathbf{9}$$

Where the width of the forward and backscattering lobe of a particle is constrained by g_2 and g_1 respectively and f is the partition coefficient between the relative magnitudes. A value between $0.5 < f < 1$ indicates a particle is more forward scattering, while a value between $0 < f < 0.5$ indicates more backscattering (Figure 25).

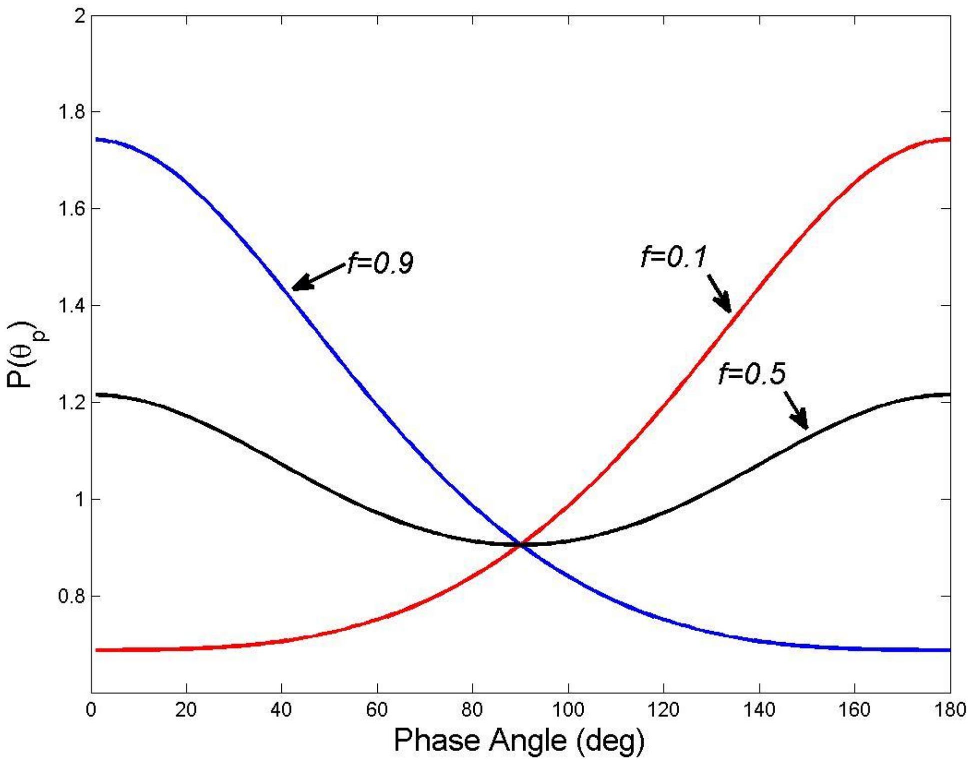

Figure 25: Henyey-Greenstien particle phase function for several values of the partition coefficient, f, with g_1 and g_2 constant at 0.2. For a partition coefficient of 0.5 (black) the backward and forward scattering lobes are equal. For a value of 0.9 (blue) there is more forward scattering and for 0.1 (red) there is more backward scattering.

1.5.1.5 Surface Roughness

Hapke's roughness correction factor is a correction for the macroscopic roughness, considered to include scales ranging from the micro-scale surface roughness to the integral surface roughness at sensor sub-pixel scales (Shepard & Helfenstein 2007; Helfenstein & Shepard 1999; Hapke 1993). It is difficult to interpret the surface roughness parameter, $\bar{\theta}$ in a geologically meaningful way as there is no well-defined relationship between $\bar{\theta}$ and the length of scale of geological features it represents.

1.5.2 Hapke DE model

Hapke has also developed a model for the angular dependence of the radiance emitted by a surface of an optically thick particulate medium at uniform temperature T (equation 10) (Hapke 2014).

$$\varepsilon_d(\theta_e) \cong \gamma \frac{1+2\mu}{1+2\gamma\mu} \qquad \textbf{10}$$

Where $\varepsilon_d(\theta_e)$ is the DE, γ is the albedo factor, defined as $\gamma = \sqrt{1-\omega}$, ω is the single scattering albedo, $\mu = \cos(\theta_e)$ and θ_e is the emission angle.

The Hapke modelled DE is plotted for several values of the single scattering albedo in Figure 26. Hapke's model predicts that for materials with a small single scattering albedo the DE is approximately unity for all emission angles hence the surface emits like a blackbody (Hapke 2014). Therefore Hapke's emission model states that for high emissivity materials the emissivity can be approximated independently of the emission angle. However, Hapke (2014) also states that only a few measurements of the DE have been published and although the Hapke DE model is in “qualitative agreement” with the DE measurements, further measurements are required to test the model. The Hapke DE model is valid for the pure DE and re-radiated DE, however it does not included any terms for the opposition effect found in the Hapke BRDF model.

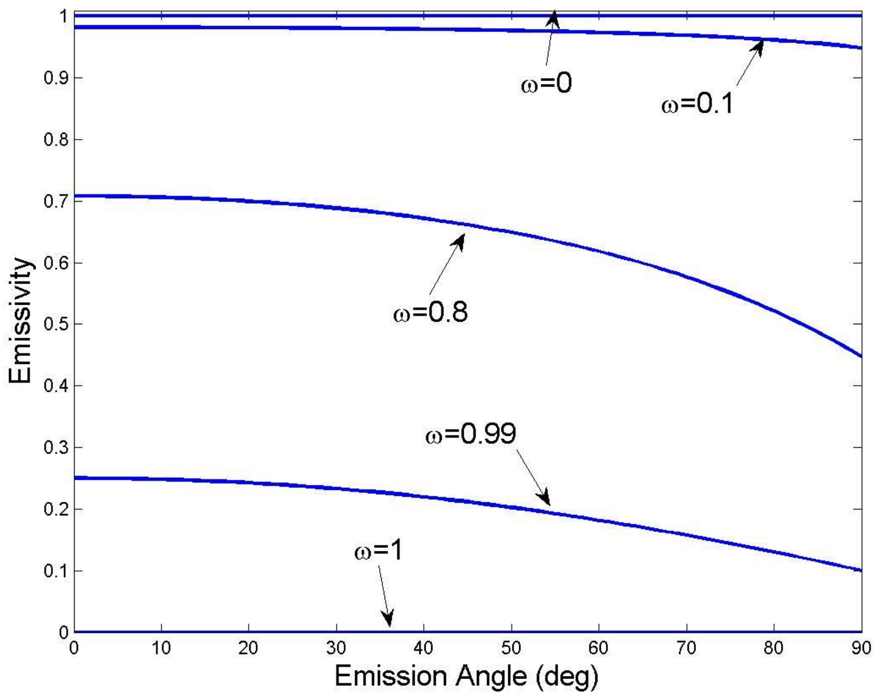

Figure 26: DE of a particulate medium for several values of the single scattering albedo as predicted by Hapke’s DE model.

1.5.3 Thermal Shadow Hiding Opposition Effect

Hapke argues that the shadow hiding and coherent backscatter mechanisms discussed in section 1.5.1.2 need a preferred direction and cannot be applied to the DE model when a sample is heated from below (Figure 21). However, when a sample is heated from above by an illumination source (e.g. sunlight) a type of SHOE can occur where one part of the surface cast a shadow over another. The areas in shadow will then be cooler than the areas in direct illumination. In this case at zero phase angle the detector will not see the cooler regions in shadow, but at all other phase angles the detector will see a mixture of cold shadowed regions and warm illuminated regions. To have a thermal opposition effect two conditions must be met:

1. The portions of the medium that radiate to space must be able to change temperature sufficiently rapidly that they can stay approximately in phase with the illumination, i.e. the medium must have small thermal inertia.
2. The difference in temperature between the cold shadowed regions and the warm illuminated regions must be large enough to make an appreciable difference in emitted thermal radiation.

To maintain a large temperature difference the two regions must be well insulated from one another. Hapke states that the thermal conduction on the Moon prevents an appreciable temperature difference from existing between different parts of one particle or between adjacent particles of the regolith and therefore a thermal opposition effect cannot be produced by shadowing between particles (Hapke 2014). Only large scale surface irregularities on the lunar surface can produce this thermal opposition effect. However, it has been shown that significantly large (>100 K) thermal gradients do exist across hundreds of microns on the lunar surface (Thomas et al. 2012; Millán et al. 2011), so a thermal opposition effect is likely to be produced by shadowing between particles on the lunar surface.

1.5.4 DE derived from the Fresnel Equations

The DE of an optically smooth surface can also be modelled using the Fresnel Equations. The Fresnel equations for reflection and transmission use the optical constants of a medium (n and k) to describe the behaviour of the parallel and perpendicular components of an electromagnetic wave incident on a dielectric or conducting surface. In this section a simple derivation of the Fresnel formula for an opaque dielectric surface is given. The Fresnel formula for any conducting surface is stated and discussed, however the derivation is beyond the scope of this thesis.

1.5.4.1 Optical Constants

The optical constants of a medium (n and k) are known as the real and imaginary parts of the index of refraction and are related to the material's electromagnetic properties by equations 11 and 12.

$$n = c_0 \sqrt{\frac{\mu_m \mu_{m0} \varepsilon_e \varepsilon_{e0}}{2}\left[1 + \sqrt{1 + \left(\frac{\sigma_e}{\omega_f \varepsilon_e \varepsilon_{e0}}\right)^2}\right]} \qquad \textbf{11}$$

$$k = c_0 \sqrt{\frac{\mu_m \mu_{\ 0} \varepsilon_e \varepsilon_{e0}}{2}\left[-1 + \sqrt{1 + \left(\frac{\sigma_e}{\omega_f \varepsilon_e \varepsilon_{e0}}\right)^2}\right]} \qquad \textbf{12}$$

Where μ_{m0}, ε_{m0} and c_0 are the magnetic permeability, electrical permittivity and the speed of light in vacuum respectively. μ_m, ε_e and σ_e are the relative magnetic permeability, relative electric permittivity and electrical conductivity respectively of the medium and ω_f is the angular frequency of the electromagnetic wave. A material's complex index of refraction is defined as $\bar{n} = n + ik$, where n is the real part of the index of refraction and k is the imaginary part. The imaginary part of the index of refraction is known as the extinction coefficient as it characterises the attenuation of electromagnetic waves through a medium. A large extinction coefficient means that the beam is quickly attenuated while passing through the medium and a small extinction coefficient means that the medium is relatively transparent to the electromagnetic radiation. From equation 12, a perfect dielectric ($\sigma_e = 0$) has its imaginary part equal to zero and hence its complex index of reflection only contains a real part, n.

1.5.4.2 Derivation of the Fresnel Formula for an Opaque Dielectric Medium

Consider the case of an electromagnetic plane wave propagating though medium 1 that is then incident upon an interface between an ideal dielectric media 1 and 2 at an angle of incidence (Figure 27). A fraction of this radiation will be reflected and the rest will propagate through medium 2 at an angle of refraction (Figure 27). Snell's law of refraction (equation 13) can be used to express the angle of refraction and incidence in terms of the optical constants of the two medium:

$$\frac{\sin(\theta_t)}{\sin(\theta_i)} = \frac{n_1}{n_2} \tag{13}$$

Where n_1 and n_2 are the real part of the index of refractions for medium 1 and 2 respectively.

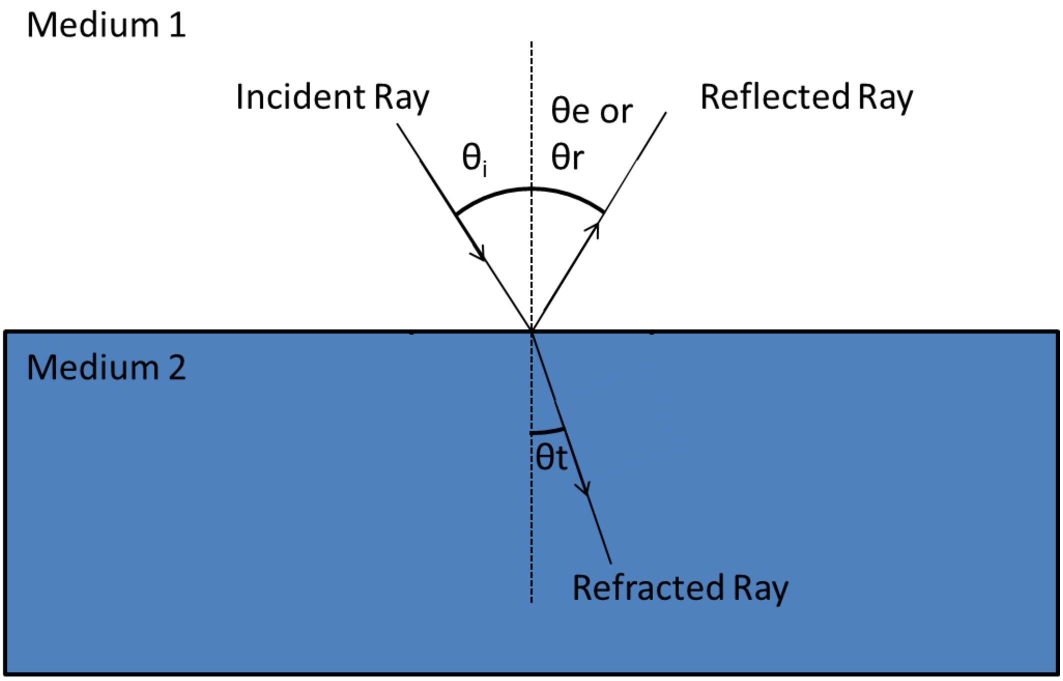

Figure 27: Interaction of an electromagnetic wave with boundary between two media. The angle between the surface normal and the direction of the reflected ray can either be the angle of emission or the angle of reflection, as the reflectivity of a surface at a given angle can be equated to the emission of a surface by Kirchoff's law.

The incident and reflected electromagnetic beam can be resolved into two components of polarization: parallel to the plane of incidence and perpendicular to the plane of incidence. The parallel and the perpendicular components of an electromagnetic beam are denoted by a subscript s and p respectively. Assuming that medium 2 is opaque and hence no transmission occurs and also that the optical constants are not directionally dependant within the medium, the reflected beam can be related to the incidence beam by equation 14 and 15.

$$\frac{E_{s,r}}{E_{s,i}} = \frac{\sin(\theta_i - \theta_t)}{\sin(\theta_i - \theta_t)} \quad \textbf{14}$$

$$\frac{E_{p,r}}{E_{p,i}} = \frac{\tan(\theta_i - \theta_t)}{\tan(\theta_i - \theta_t)} \quad \textbf{15}$$

Where $E_{s,r}$ is the parallel component of the reflected beam, $E_{s,i}$ is the parallel component of the incidence beam, $E_{p,r}$ is the perpendicular component of the reflected beam, $E_{p,i}$ is the perpendicular component of the incidence beam and θ_i, θ_r are the angles of incidence and reflection defined in Figure 27.

Using Snell's law of refraction (equation 13) to eliminate the angle of refraction, θ_t, equation 14 and 15 can be simplified and written in alternative forms as functions of optical constants of both media.

$$r_p(\theta_r) = \frac{n^2\cos(\theta_r) - \sqrt{n^2 - \sin^2(\theta_r)}}{n^2\cos(\theta_r) + \sqrt{n^2 - \sin^2(\theta_r)}} \quad \textbf{16}$$

$$r_s(\theta_r) = \frac{\sqrt{n^2 - \sin^2(\theta_r)} - \cos(\theta_r)}{\cos^2(\theta_r) + \sqrt{n^2 - \sin(\theta_r)^2}} \quad \textbf{17}$$

Where n is the ratio of the refractive index of medium 2 to medium 1. Equation 16 and 17 are known as Fresnel's equations of reflection for an ideal dielectric medium. For unpolarised light, where there is an equal intensity from the parallel and perpendicular components, the reflection for an ideal medium can be calculated by taking the average of equation 16 and 17 to give equation 18.

$$r_t(\theta_r) = \frac{r_p(\theta_r) + r_s(\theta_r)}{2} \tag{18}$$

Where r_p is the reflection of the parallel component, r_s is the reflection of the perpendicular component, θ_r is the angle of reflection (Figure 27) and r_t is the reflected electromagnetic beam for unpolarised radiation. The DE of a perfect dielectric can then be calculated using Kirchoff's law (equation 19).

$$\varepsilon_d(\theta_e) = 1 - r_t(\theta_r) \tag{19}$$

Where ε_d is the DE at emission angle θ_e, r_t is the radiation reflected at angle θ_r given in equation 18, θ_r is the angle of reflection and θ_e is the angle of emission.

According to the Fresnel equations, the DE emissivity of a perfect dielectric is dependent on only one free parameter, the ratio of the two media's refractive indices, n. The DE of the dielectric is isotropic for all values of emission angle when n is unity. For larger values of n the DE is isotropic until approximately 60^o, past which the DE decreases with increasing emission angle. In addition as n increases from unity the normal emissivity (DE at $\theta_e = 0$) decreases (Figure 28).

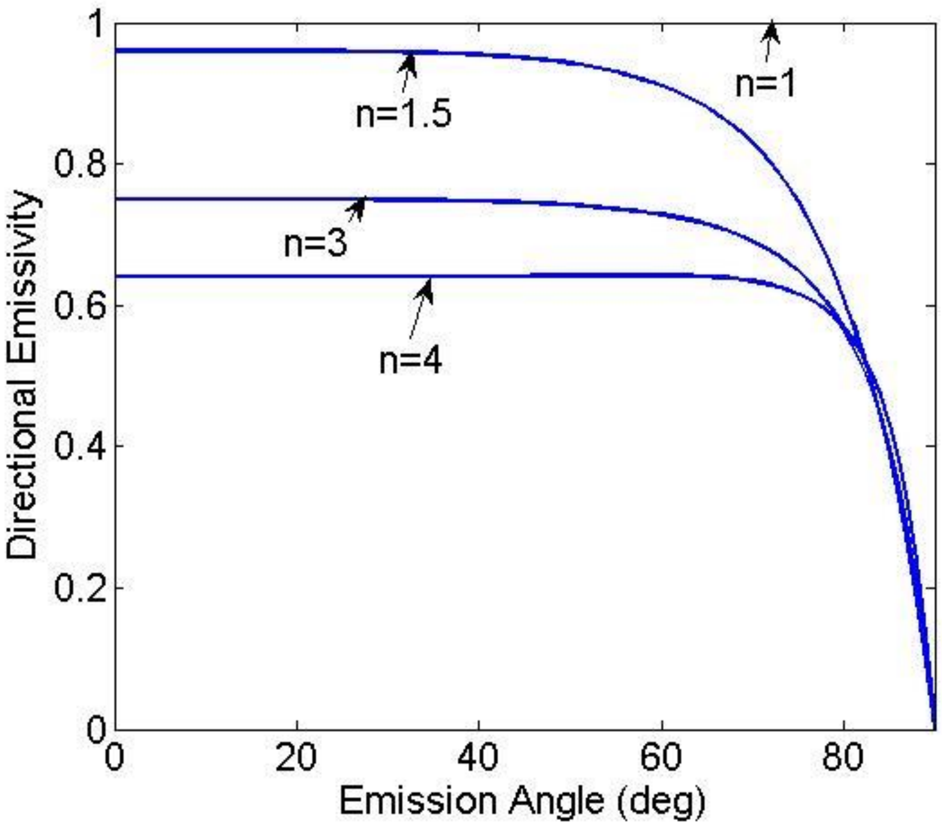

Figure 28: DE curves for a dielectric material with different index of refractions.

1.5.4.3 Fresnel Formula for a Conducting Medium

Equations 16 and 17 can be generalised for the more complicated case of a conducting media, by allowing the extinction coefficient (k) to be non-zero. Assuming that medium 1 (Figure 27) is either air or vacuum simplifies the equations, as the index of refraction is approximately unity for both air and vacuum. The Fresnel formulae for a conducting medium are given in equations 20 and 21.

$$r_s(\theta_r) = \frac{(a - \cos(\theta_r))^2 + b^2}{(a + cos(\theta_r))^2 + b^2} \quad (20)$$

$$r_p(\theta_r) = \frac{(a - \cos(\theta_r))^2 + b^2}{(a + \cos(\theta_r))^2 + b^2} \frac{(a - sin(\theta_r)\tan(\theta_r))^2 + b^2}{(a + sin(\theta_r)tan(\theta_r))^2 + b^2} \quad (21)$$

Where a and b are auxiliary parameters given equations 22 and 23 respectively:

$$a = \sqrt{\frac{1}{2}\left[\sqrt{(n^2 - k^2 - sin^2(\theta_r))^2 + 4n^2k^2} + (n^2 - k^2 - sin^2(\theta_r))\right]} \quad (22)$$

$$b = \sqrt{\frac{1}{2}\left[\sqrt{(n^2 - k^2 - sin^2(\theta_r))^2 + 4n^2k^2} - (n^2 - k^2 - sin^2(\theta_r))\right]} \quad (23)$$

Where n and k are the index of refraction and the extinction coefficient of the investigating medium in air or vacuum. θ_r is the angle of reflection shown in Figure 27.

The DE for a conducting medium can then be calculated as:

$$\varepsilon_d(\theta_e) = \frac{1 - r_t(\theta_r)}{2} = \frac{(1 - r_s) + (1 - r_p)}{2} \quad (24)$$

Examples of the Fresnel calculated DE of two conducting materials with given optical constants is shown in Figure 29. Increasing the extinction coefficient from zero causes the normal emissivity (at $\theta_e = 0^o$) of the material to drop sharply. For dialectic materials with index of refractions greater than unity, the DE is isotropic until 60^o, after which it decreased with increasing emission angle (Figure 28). For mediums with large extinction coefficients the emissivity increases from 60^o until 80^o emission angle, at which point it falls sharply from ~0.3 to zero at 90^o.

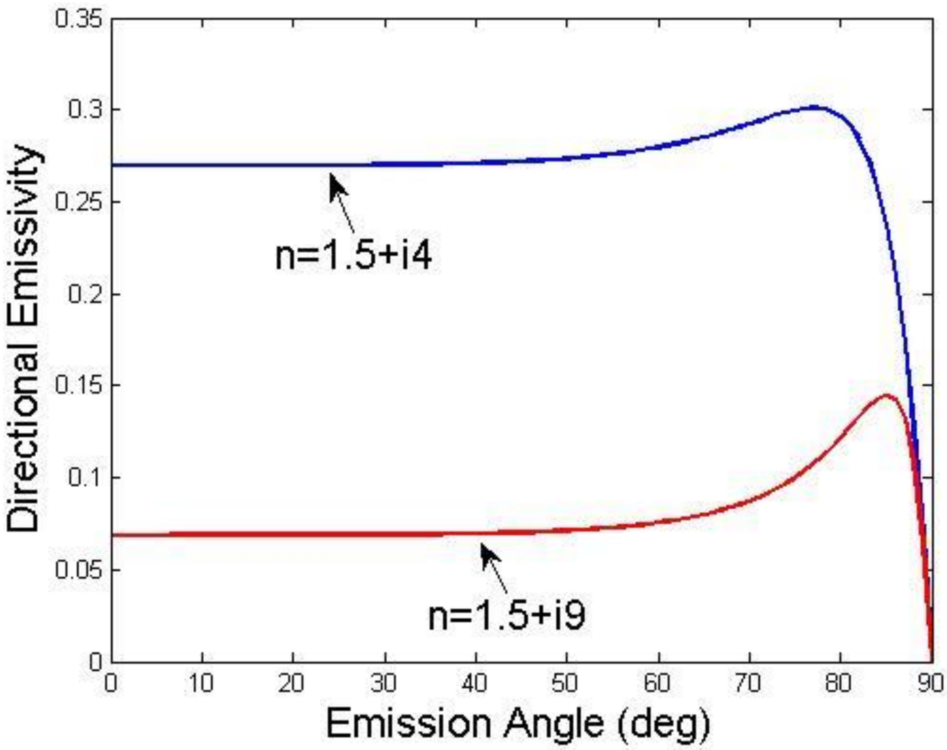

Figure 29: Directional emissivity for a conductor with different indices of refraction.

1.5.4.4 VIS/NIR Goniometry

BRDF measurements of lunar regolith in the visible and near infrared have already been made by a number of different goniometers including the

Bloomsburg University Goniometer (BUG) (Figure 30) and the Physikalisches Institut Radiometer Experiments (PHIRE) (Pommerol et al. 2011; Johnson 2008; Johnson & Shepard 2009; Foote & Paige 2009). Both BUG (section 1.5.5) and PHIRE (section 1.5.6) are able to make automated full BRDF measurements of samples in the visible and near infrared (400 – 1100 nm) (Foote & Paige 2009; Shepard 2002).

1.5.5 Bloomsburg University Goniometer (BUG)

Figure 31 shows the BUG measurements from Shepard (2002) of the full BRDF of Apollo soil sample 10084 at a wavelength of 750 nm and an incidence angle of 60^{o}. The BUG measurements of Apollo 10084 demonstrate that the bidirectional reflectance of lunar soil is very anisotropic at high incidence and emission angles (Shepard 2002). These results have significant relevance for modelling illumination conditions and temperatures in shadowed regions at the lunar poles, as they suggest that the flux of scattered solar photons within shadowed regions may be more than a factor of two higher than has been previously estimated assuming isotropic scattering (Shepard 2002). This could explain some of the deviation between three dimensional thermal physical model results and Diviner measurements in Figure 18, however, DE measurements in the thermal infrared are necessary to better explain the difference.

Figure 30: Image of BUG. The longer arm (two meters long) on the right holds the silicon detector. The shorter arm on the left terminates with a fibre-optic lens assembly that puts a near-collimated beam on the sample. Taken from (Johnson & Shepard 2009).

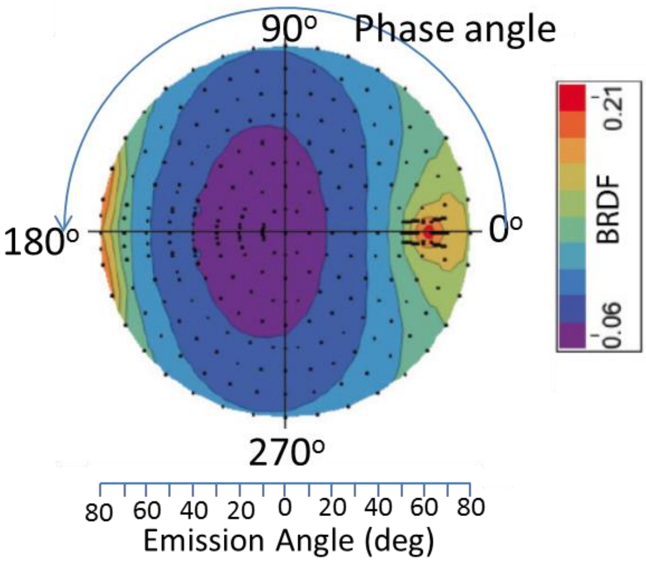

Figure 31: BUG measured bidirectional reflectance function of Apollo soil sample 10084 at 750 nm and at $\theta_i = 60^o$. Taken from Johnson & Shepard (2009)**.**

1.5.6 The PHIRE (Physikalisches Institute Radiometer Experiments)

The PHIRE are two goniometers (PHIRE-1 and PHIRE-2) designed in a similar fashion to BUG. PHIRE-2 (Figure 32) is a modified version of PHIRE-1, to permit measurements at temperatures just below 0^{o}C, to study the photometry of samples containing water ice. The PHIRE-2 goniometer has also taken measurements across visible wavelengths of lunar regolith simulant (JSC-1AF), again showing the anisotropic scattering at high incidence and emission angles.

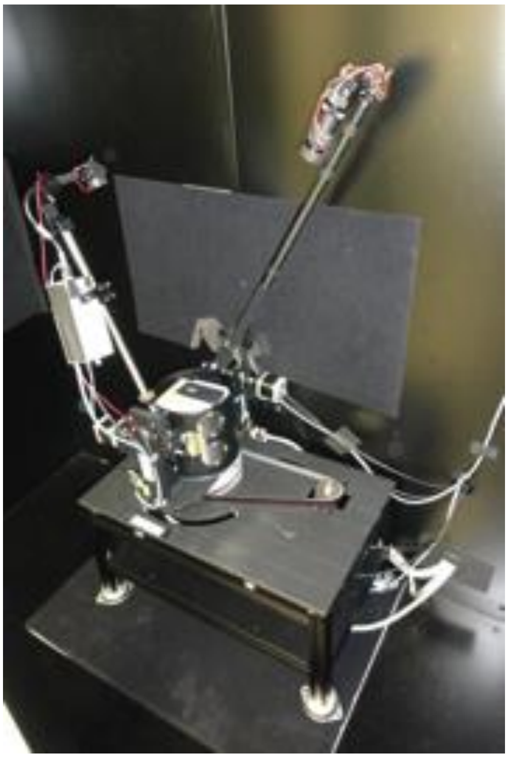

Figure 32: Image of PHIRE-2. The shorter arm on the left holds the silicon detector. The longer arm on the right terminates with a fibre-optic lens assembly that puts a near-collimated beam on the sample. Taken from (Pommerol et al. 2011).

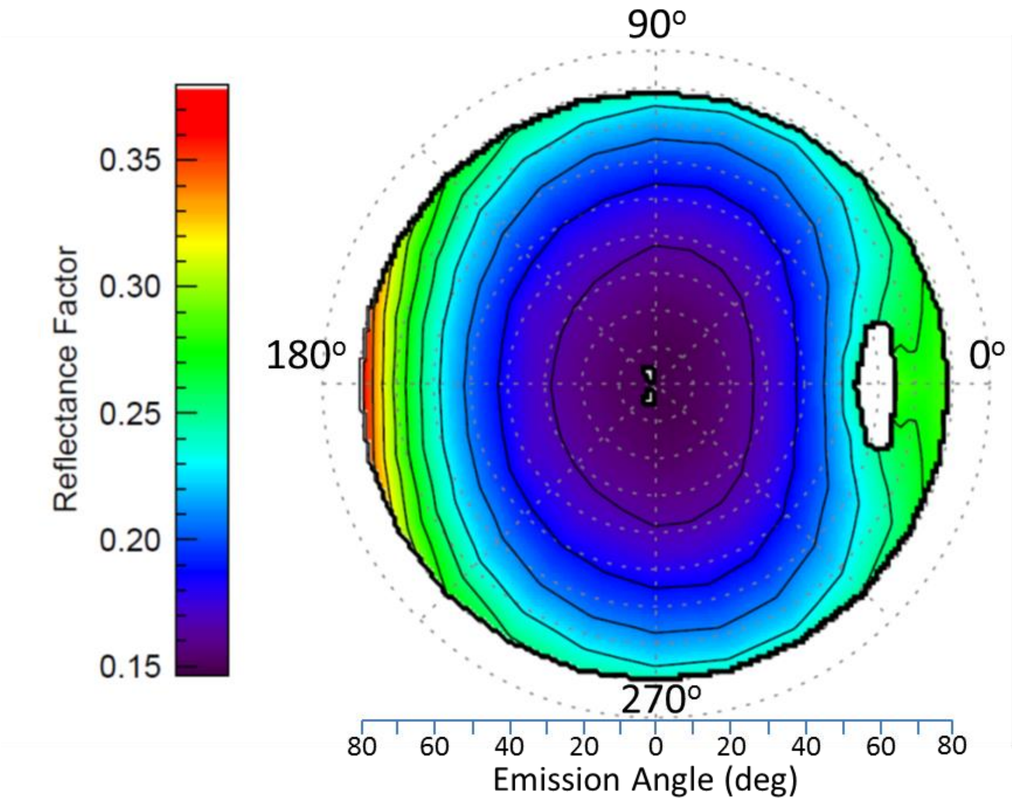

Figure 33: PHIRE-2 measured bidirectional reflectance function of the lunar analogue material JSC1-AF at 750 nm and at $\theta_i = 60^o$. After Pommerol et al. (2011).

1.6 Thermal and Far Infrared Goniometry

Although PHIRE and BUG have made significant progress in measuring the BRDF of the lunar surface across the visible and near infrared wavelengths, no laboratory data is available in the thermal and far infrared spectral range for lunar soils or regolith analogues. The lack of laboratory data in this wavelength range may be due to the following two reasons:

1. Before Diviner there were no available global maps of thermally derived properties from spatially resolved thermal infrared instruments in orbit around airless bodies. Hence, there was no remote sensing data to compare laboratory measurements with.
2. The experimental procedure required to make measurements in the thermal infrared is complex.

Due to design constraints PHIRE and BUG are not able to make goniometric measurements of lunar analogue samples in the thermal infrared. To make realistic thermal and far infrared measurements of Apollo samples the whole experiment (sample and goniometer) must be surrounded by a cold shield and inside a vacuum chamber ($<10^{-6}$ mbar), to simulate the environment of an airless body (see section 3.5 for more details). The BUG and PHIRE setups do not include a cold shield or vacuum chamber and cannot be used to measure the DE in the thermal or far infrared.

At the time of writing three goniometric systems have been found in the literature that are able to make DE measurements of surfaces (De Silva & Jones 1987; Koirala 2004; Lohrengel 1987). All of the systems are designed to investigate the DE of solid surfaces such as glass or metals for the application of solar panels. The three DE goniometers would not be able to measure lunar analogue materials as the systems are not designed to measure powdered samples; the goniometers tilt the sample to change the emission angle, thus the sample would fall out of the sample holder at high emission angles.

1.7 Summary of Introduction

It is clear that a new goniometric system capable of measuring Apollo samples and analogue materials across thermal and far infrared wavelengths is necessary for modelling the lunar surface temperature accurately. The following sections of this thesis detail the design, development and calibration of the Oxford Space Environment Goniometer (OSEG), which is capable of measuring the DE of lunar regolith samples in the thermal and far infrared.

The original motivation for building the OSEG was to support measurements currently being made by the Diviner Lunar Radiometer. The Diviner channels range across the ultraviolet to visible (0.35 μm) to the far infrared (400 μm), with three channels centred on the thermal infrared (8 μm) (Paige et al. 2009). One of Diviner's main goals was to explore permanently shaded craters at the poles of the Moon. It has been shown that permanently shaded craters exist at the lunar poles due to the low axial tilt of the Moon's orbit relative to the Sun. These regions have not been exposed to direct sunlight for billions of years and hence are sufficiently cold to retain water and other volatiles delivered to the surface by comets and meteorites (Vasavada et al. 1999; Arnold 1979; Watson et al. 1961; Siegler et al. 2011; Paige et al. 2010).

Currently, three-dimensional thermal physical models of the lunar surface that attempt to reproduce the brightness temperatures measured by Diviner (Paige et al. 2010; Vasavada et al. 1999), assume that the lunar surface scatters radiation isotropically. While at low latitudes (<80^o) the lunar surface temperature is primarily dependent on the local time of day, at higher latitudes the local topography becomes increasingly important, and at the lunar poles (>80^o latitude) the surface temperature is driven almost entirely by the local topography. Therefore, to model the surface temperature accurately, particularly around the lunar poles it is necessary to accurately know how light and infrared radiation is re-radiated and scattered by the lunar surface (Paige et al. 2010).

Whilst the current models are generally in very good agreement with the bolometric temperatures measured by Diviner, there are two noticeable discrepancies. The largest discrepancy is the daytime temperatures in shadowed regions of craters, where the models underestimate temperatures by roughly 15 K (Paige et al. 2010). Paige et al. (2010) attributes this discrepancy to the failure of the current model to account for directionally anisotropic infrared emission from rough sunlit crater walls. The second discrepancy is the night-time temperatures where the model underestimates and overestimates surface temperatures by approximately ±20 K. This discrepancy could also be attributed to the unrealistic scattering treatment of the model.

Significant progress is being made in determining the scattering properties (BRDF) of the lunar soil in the visible and near infrared (Foote & Paige 2009; Pommerol et al. 2011; Shepard 2002; Hapke 2014), however, there is limited laboratory data available on the DE in the thermal and far infrared. Hapke (2014) developed a model to calculate the BRDF using a number of macroscopic surface parameters, described in section 1.5.1. The scattering properties of lunar analogue samples (JSC-1AF) and Apollo lunar samples have been studied in the visible by measuring the BRDF using the BUG and PHIRE goniometers (Foote & Paige 2009; Pommerol et al. 2011; Shepard 2002) and fitted with parameters from Hapke's models (Figure 31 and Figure 33). Foote & Paige (2009) found the Hapke parameters that fitted the measured BRDF of lunar Apollo sample 10081 were $\omega = 0.33$, $\bar{\theta} = 7$, $h = 0.017$, $B_0 = 1$, $g_1 = g_2 = 0.308$ and $f = 0.425$.

Hapke outlines a simple thermal infrared emission model for particulate surfaces described in section 1.5.2 (Hapke 2014) and a Fresnel model is outlined in section 1.5.4 (Bohren & Huffman 1998). Previous studies in the thermal infrared have investigated the DE of metals, glass and silicon surfaces for the application of solar panels. However, no DE measurements have been made of lunar analogues or Apollo samples.

2 Thesis Outline

In section 3 the Hapke BRDF model described in section 1.5.1 is used as a baseline to derive a set of requirements for a goniometer to make BRDF and DE measurements from the visible to the far infrared. The build and construction of the goniometer from the requirements is described section 4. The goniometer was then validated across the visible and near infrared wavelengths by measuring the BRDF of reference targets with well-known phase functions in section 5.

Once OSEG was validated, broadband (0.2 – 25 μm) DE measurements in the thermal infrared of black (Nextel) painted disks with different surface roughness textures were made and the results are discussed in section 6. In section 7 both the Hapke DE and Fresnel models were used to model the measured DE of the Nextel targets. However, neither model was found to fit the measured data sufficiently accurately (R^2 <0.67). A ray-tracing Monte Carlo technique that accounted for the micron-scale surface roughness of the Nextel target was used in section 7.4, which did produce a good fit (R^2 = 0.995) with the measured DE. In section 8, broadband (0.2 – 25 μm) DE thermal infrared measurements of the powdered lunar simulant (JSC-1AF) were made and modelled with the same techniques used for the Nextel target. The DE measurements of the JSC-1AF sample are compared to large scale (>100 m) broadband DE measurement made by Diviner in section 8.6.

In section 9, the DE measurements of JSC-1AF were fitted with a cosine law to allow easy integration into a three-dimensional thermal physical model of an imaginary crater near the lunar pole. The three-dimensional thermal physical model was run by B. Rozitis (Open University, UK) assuming isotropic scattering and compared to a run assuming anisotropic scattering, to show that a difference in modelled surface temperatures of ~ 10 K. The conclusions and summary of this work is given in section 10 before recommended future experiments and the application of this work to other airless bodies (e.g. asteroids and Mercury) is discussed in section 11.

3 Requirements for a New Thermal and Far Infrared Goniometer

This section outlines the requirements for a goniometer setup to be able to measure both the BRDF in the visible and the DE in the thermal/far infrared of lunar analogue materials or Apollo soil samples. Requirements are set for the:

- Angular range and accuracy
- Signal to noise
- Project field of view (FOV) of the radiometer instrument on the sample
- Temperature stability of the setup
- Frequency stability of the radiometer's chopper
- Sample temperature
- Pressure range

3.1 Signal to Noise and Angular Accuracy Requirements for the Goniometer

The Hapke BRDF model described in section 1.5.1 has been used as a baseline in this section to explore the angular accuracy and signal to noise ratio (SNR) required for a radiometer instrument mounted on a goniometer to resolve the primary features in the BRDF: the opposition surge, empirical phase functions and surface roughness effects. The Hapke BRDF model has been used as the baseline because the Fresnel and Hapke emission models do not have any small angular features (e.g. opposition surge seen at ~75^{o} in Figure 34) and would therefore require a lower angular accuracy.

To resolve the smallest angular feature of the BRDF, the opposition surge (the peak in Figure 34 at approximately 75^{o}), the angular accuracy of the goniometer must be at a minimum half the width of the opposition surge effect. The Hapke parameters used in this section were taken from measured BRDF of Apollo soil sample 10083 (Figure 34) (Shepard 2002). Using this data the angular width of the opposition surge is ~1^{o}, hence the minimum required angular accuracy of the goniometer is set at 0.5^{o}.

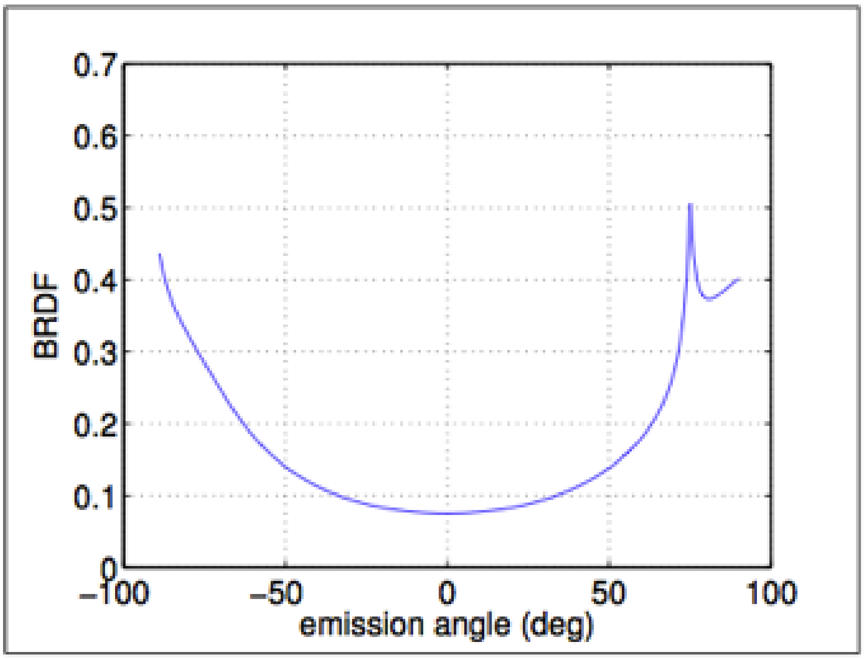

Figure 34: Model calculated BRDF for varying emission angle at 750nm for $\theta_i = 75^o$ in the principal plane (i.e. the light source and detector are in the same plane). The model results shown here employ an optimised set of Hapke parameters that were fitted to a subset of the BUG dataset from (Shepard 2002) that included only data measured in the principal plane. Using the notation of Johnson & Shepard (2009), they are $\boldsymbol{\omega} = \mathbf{0.33}$, $\bar{\boldsymbol{\theta}} = \mathbf{7}$, $\boldsymbol{h} = \mathbf{0.017}$, $\boldsymbol{B_0} = \mathbf{1.0}$, $\boldsymbol{b} = \mathbf{0.308}$, $\boldsymbol{c} = \mathbf{0.425}$.

3.1.1 Radiometric Accuracy Requirements

To explore the SNR requirements of the goniometer, two model calculated BRDFs were compared (Figure 35). A simple model without the effects of surface roughness, opposition surge and empirical phase functions gives a smooth function that was compared with a more complex model to show the level of SNR required to observe the primary features of the BRDF (e.g. the opposition surge, surface roughness effects and the empirical phase function). By adding white Gaussian noise to the complex model until the primary features of the BRDF could not be clearly distinguished (Figure 36), it was found that a minimum SNR of 30 is required for the goniometer to observe the primary features of the BRDF. With a smaller SNR the opposition surge (seen at 70^{o} in Figure 34) is not discernible from the noise. The opposition surge was defined to be undiscernible from the noise when the height of the opposition surge was less than twice the maximum peak to peak ratio of noise.

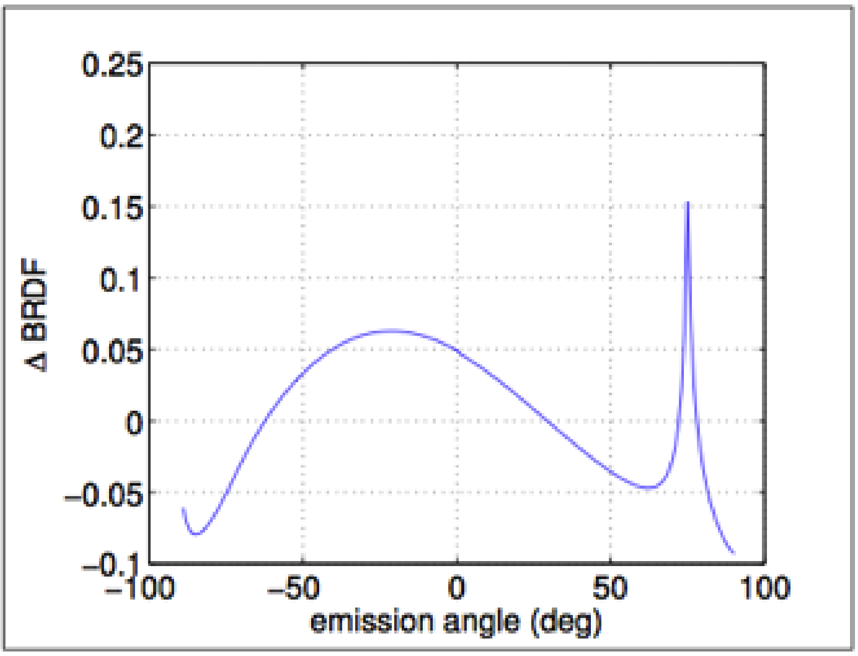

Figure 35: The difference between two model calculated BRDFs at 750nm for $\theta_i = 75^o$, in the principal plane. One model (shown in Figure 34) accounted for the effects of surface roughness, opposition surge, and empirical phase function. The other model assumed lambertian scattering, but did not account for any of the effects in the first model.

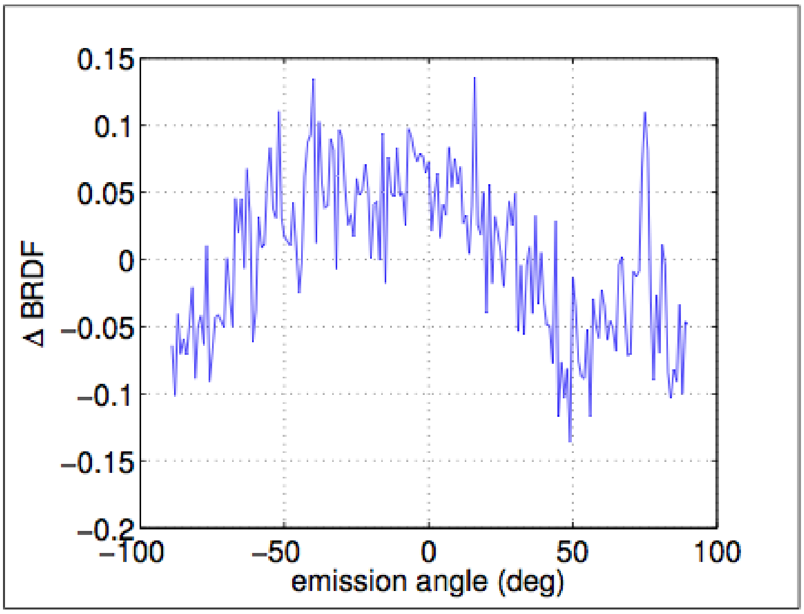

Figure 36: Model calculated BRDF at 750nm for $\theta_i = 75^o$, as shown in Figure 35 but with a SNR of 30.

3.2 FOV Requirements for the Goniometer

It is important the projected FOV of the radiometer instrument is a well-defined uniform circle on the sample being measured at an emission angle of zero degrees. If the FOV is not a well-defined circle the projected FOV will change shape as the emission angle is increased. The measured DE will then be spatially convolved with the shape of the FOV, making the calibration of the DE measurements difficult. With a circular FOV at zero emission angle, as the emission angle is increased the FOV will become ellipsoidal with the semi-major axis increasing inversely proportional to the cosine of the emission angle. It is therefore important that at the maximum emission angle of the goniometer the FOV is not greater than the diameter of the sample. It is also important to ensure that the same section of surface is being sampled such that the FOV does not move across the surface of the sample as the observation angle is changed. As a minimum requirement the FOV must not move off the sample as the emission angle is increased. The size of a sample is 50 mm, the maximum emission angle of BUG and PHIRE is 80^{o}, so the maximum size of the FOV would be 8.5 mm when at an emission angle of 90^{o}.

3.3 Temperature Stability Requirements for the Radiometer, Thermal Background and Sample

The goniometer system will consist of two arms, one carrying the radiometer carriage and another with an illumination source that points at a sample in the centre. The two arms are able to move around the sample to change the emission, incidence and phase angles. For measuring the BRDF that the light source beam will be chopped and the signal recorded by the radiometer will be fed into a lock-in amplifier to record only chopped radiation. For measuring the pure DE the light source will be removed and the sample heated from below by a heating element attached to the underside of the sample cup. As there is no illumination source the chopper will be placed on the radiometer carriage in front of the detector, filter wheel and baffle (Figure 37). The beam should be chopped for three reasons:

1. To remove the background radiation from the signal by subtracting the chopper radiance.
2. To make an alternating output signal level from the detector to reduce the $^{1}/_{f}$ noise.
3. Some detectors (e.g. pyroelectric detectors) only respond to changes in their scene temperature, hence chopping is required to get a signal if viewing a scene of constant temperature.

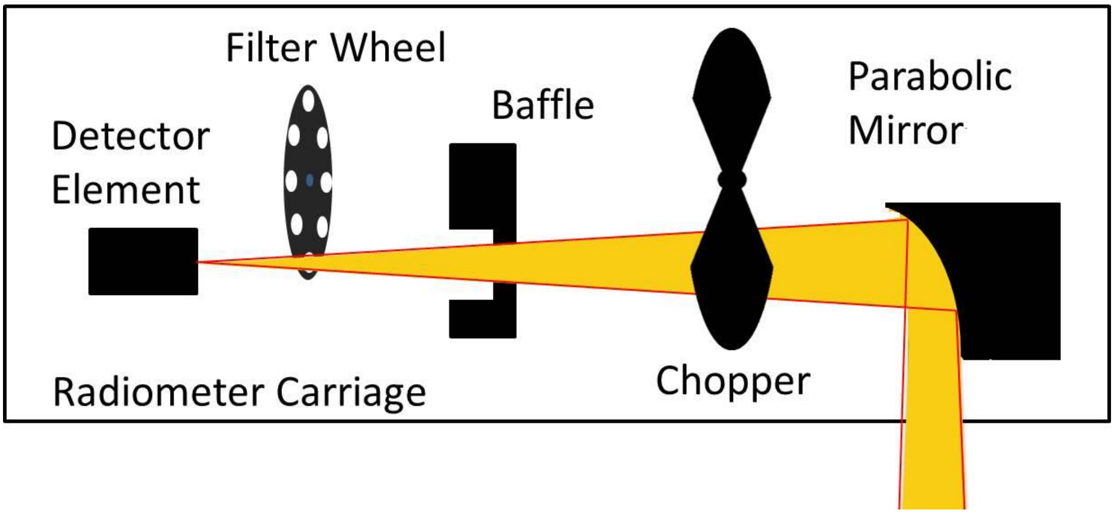

Figure 37: Example layout of a radiometer instrument with detector element, filter wheel, baffle, chopper and parabolic mirror that could be used in a thermal and far infrared goniometer.

Assuming a pyroelectric detector is used to make measurements in the thermal infrared as part of a radiometer (Figure 37), the signal recorded by the lock-in amplifier can be calculated as the difference between the radiance incident on the detector when the chopper blades are open compared to the radiance incident on the detector when the chopper blades are closed (equation 25).

$$V = \bar{R}(E(T)\varepsilon_d(\theta_e, \theta_p, \theta_i, T, \lambda) + e_1(\theta_e, \lambda) + e_2(\lambda) + e_3(\lambda) - e_4(\lambda) - e_5(\lambda)) \quad (25)$$

Where V is the voltage output of the system, $\bar{R}$ is the responsivity of the system (measured in volts per watt per m^2 of chopped radiation) and $\varepsilon_d(\theta_e, \theta_p, \theta_i, T)$ is the DE of the sample that is measured. The first four terms provide the signal when the chopper blades are in the open position and the last two terms provide the signal when the chopper blades are in the closed position. $E(T)\varepsilon(\theta_e, \theta_p, \theta_i, T)$ is the spectrally integrated radiance emitted by the sample that can be seen by the detector. E takes the form:

$$E(T) = \Omega \mathrm{R}_m \int_{\lambda_2}^{\lambda_1} B(\lambda, T) d\lambda \quad (26)$$

Where Ω is the solid angle subtended by the baffle aperture, R_m is the reflectivity of the parabolic mirror, $B(\lambda, T)$ is the Planck function at temperature T and wavelength λ. λ_1 and λ_2 are the cutoff and cut on wavelengths of the filter being used in the radiometer. Each e_x term in equation 25 is an extra contribution that is measured in addition to the signal from the sample. Each e_x term can therefore be considered a source of systematic error:

- e_1 is the thermal background radiance reflected off the sample and seen by the detector at emission angle θ_e and wavelength λ.

- e_2 is the radiance seen by the detector emitted by the radiometer components that are behind the chopper (e.g. baffle, filter wheel radiometer walls) when the chopper blades are open.
- e_3 is the radiance seen by the detector emitted by components of the radiometer carriage that are not behind the chopper (e.g. the parabolic mirror).
- e_4 is the radiance seen by the detector emitted by the radiometer components that are behind the chopper (e.g. baffle, filter wheel radiometer walls) when the chopper blades are shut.
- e_5 is the radiance emitted by the chopper blades seen by the detector.

Provided the radiometer components behind the chopper (e.g. detector element, baffle, filter wheel and radiometer walls) do not change in temperature faster than the chopping speed then terms e_2 and e_4 will cancel out. Terms e_1, e_3 and e_5 will then contribute some of the chopped radiance measured by the detector. It is assumed that the radiometer will be calibrated relative to observing the radiance at an emission angle of zero degrees (i.e. looking straight down) and normalising all measurements at different emission angles to this measurement. This will give a measurement of relative emissivity at different observational angles. From equation 25 provided that the radiance contributions from the e_x terms remain constant, as the emission angle is varied any changes in the voltage output from the lock-in amplifier will be proportional to the DE of the sample. However, any changes to the contributions from the e_x terms as the emission angle is changed will create systematic error in the measurement.

The contribution from the e_1 term is controlled by the ambient temperature of the background surrounding the sample and the emissivity of the sample being measured (equation 27), the e_3 term is controlled by the emissivity and temperature of the parabolic collecting mirror (equation 28) and the e_5 term is controlled by the emissivity and temperature of the chopper blades (equation 29).

$$e_1 = \varepsilon_s \Omega \mathrm{R}_m \int_{\lambda_2}^{\lambda_1} B(\lambda, T_a) d\lambda \qquad 27$$

Where ε_s is the emissivity of the sample and T_a is the ambient temperature of the background surrounding the sample.

$$e_3 = \varepsilon_m \Omega \int_{\lambda_2}^{\lambda_1} B(\lambda, T_m) d\lambda \qquad 28$$

Where ε_m is the emissivity of the parabolic mirror and T_m is the temperature of the mirror.

$$e_5 = \varepsilon_c \Omega \int_{\lambda_2}^{\lambda_1} B(\lambda, T_c) d\lambda \qquad 29$$

Where ε_c is the emissivity of the chopper blades and T_c is the temperature of the chopper blades.

3.4 Radiometric Systematic Uncertainty Analysis

The values given in Table 3 By using the values given in Table 3 for the terms in equations 25 – 29, the systematic error introduced by small (<1 K) increases in the temperature values of the mirror, chopper and surrounding background were investigated. The values in Table 3 were used to calculate a lock-in voltage output that was then compared a lock-in voltage output calculated using the same values, but with small increases in the temperature values of the mirror, baffle and surrounding background (Table 5 and Table 6).

Table 3: Assumed values in equations 25 – 29 for calculating the systematic noise contributions from increases in the temperature of the parabolic mirror, baffle and surrounding background.

Term in equation 25	Value
Sample temperature (T_s)	350 K
Sample emissivity (ε_s)	0.8
Solid angle subtended by baffle (Ω)	7×10^{-4} sr
Reflectivity of parabolic mirror (R_m)	0.8
Ambient temperature (T_a)	290 K
Parabolic mirror temperature (T_m)	290 K
Emissivity of the chopper (ε_c)	1

Chopper temperature (T_c)	290 K
Cut on/off wavelength of filter (λ_1/λ_2)	0.2 – 25 µm

Table 4: Error introduced to the lock-in output by increases in the temperature of the chopper blades (e_5 term) and the mirror (e_3 term). The values were calculated using equation 25 and assuming the values given in Table 3.

Change in temperature	Error introduced by the mirror (e_3)	Error introduced by the chopper (e_5)
±0.5 K	0.2%	1.3%
±0.25 K	0.1%	0.7%
± 25 mK	0.01%	0.065%

Table 5: Error introduced to the radiometer system by increases in the temperature of the thermal background surrounding the sample (e_1 term in equation 25). The error values were calculated using equation 25 and the values given in Table 3 (except where otherwise stated).

Change in temperature	Error introduced by e_1 assuming a sample emissivity of 0.2	Error introduced by e_1 assuming a sample emissivity of 0.5	Error introduced by e_1 assuming a sample emissivity of 0.8
± 0.5 K	3%	1%	0.3%
± 0.25 K	1.5%	0.5%	0.1%
±25 mK	0.2%	0.05%	0.01%

From the values in Table 4 and Table 5 it is clear that for samples with an emissivity greater than 0.5 the dominant source of systematic noise is changes in the chopper temperature (e_5). From the Hapke BRDF model used to investigate the SNR requirements (section 3.1, Figure 34) the goniometer will be required to resolve features that are have a difference in emissivity of 0.1. Therefore the maximum tolerable error is 0.05 (at one sigma). For a sample that has an average lunar-like emissivity of 0.8, the maximum allowed error budget would therefore be 6.25%. To allow room for redundancy and other sources of error the maximum error introduced by temperature changes in the mirror, chopper and surrounding background should be less than 1%. The temperature of the radiometer instrument and the surrounding background should therefore be stable within ±0.25 K (Table 4 and Table 5).

3.5 Cold Shield Requirements for Measuring the Thermal and Far Infrared DE

It is important to note that if the temperature of the chopper and the mirror are measured and recorded then the e_3 and e_5 error terms could be removed mathematically after the measurement. However, the e_1 term will have an angular dependence that will make this correction difficult. To reduce the error from the reflected thermal background contribution (e_1 term in equation 25), the whole goniometer must be surrounded by a thermal shield at a constant temperature. The shield should have high emissivity (>0.9) to ensure that any radiance emitted by the sample, reflected off the shield and off the sample and then into the detector is negligible compare to the radiance emitted by the shield and reflected off the sample into the detector.

Provided the shield at ambient temperature (290 K) does not change by more than one Kelvin the systematic error will be small (between 0.3 – 3% from Table 5). The exact value of the systematic error then depends on the emissivity of the sample being measured, the smaller the emissivity the larger the error (Table 5). To reduce the error from changes in the reflected thermal background emission, the shield surrounding the experiment must be cooled. A cooling system (single stage cold head CoolPower 140 T available from Leyboid Vacuum, part number 842030, described in more detail in section 4.3) that is able to cool such a shield down to <150 K under vacuum (10^{-6} mbar) was available for this project. The systematic error introduced by changes in the reflected background thermal emission when the cold shield is at 150 K is calculated in Table 6. The error is very small (0.1%) even for low emissivity (0.2) samples. This low level of noise is not required for the goniometer system and provided the sample emissivity is not lower than 0.5 and the shield temperature is stable to 1 K, the shield is not required to be cooled to measure the pure emissivity.

Table 6: Error introduced to the radiometer system by increases in the temperature of the thermal background surrounding the sample (e_1 term in equation 25). The values were calculated using equation 25 and assuming the values given in Table 3, except for the ambient temperature, which was assumed that the whole goniometric system was surrounded by a cooled shield that was cooled to 150 K. This temperature stability is only need if the cold shield is not switched on the surrounding cold shield is at room temperature.

Change in temperature of thermal shield	Signal error introduced by e_1 assuming a sample emissivity of 0.2	Signal error introduced by e_1 assuming a sample emissivity of 0.5	Signal error introduced by e_1 assuming a sample emissivity of 0.8
±0.5 K	0.24%	0.06%	0.02%
±0.25 K	0.10%	0.03%	0.008%
±25 mK	0.01%	0.003%	0.0008%

However, on the lunar surface the vacuum and cold temperature of space induces a thermal gradient in the top few hundred microns of the lunar regolith that may change its scattering properties and it is known to effect the emission spectrum of the lunar regolith in the thermal infrared (Donaldson Hanna et al. 2012; Millán et al. 2011; Thomas et al. 2012). Therefore when measuring the re-radiated DE of a sample in the thermal and far infrared the cold shield and vacuum will be required to simulate the environment, space-like conditions, around the sample similar to that found at the lunar surface. Even a low-pressure (~5 mbar) atmosphere will allow gas between grains (in the sample) to transfer heat, so a high vacuum (10^{-6} mbar) is required to setup up a lunar-like thermal gradient across the sample. The cold shield is therefore not required for measuring the DE of solid samples or powdered samples under terrestrial conditions, but will be required for measuring powdered samples under lunar-like conditions, where the induced thermal gradient could affect the DE.

3.6 Maximum Allowed Thermal Gradient across Cold Shield

When the cold shield is cooled to 150 K there will be a thermal gradient between the top and the bottom, as the shield is cooled from the bottom. As the e_1 term is angular dependent it is important this thermal gradient is small as it will create systematic error in the DE measurement that cannot be removed mathematically. Using equation 25 and the values given in Table 3 the systematic error introduced by a thermal gradient (when the cold shield is cooled to <150 K) was approximated by calculating the systematic error introduced from changes in temperature of the whole cold shield. At 150 K the thermal gradient must be less than 30 K to keep the systematic error below 0.7% (Table 7) in the wavelength range 0.2 – 25 μm.

Table 7: Error introduced to the radiometer system by changes in temperature of the cold shield (e_1 term in equation 25). The values were calculated using equation 25 and assuming the values given in Table 3 (except the ambient temperature was assumed to be 150 K – the temperature of the cold shield). The error introduced was also calculated assuming a wavelength range of 100 – 400 µm, as this is the wavelength selection that will provide the greatest error (assuming Diviner filters are used – section 1.2).

Change in temperature of the cold shield initially at 150 K	Error introduced by e_1 assuming wavelength selection 0.2 – 25 µm	Error introduced by e_1 assuming wavelength selection 100 – 400 µm
± 15 K	0.7%	3.3%
± 10 K	0.41%	2.2%
± 5 K	0.18%	1.2%
± 2.5 K	0.08%	0.6%

The values in the first column in Table 7 were calculated assuming wavelength selection between 0.2 – 25 µm. The calculated systematic error is small (<0.7% for a temperature gradient of 30 K) because in the wavelength region 0.2 – 25 µm the emission from the hot sample dominates over the emission from the cold shield. The peak of the Planck emission function from the sample (350 K) is approximately 2.3 μm and the peak emission of the cold shield (150 K) is 19.3 μm. At longer wavelengths (>100 μm) the emitted radiance from the cold shield (150 K) is comparable to the radiance emitted from the sample (350 K) and therefore using the Diviner 100 – 400 μm (B6) filter the error introduced by changes in the temperature of the cold shield will be greatest. From the second column in Table 7, the thermal gradient should be less than 10 K to ensure the systematic error introduced from the reflected radiance is then less than 1.2% when using the 100 – 400 μm Diviner filter.

3.7 Sample Temperature Stability Requirements for Measuring the thermal infrared DE

Another systematic noise source in the goniometric system is due to the temperature stability of the sample being heated. Small changes in the sample temperature will cause changes in the output lock-in voltage signal in equation 25. Assuming a sample temperature of 350 K and the values given in Table 3, the error introduced by these changes has been calculated in Table 8. The sample temperature should be kept stable to ±0.25 K as this will introduce a 1% systematic noise that in combination with the error introduced by the temperature stability of the mirror (0.1% from Table 5), chopper (0.7% from Table 5) and cold shield (0.1% from Table 6) makes a total error budget of 1.9%.

Table 8: Error introduced to the radiometer system by increases in the temperature of the sample (E term in equation 25). The signal error percentages were calculated using equation 25 and the values in Table 3.

Change in temperature of the sample	Signal error introduced
± 0.5 K	2%
± 0.25 K	1%
±25 mK	0.1%

3.8 Frequency Stability

The final noise source considered is the frequency stability of the chopper. The responsivity ($\bar{R}$ term in equation 25) of the detector and system will depend on the chopping rate. For example if the pyroelectric detector LIE-332f-66 is used for thermal infrared DE measurements then the relative responsivity of the detector will decrease with increasing chopping frequency (from 100% at 1 Hz to 30% at 10 Hz, Figure 38). The frequency stability of the chopper is therefore important as small changes in the chopping frequency will introduce a systematic error in the output of the lock-in amplifier. Using the values given in Table 3 and assuming the signal is chopped at 10 Hz, the error introduced to the system by small increases in the chopper frequency is investigated in Table 9. The frequency of the chopper should be kept stable to within ±0.05 Hz to ensure the error introduced by changes in the responsivity of the system is less than 1% (Table 9). Alternatively, the frequency of the chopper could be recorded and the detector output can be mathematically corrected to account for changes in the frequency of chopper. Assuming no mathematical correction is applied and the chopper frequency is stable to within ±0.05 Hz the total error budget including the temperature stability is 2.9%.

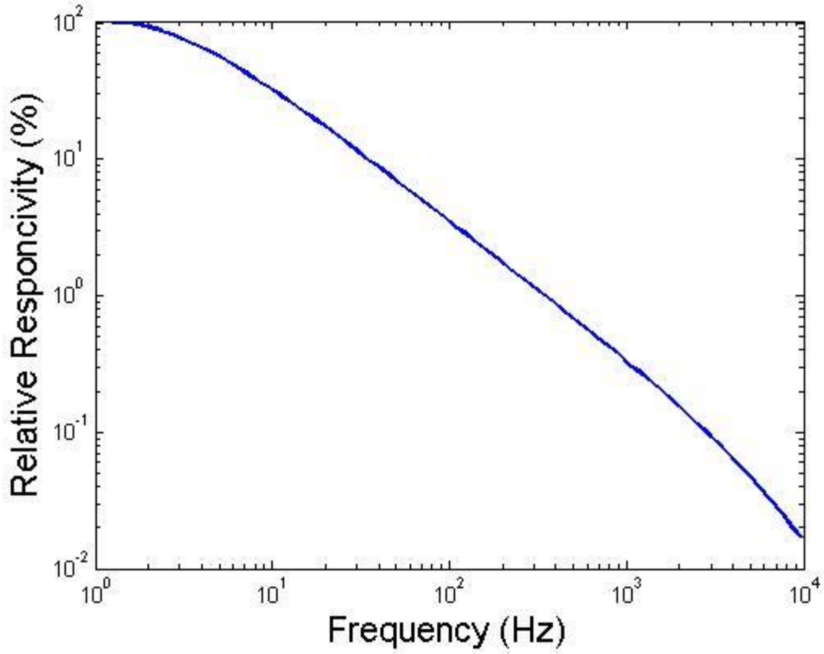

Figure 38: Responsivity of the LIE-332f-66 detector with chopping frequency. After (InfraTec 2015)**.**

Table 9: Error introduced to the radiometric system by small increases in chopper frequency. The error percentages were calculated using equation 25 and the values given in Table 3. The chopper frequency was assumed to be 10 Hz and the responsivity of the system at a given chopper frequency was taken from Figure 38.

Change in frequency of chopping rate	Signal error introduced
+Δ0.01 Hz	0.09%
+Δ0.1 Hz	0.9%
+Δ0.2 Hz	1.8%

3.9 Summary of Requirements for a Goniometer to Explore the Thermal Infrared DE and Visible BRDF

Table 10 gives a science requirements traceability matrix of the requirements of a visible and thermal/far infrared goniometer. In order to fully explore the anisotropic scattering from lunar regolith samples across wavelengths from the visible to the thermal/far infrared, a goniometer is required to have the following:

- The goniometer must be able to measure as full as possible a BRDF/DE for all angles. Of particular importance is that the goniometer must be able to make measurements at low phase angles, so it is able to measure the opposition effect, as described in section 1.5.1.2. The angular accuracy must be at least 0.5^o and the signal to noise ratio must be greater than 30 for the goniometer to see the opposition effect.

- The goniometer must be able to use Diviner spare filters (or filters of a similar wavelength) for wavelength selection, to make the DE as comparable as possible to the Diviner data set.
- The goniometer and sample must be surrounded by a high emissivity cold shield (<150K) to simulate cold space and help setup a lunar-like thermal gradient across the top few hundred microns of the sample. The cold shield will also help to reduce the background thermal contribution.
- The cold shield must be kept inside a vacuum chamber ($<10^{-6}$ mbar), to enable the cold head to cool the cold shield and avoid condensation. To cool the cold shied, the cold head temperature will be of the order 70 K, which is cold enough to condense water and N_2. The vacuum is also required to help setup a thermal gradient across the top few hundred microns of the sample by preventing convection between soil grains.
- The thermal gradient between the top and the bottom of the cold shield must be less than 10 K.
- At an emission angle of zero degrees, the FOV should be a well-defined circle.
- The FOV of the radiometer must be smaller than the diameter of the sample at all emission angles.

- The centre of the FOV of the radiometer should not move across the surface of the sample as the emission or phase angle is varied. As a minimum the FOV must always stay on the surface of the sample for all emission and phase angles.
- If no mathematical correction is applied the temperature stability of the heated sample must be within ±0.25 K.
- If no mathematical correction is applied the temperature stability of the radiometer carriage and all components on the radiometer carriage must be within ±0.25 K.
- If no mathematical correction is applied the stability of the chopper must be controlled to ±0.05 Hz.

Table 10: Traceability matrix mapping the science to the measurement requirements.

			Measurement Requirements											
Science Goal	**Science Objective**	**Measurement Goal**	**Light Source required**	**Angular range**			**Angular accuracy**	**SNR**	**Cold shield temperature and Vacuum pressure**	**Radiometer carriage temperature stability**	**Wavelength range**	**Sample temperature**	**Sample temperature accuracy**	**Output Data Product**
Understand surface temperature of airless bodies and the connection to thermal physical properties and topography				Phase	Emission	Incident								
	Improve accuracy of three-dimensional thermal physical models by measuring realistic scattering of lunar analogues	Measure pure DE of lunar analogue material	No	One phase angle	0-90°	NA	0.5°	30	290 K at atmospheric pressure	1K	1-100 µm Using Diviner flight spare filters	300-400 K	0.1 K	Emissivity measurements at different emission angles
		Measure re-radiated DE of lunar analogue material	Yes	0-360°	0-90°	0-90°	0.5°	30	<150 K under 10^{-6} mbar pressure	1K	1-100 µm Using Diviner flight spare filters	300-400 K	0.1 K	Emissivity measurements at different phase, incident and emission angles
Remote sensing data to airless bodies surface physical properties	Understand light scattering properties of airless bodies	Measure BRDF of lunar analogue materials	Yes	0-360°	0-90°	0-90°	0.5°	30	Not required	NA	0.4-1 µm	NA	NA	BRDF measurements at different emission, phase and incident angles

4 Design and Development of a fully Automated Vacuum Compatible Goniometer

This chapter describes the design and development of the Oxford Space Environment Goniometer (OSEG) from the requirements outlined in section 3. At the start of this project only the vacuum chamber was available all other goniometer components described in this section were developed by the Author for this project.

4.1 General Design Overview

To meet the requirements in section 3, the goniometer was designed to be an automated three-axis system, providing motion in the incidence, emission and phase angles (Figure 40). This allows an entire half hemisphere of scattering geometries to be measured. The goniometer was constructed to fit inside a one meter diameter vacuum chamber and be surrounded by a cold shield as detailed in the requirements (section 3.5). All the mechanical moving parts of the goniometer are set up on a base plate, which sits on glass fibre legs 10 cm above the cold shield, thermally isolating the mechanical moving parts from the cold shield. For clarity in this report the design and construction of the goniometer has been split into five different subsystems:

1. Mechanical parts, section 4.2.
2. Cold Shield and Vacuum Chamber, section 4.3.
3. Radiometer Carriage, section 4.4.
4. Sample Changer, section 4.5
5. Light Source, section 4.6.

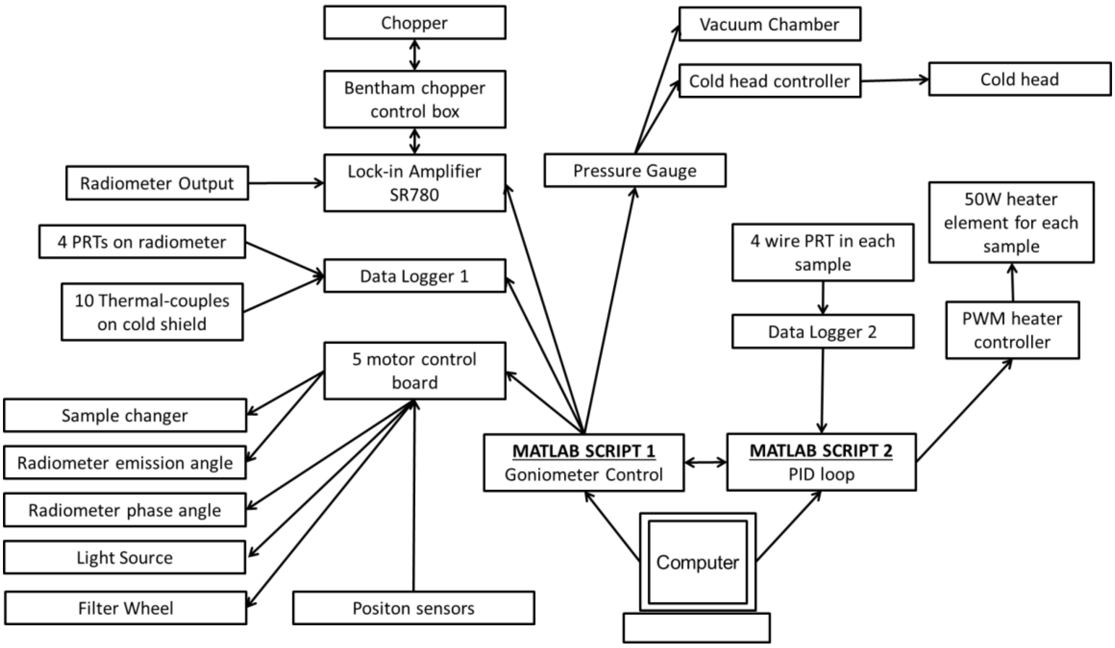

Figure 39 : Overview of the OSEG electrical subsystems

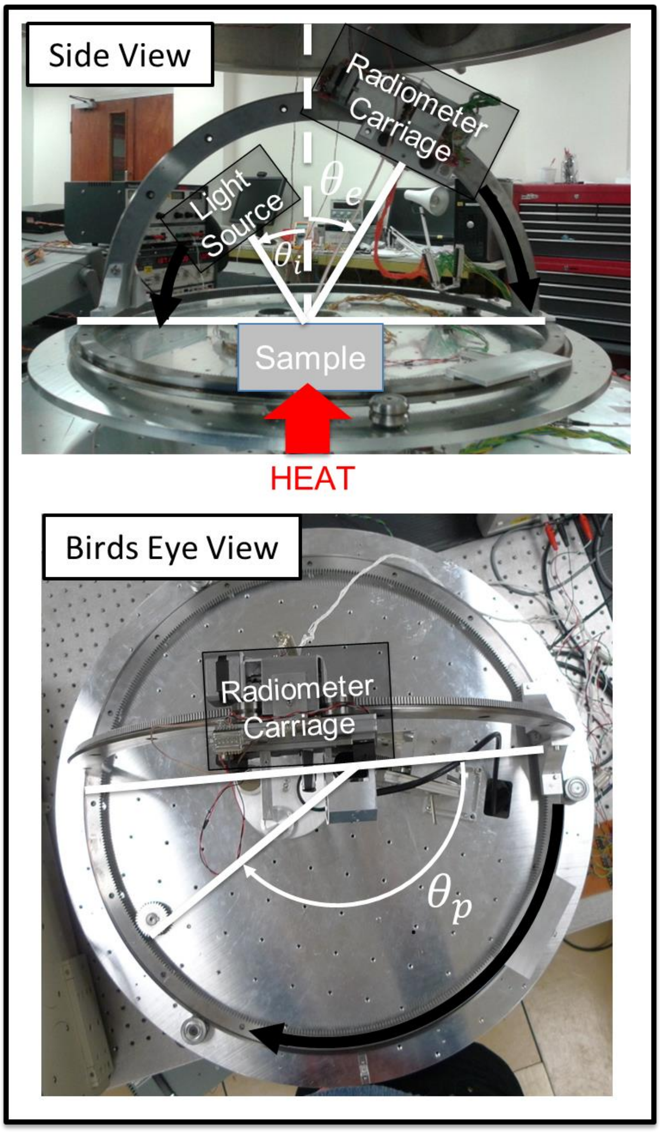

Figure 40: OSEG setup on an optical bench showing the movement of the two arms allowing the angle of incidence θ_i , emission θ_e and phase θ_p to be changed.

4.2 Mechanical Parts

A total of five stepper motors are used to control the movement of the goniometer, one for controlling the phase angle, emission angle, incidence angle, sample changer and filter wheel. All the stepper motors are controlled by a custom-built stepper motor control board that interfaces by RS232 with a computer (Appendix 1). A custom Matlab graphical user interface (GUI) has been built to control the goniometer movement.

- Phase angle movement – Provided by a 360^{o} ring mounted on a base plate, which rotates in both directions around the sample cup in the centre of the ring. The size of the ring (0.65 m) was dictated by the size of the vacuum chamber (1 m) that the goniometer must fit inside.
- Emission angle movement – Provided by a 180^{o} segment ring placed vertically on top of the 360^{o} ring (Figure 40). The radiometer (section 4.4) is mounted onto a carriage, which is able to run up and down the 180^{o} segment.
- Incidence angle movement - Inside the 360^{o} ring a 90^{o} segment is attached to the base plate. The light source will be mounted on a carriage that can move up and down the 90^{o} segment. It was decided that as the light source would require cooling pipes (section 4.6) when under vacuum, the light source would be fixed and the radiometer would rotate, to enable the phase angle to be changed.

4.3 Vacuum Chamber and Cold Shield

As outlined in the requirements of the goniometer (section 3), the goniometer is surrounded by a high emissivity cold shield (capable of cooling to <150 K), cooled by a 140 W cold head (Leyboid Vacuum CoolPower 140T, part number

842030) and housed inside a <10^{-6} mbar one meter diameter vacuum chamber (Figure 41). To increase the emissivity of the cold shield the inside was spray painted with high emissivity (>0.95 across wavelengths 0.2 – 25 µm) Nextel black paint. As outlined in the requirements the cold shield must have a thermal gradient between the top and bottom of less than 10 K and must be able to cool in sufficient time (<12 hours to allow the whole experiment to be cooled overnight). The wall thickness of the thermal shield is therefore important as the thicker the walls the smaller the thermal gradient, but the longer the longer the shield will take to cool. The maximum thickness an aluminium cold shield could be manufactured using the standard technique of rolling was 6 mm.

Figure 41: Photographs showing thermal infrared setup. (Left) The OSEG setup inside the vacuum chamber without the cold shield surrounding it. (Right) the cold shield surround in 10 layers of multilayer insulation (MLI) house inside the vacuum chamber.

4.3.1 Model of the Time Taken for the Cold Shield to Cool

Before the cold shield was constructed an analytical model was used to check that the whole shield (with 6 mm walls) could be cooled to <150 K in a reasonable amount of time (<12 hours). Assuming there is no thermal resistance from any thermal joints the time it takes for the cold shield (with 6 mm walls) to cool down to 150 K can be estimated from equation 30 as 12 hours.

$$Time = \frac{C_{AL} V_{CS} \rho \Delta T}{P_{CH}} \qquad \textbf{30}$$

Where: C_{AL} is the specific heat capacity for aluminium (897 J/kgK), V_{Cs} is the volume of the cold shield (17.4 cm^3), ρ is the density of aluminium (2700 kg/m^3), ΔT is the difference between the initial temperature of the cold shield (room temperature) and the temperature it is cooled to (150 K) and P_{CH} is the cooling power of the cold head (140 W).

4.3.2 Model of Thermal Gradient across Cold Shield

A temperature gradient across the cold shield will be formed as the cold shield is cooled from below and thermal emission from the surrounding vacuum chamber walls heat the walls of the cold shield (Figure 42). From the requirements (section 3.5) the thermal gradient should be less than 10 K. The temperature gradient across the cold shield can be calculated using equation 31 as approximately 4.2 K.

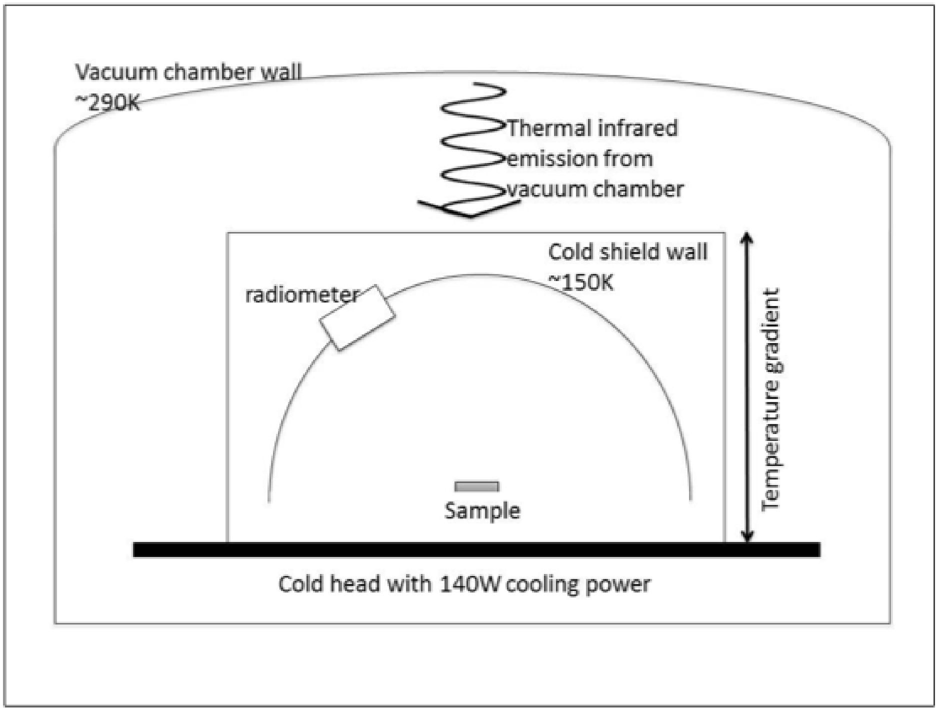

Figure 42: Two dimensional diagram of the OSEG inside the cold shield and vacuum chamber displaying the thermal gradient between the top and the bottom of the cold shield. The thermal gradient is formed by infrared emission from the vacuum chamber walls warming the walls of the cold shield. To reduce this effect the outside of the cold shield will be covered in a multilayer insulation (MLI) blanket (Figure 41).

$$\Delta T = \frac{\Delta Q L_{CS}}{A\alpha_c} \quad \mathbf{31}$$

Where α_c is the thermal conductivity of aluminium (170 W/mK), A is the cross-sectional area of the cold shield walls (260 cm^2), ΔT is the thermal gradient across the cold shield, L_{CS} is the length of the cold shield walls (480 mm) and ΔQ (39 W) is the radiative power on the top of the cold shield that can be estimated from equation 32.

$$\Delta Q = \varepsilon\sigma(T_{vacuum}^4 - T_{coldshield}^4) \quad (32)$$

Where ε is the emissivity of 10 layers of multilayer insulation blanket (approximately 0.1 (Finckenor & Dooling 1999)), σ is the Stephan-Boltzmann constant and T_{vacuum} is the temperature of the vacuum chamber walls (294 K) and $T_{coldshield}$ is the temperature of the cold head (150 K).

Equations 30 and 31 are approximations assuming that the shape of the aluminium cold shield has no effect on the cooling. To accurately model the temperature gradient across the cold shield a finite element thermal model was made in the multi-physics package COMSOL. The bottom surface was constrained to a temperature of 150 K and the whole shield was surrounded by a vacuum chamber at 290 K. Radiation effects from the vacuum chamber walls were taken into account and the initial temperature was set to 290 K. The model results suggested that the difference between the top and bottom of the cold shield would be approximately 3 K for an aluminium cold shield with 6 mm thick walls (Figure 43).

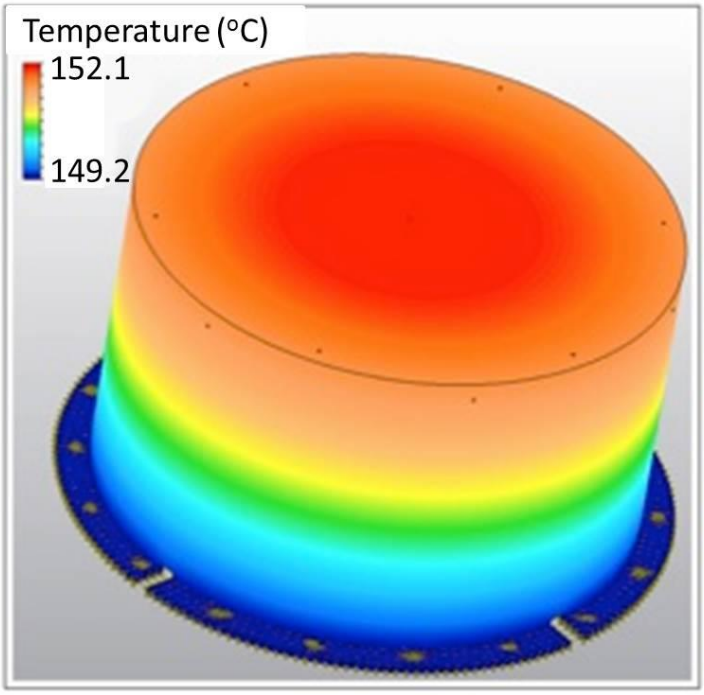

Figure 43: Results of the thermal model of the cold shield, showing the thermal gradient between the top and bottom of the cold shield is less than 3 K.

4.3.3 Cold Shield Cooling Test

A dry run evacuating the chamber and cooling the cold shield was performed to test the modelling accuracy and to ensure the thermal gradient is smaller than the 10 K outlined in the requirements. The cold shield is constructed of three parts (Figure 44):

1. An aluminium plate that is attached directly to the cold head.

2. A second aluminium plate that forms the base of the cold shield is screwed onto the first plate.
3. The cylindrical cold shield and flange are screwed onto the base plate.

At each interface between different parts of the cold shield, vacuum compatible thermal grease (Apiezon “N”) was used to ensure good thermal contact. The cold shield was placed inside the vacuum chamber and K-type thermal couples were place around each part of the cold shield to record the temperature (the position of each thermal couple is shown in Figure 44). The vacuum chamber was evacuated to 10^{-6} mbar, the cold head was turned on and left overnight, and temperature recordings of each thermal couple were made at one-minute intervals (Figure 45).

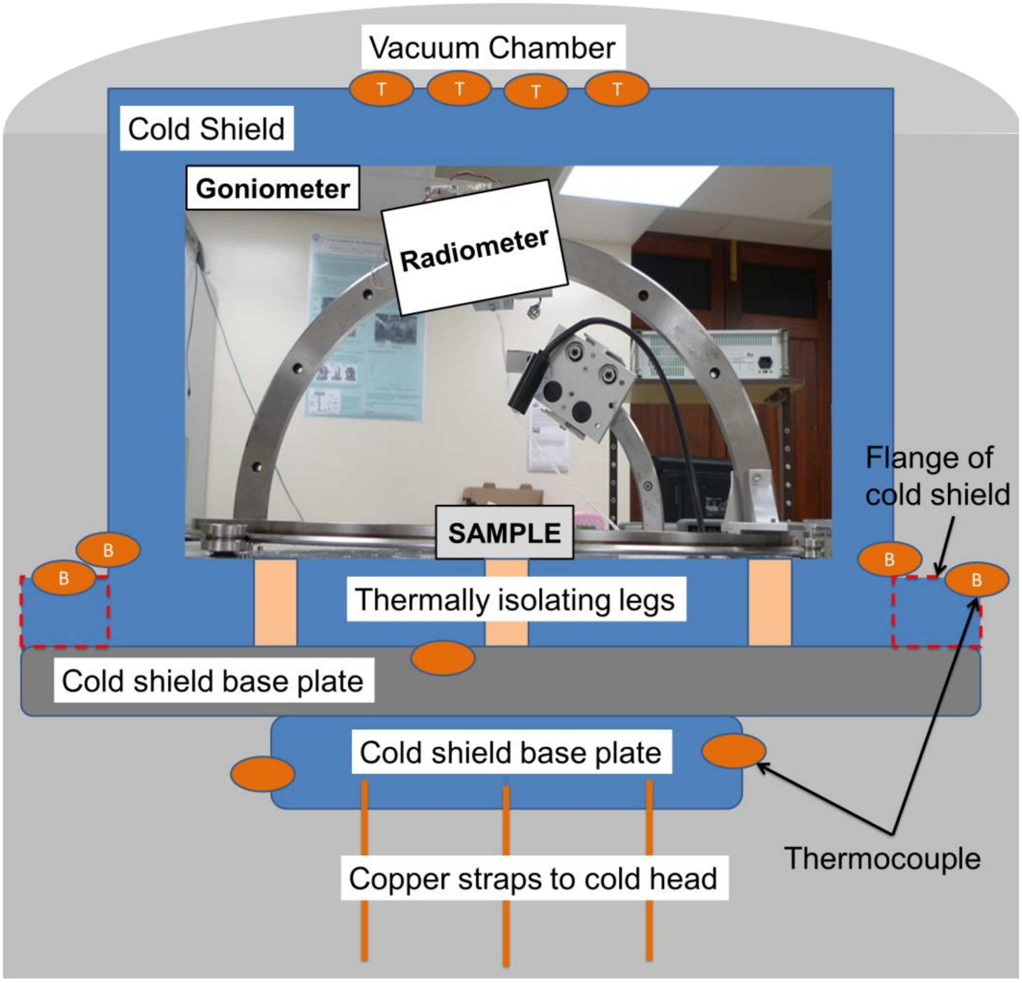

Figure 44: Each component of the cold shield inside the vacuum chamber and the location of the thermal couples used to monitor the temperature of the cold shield. Four thermal couples where placed at the top of the cold shield (T) and four around the base (B).

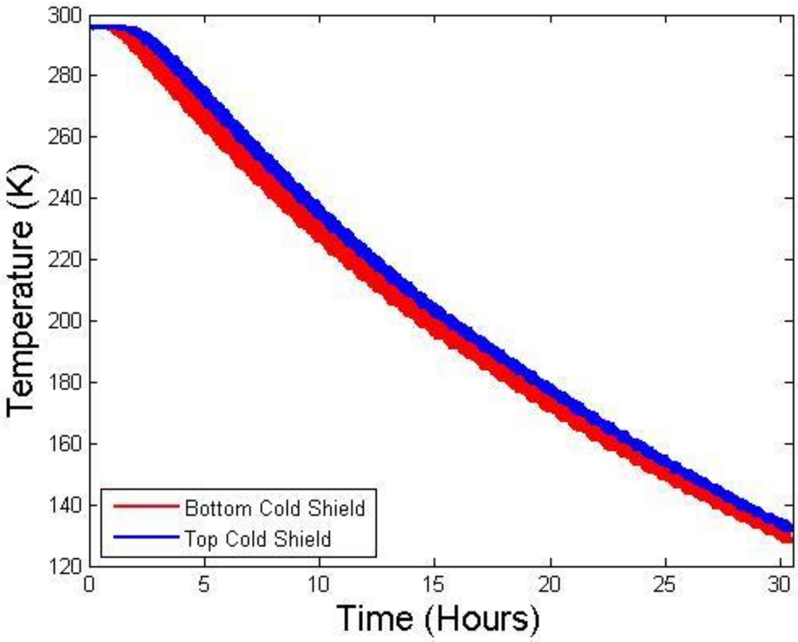

Figure 45: Temperature recordings of K-type thermal couples placed at the top and bottom of the cold shield as the whole system was cooled inside a 10^{-6}mbar vacuum. The readings from four thermal couples were averaged together at both the top and the bottom of the shield. The error bar is represented by the thickness of the line and is taken to be the standard deviation between the four measurements. The location of each thermal couple can be seen in Figure 44.

After 30 hours of cooling there is a 2.1 ±1 K temperature gradient between the top of the cold shield and the bottom of the cold shield's flange. This is in reasonable agreement with the model, which suggested a temperature gradient of 3 K. The slight difference between the model and measured temperature gradient could be due to inaccuracy in the assumed thermal conductivity of aluminium.

4.4 Radiometer

As outlined in the requirements the radiometer carriage must be able to move over as large as possible range of emission and phase angles and take measurements from the visible to the far infrared using spare Diviner filters to make the measurements as comparable as possible to the Diviner measurements. To meet the requirements the radiometer was designed in a modular fashion to allow as wide a range of wavelength selection as possible. It was tested to show that it meets all the requirements laid out in section 3:

- The radiometers projected FOV should be a uniform circle at an emission angle of zero (tested in section 4.4.4).
- The FOV must be smaller than the diameter of the sample at all emission angles and should not move across the sample (tested in section 4.4.5).
- The thermal stability of the radiometer instrument should be within ± 0.25 K (tested in section 4.4.6).
- The angular accuracy should be $<0.5^{o}$ (tested in section 4.4.7).
- The signal to noise should be 30 (tested in section 4.4.8)
- The frequency stability of the chopper should be within ± 0.05 Hz (tested in section 4.4.9)

4.4.1 General Optical Design

A modular radiometer carriage (Figure 47 and Figure 48) was built with defined mechanical interfaces including a detachable: baffle, filter wheel, chopper, 90-degree off-axis parabolic mirror and detector element (CAD model given in Appendix 4). The off-axis parabolic mirror (Edmond optics #47-105) has a broadband reflectance (>85% between 0.1 – 25 μm) and an effective focal length of 76.2 mm. It collects radiation reflected from the sample, reflects it through 90 degrees and focuses it onto the detector element. The detector output is connected to a trans-impedance pre-amplifier (Appendix 2) before being connected to the input of a lock-in amplifier. The demodulated output from the lock-in amplifier is then recorded on a computer (Figure 46).

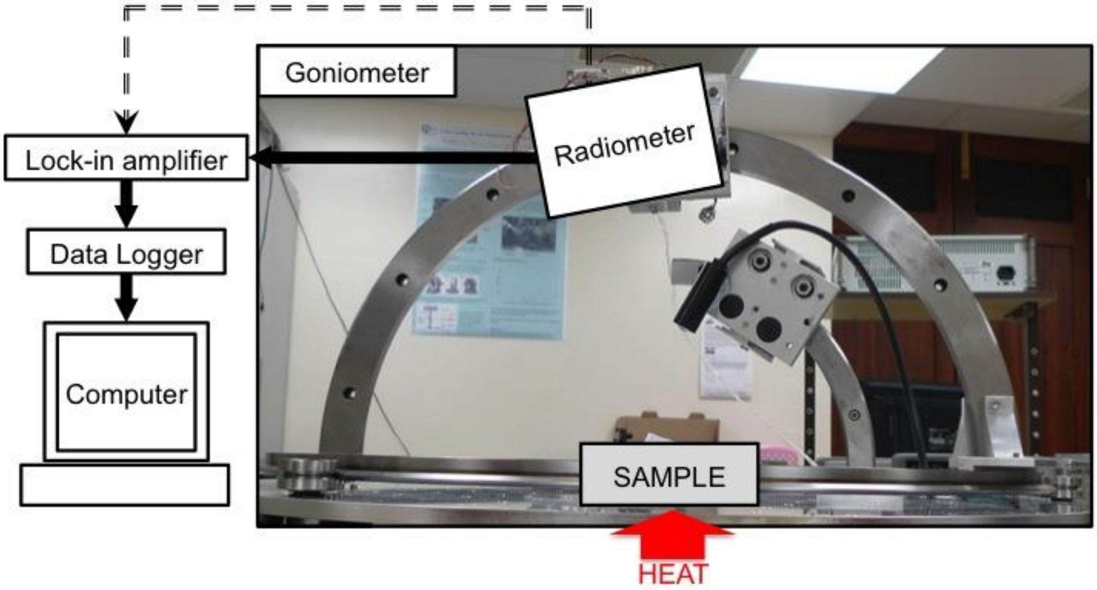

Figure 46: Block diagram of the OSEG setup to measure the DE of a sample.

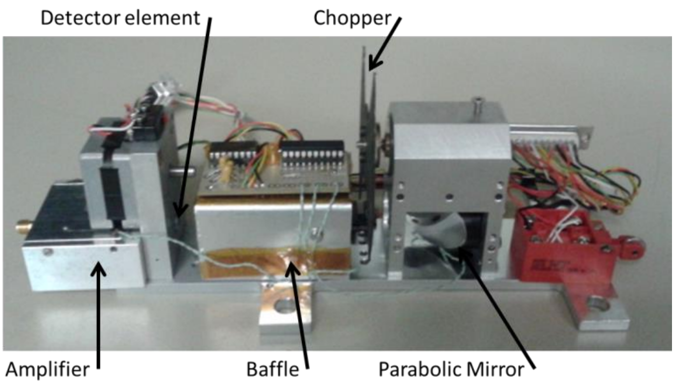

Figure 47: Image of the radiometer carriage with parts labelled.

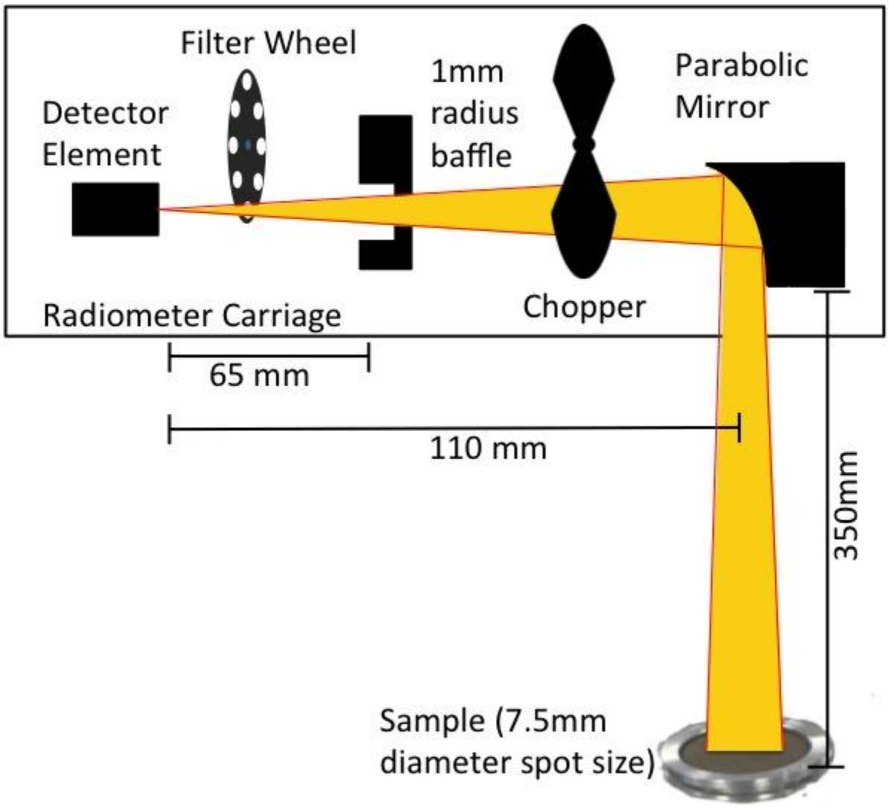

Figure 48: Block diagram of the radiometer carriage.

As outlined in the requirements for both BRDF and DE measurements the signal is chopped to reduce the background noise. When measuring the BRDF of a sample a lock-in amplifier is used in combination with a chopped light source to remove the background noise from the experiment (Pommerol et al. 2011). For DE measurements as the surface emission is being measured the light source cannot be chopped hence the chopping is performed on the radiometer carriage. This removes the thermal background noise from the all the radiometer components behind the chopper.

4.4.2 Radiometer Wavelength Selection

From the requirements the radiometer instrument should be able to make measurements in a broad wavelength region (visible – far infrared, 400 nm – 400 μm) by substituting the detector element and filters used. For measuring the BRDF of samples in the visible a photodiode (RS stock number 303-719) is used as the detector element (Figure 48). This photodiode was chosen because it was cheap (£7.20) and had wavelength responsivity in the visible region between 400 – 700 nm. For measuring the DE of samples in the thermal/far infrared a high performance pyroelectric detector (Infratec LIE-332F) is used. From the requirements the radiometer should be able to make measurements using the Diviner filters for wavelength selection. However, the wavelength selection of the radiometer is limited by the transmission of the potassium bromide (KBr) window on the front of the detector element can. The transmission of the KBr window rolls off significantly between 20 – 30 μm (Figure 49), hence only the Diviner filters A2-A6 (8 – 25 μm) can be used. To use the longer wavelength B1-B3 (25 – 400 μm) Diviner filters a new detector element with a matching window response will be required.

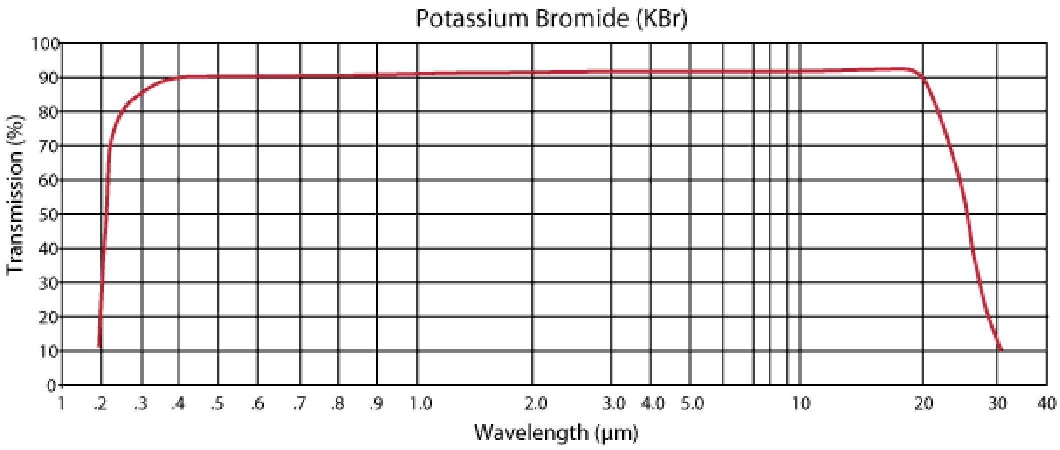

Figure 49: Potassium Bromide (KBr) transmission spectrum on the front of the Infratec LIE-332F detector that rolls off significantly between 20 – 30 μm (InfraTec 2015)**.**

4.4.3 Radiometer's Field of View

From the requirements the radiometer's FOV projected onto the sample must smaller than the diameter of the sample for all emission angles. As the radiometer carriage moves down towards the baseplate increasing the emission angle, the FOV of the radiometer will become ellipsoidal and the semi-major axis will increase proportional to the cosine of the emission angle. Hence at 75^{o} (the maximum emission of the OSEG) the semi-major axis of the FOV must not exceed 50 mm (the diameter of the sample cup). Therefore at an emission angle of zero, the FOV projected onto the sample should not be greater than 12.9 mm.

To create a FOV smaller than 12.9 mm, the detector element is positioned 33.8 mm beyond the effective focal length (76.2 mm) of the parabolic mirror. This creates a slightly converging (0.4^{o}) input beam from the target into the collecting mirror. To constrain the spot size on the parabolic mirror a baffle is placed 65 mm away from the detector element. As the target is ~350 mm away from the mirror, the size of the radiometer's FOV projected onto the target can be calculated using equation 33 and some basic geometry as 7.7 mm. A summary of the optical design of the radiometer instrument can be found in Table 11.

$$\frac{1}{\bar{f}} = \frac{1}{u} + \frac{1}{v} \qquad \textbf{33}$$

Where $\bar{f}$ is the effective focal length of the mirror, u is the distance between the mirror and the detector element and v is the distance between the mirror and the focal point of the optical design.

Table 11: Key parameters in the optical design for the radiometer instrument.

Design Parameter of Radiometer Instrument	Value
Distance between detector and mirror	110 mm
Distance between detector and baffle	65 mm
Diameter of baffle	2 mm
Working spot diameter on mirror	3.4 mm
Divergence of beam	0.37 ^{o}
Effective focal length of mirror	76.2 mm
Object distance from parabolic mirror	248 mm
Distance between target and mirror	350 mm
FOV on target	7.7 mm

4.4.4 Mapping the Radiometer's FOV

The requirements specify that the radiometer's FOV should be a well-defined uniform circle at an emission angle of 0^o. To ensure the specification was met, the radiometer's FOV was mapped out in the thermal infrared by measuring the change in radiation incident on the detector element as a pinhole thermal infrared source was scanned across the FOV at a distance of 400 mm from the parabolic mirror. A hot wire was mounted behind a pinhole on a two-axis jig (Figure 50). Two precision stepper motors controlled the jig, one stepper motor moving the thermal infrared pinhole source in the y direction and the other in the x direction. A Matlab script was then used to scan the pinhole in steps of 0.5 mm in the x and y direction to map out the FOV of the radiometer carriage.

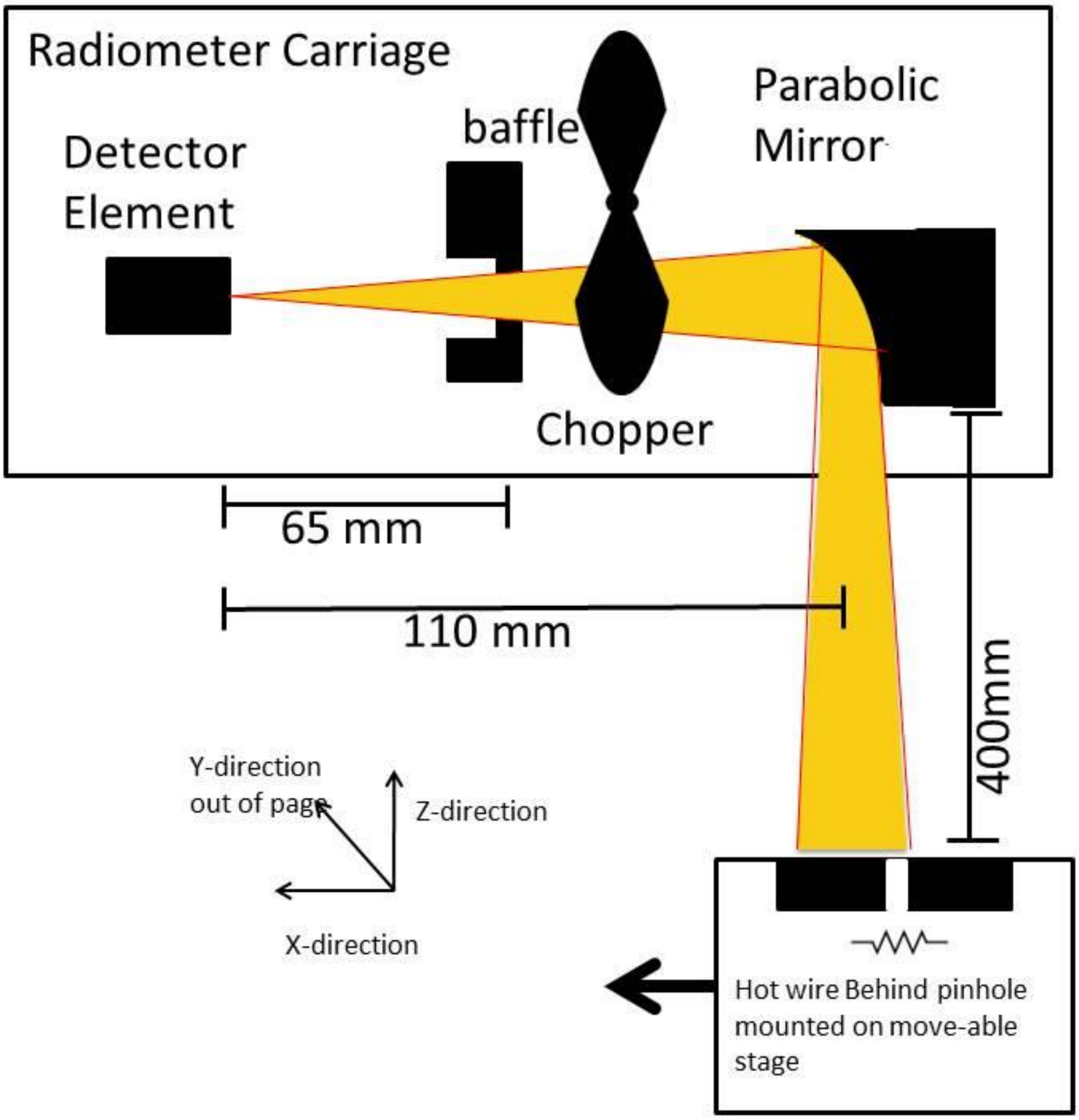

Figure 50: Setup used to map the FOV of the radiometer carriage in the thermal infrared.

The initial design for the radiometer carriage used a large baffle allowing the most of the parabolic mirror to be utilised, the detector element was placed near the effective focal length of the parabolic mirror (76.2 mm) creating a near collimated input beam. However, it was found that that the FOV followed the shape of the parabolic mirror (Figure 51). This result was expected due to the amount of cromatic aberration from all the off-axis rays on the parabolic mirror. The baffle was then made smaller to reduce the amount of the parabolic mirror being used, the detector element was moved 33.8 mm beyond the effective focal length of the parabolic mirror to create a slightly diverging input beam and a projected FOV on the sample of ~7.7 mm.

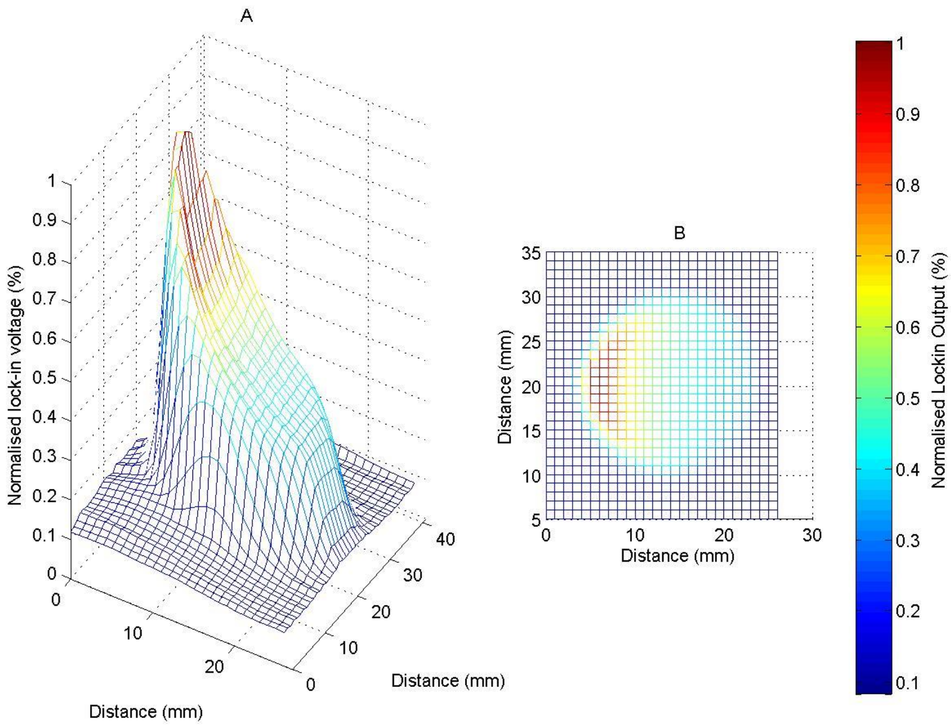

Figure 51: Mapped FOV of the radiometer carriage with a large baffle. As can be seen the FOV follows the shape of the parabolic mirror.

Repeating the process with the smaller baffle (2 mm diameter) the FOV has been shown to be circular with a diameter of 10 mm (Figure 52). This meets the requirements (section 3.2) as the FOV is a well-defined circle at an emission angle of zero and is smaller than the sample at all emission angles (at the maximum emission angle of 75^{o} the FOV will be 38.6 mm).

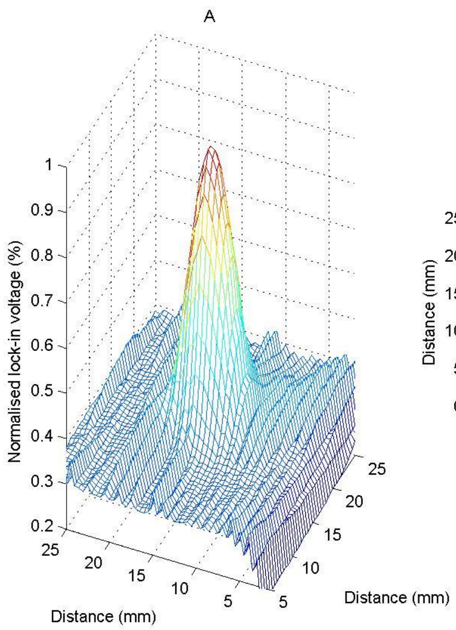

Figure 52: Mapped FOV of the radiometer carriage at 0^{o} emission angle. The FOV is a near perfect circle with a diameter of approximately 10mm.

4.4.5 Measuring the Movement of the Projected FOV across the Sample.

From the requirements the radiometer carriage must be aligned accurately, such that the centre of the detectors' FOV does not move across the surface of the sample as the emission angle is changed. To check the alignment of the radiometer carriage, the detector element was replaced with a visible light emitting diode (LED) and baffle. The baffle was made to be the same shape and size as the surface area of the photodiode and pyroelectric detector. This arrangement then allowed the FOV of the detector to be projected onto the sample. A web-camera was then setup such that it could observe the whole sample to record the projected FOV, as the radiometer carriage was moved around the sample (Figure 53).

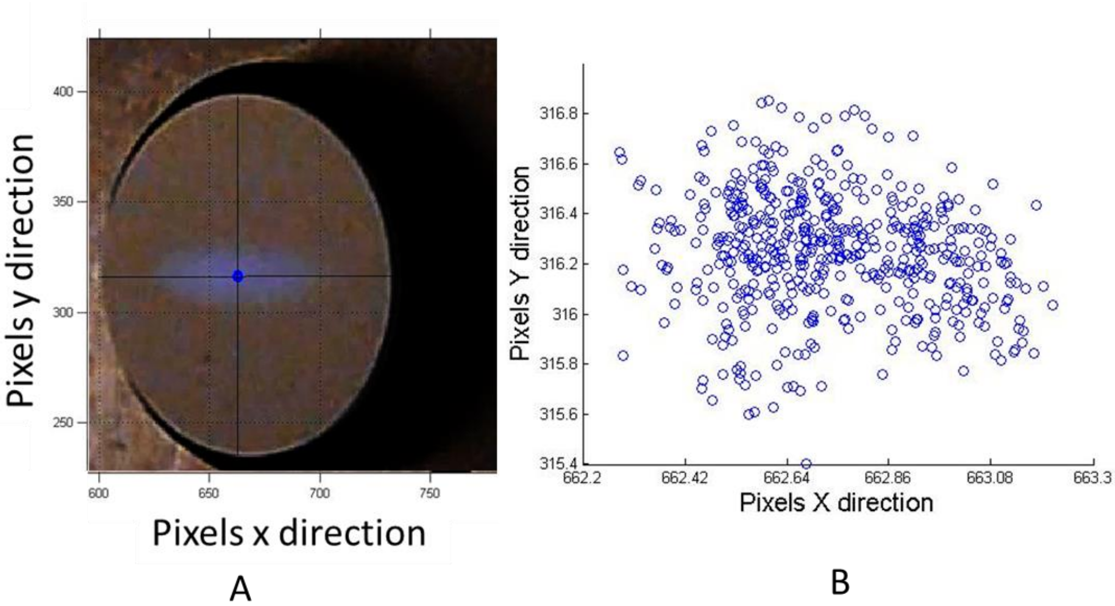

Figure 53: (A) A sequence of one hundred images was taken by a stationary web camera of the Spectralon target as the radiometer carriage was moved to different emission angles (0^o-72^o emission angle). For each image the FOV of the radiometer was projected onto the Spectralon target using a visible LED in place of the detector element. A blue circle shows the calculated centre of the FOV of the detector element for each frame. As the radiometer carriage was moved the centre of the FOV was found to move by 1.502 pixels in the x direction

and 0.9331 pixels in the y direction. The diameter of the Spectralon target is 133 and 164 pixels in the x and y directions respectively. As the diameter of the Spectralon target is 50 mm, this can be used to calculate the movement of the FOV in the x and y directions as 0.56 and 0.28 mm respectively. (B) shows a close up of the centre of the Spectralon target shown in (A).

Each frame was loaded into Matlab and analysed using the Matlab image processing toolbox to highlight the FOV projected onto the sample and calculate its geographic centre. Between each frame the centre could be seen to move by a few pixels (1.8 pixels) in the x and (0.93 pixels) y direction. The x direction was aligned in the same plane of motion as the radiometer carriage was moved to vary the emission angle. Pixels were converted into millimeters by normalising using the diameter of the sample (50 mm) in the x and y directions showing that the FOV moved <0.8 mm (Figure 53), giving confidence that the radiometer carriage is aligned correctly. This meets the requirement as with a 38.6 mm projected FOV size at an emission angle of 75^{o}, a movement <0.8 mm will ensure that the entire FOV is inside the sample (50 mm in diameter).

4.4.6 Thermal Control of the Radiometer Instrument

The requirements (section 3.3) specify that the temperature of the radiometer, parabolic mirror and chopper should be kept constant to ±0.25 K to ensure the noise introduced to the measurement is small enough to be able to resolve features 0.1 in emissivity in the DE. No active thermal control is used on the radiometer carriage, but the radiometer is covered in 10 layers of multilayer insulation (MLI) to minimise temperature changes when under vacuum. Three four-wire Platinum Resistance Temperature (PRT) sensors are then used to monitor the temperature of the mirror, baffle and detector element housing to ensure that the temperature stability requirement (±0.25 K) is met. During measurements of Nextel targets (described in section 6) the maximum temperature change on the radiometer carriage as the emission angle was varied between 0^o and 72^o was measured to be ±0.15 K, 0.2 K better than the requirement.

4.4.7 Measurement of the Mechanical Angular Accuracy of the Radiometer Carriage Movement

From the requirements (section 3.1) the mechanical angular accuracy of the goniometer must be at least 0.5^o to resolve the expected angular width of the opposition surge of Apollo soil samples. To measure the radiometer's angular accuracy, the goniometer was setup as shown in Figure 54 and Figure 55. Spectralon (a standard BRDF reference target in the visible – see section 8) was used as the target sample and the goniometer's radiometer carriage was moved to seven different locations each 5.7^o apart. The time constant on the lock-in amplifier was set to one second and at each location there was a thirty second pause to allow the lock-in output to settle (this is the recommended settling time for a time constant of one second using the SR830 Stanford

Research lock-in amplifier (Stanford Research Systems 2011)), before the lock-in amplifier was read by the computer. This procedure was repeated eight times, each time the radiometer carriage was moved to the same seven locations. The results are plotted in Figure 56; the output of the lock-in recorded was nearly identical (>99.5%) for each emission angle for the eight times it was repeated.

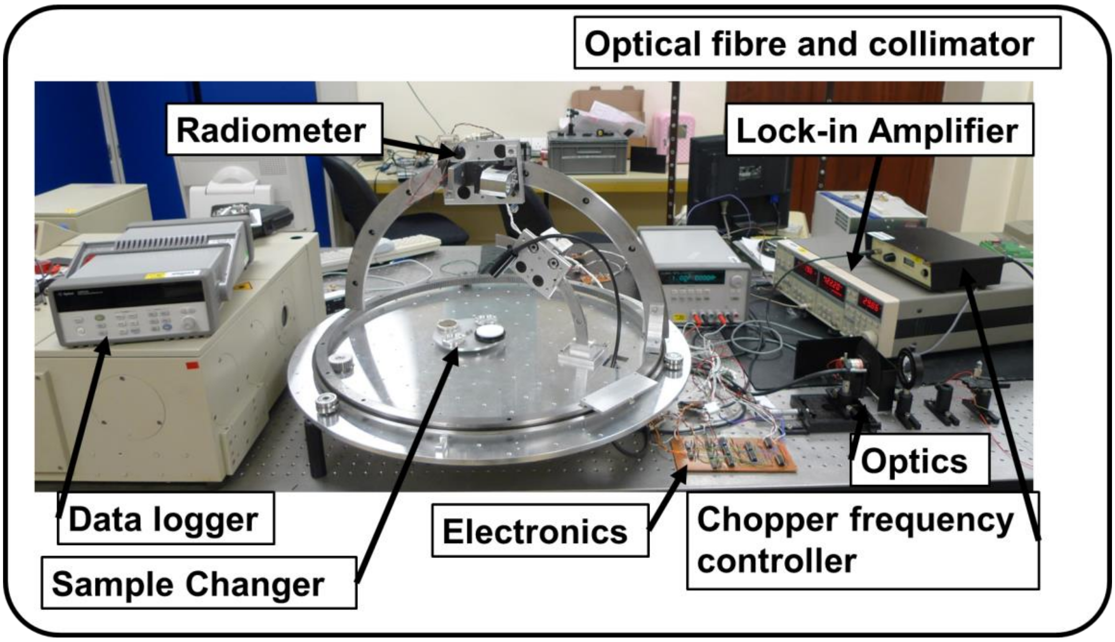

Figure 54: OSEG setup on an optical bench ready to make BRDF measurements of a Spectralon target, with labels displaying each part.

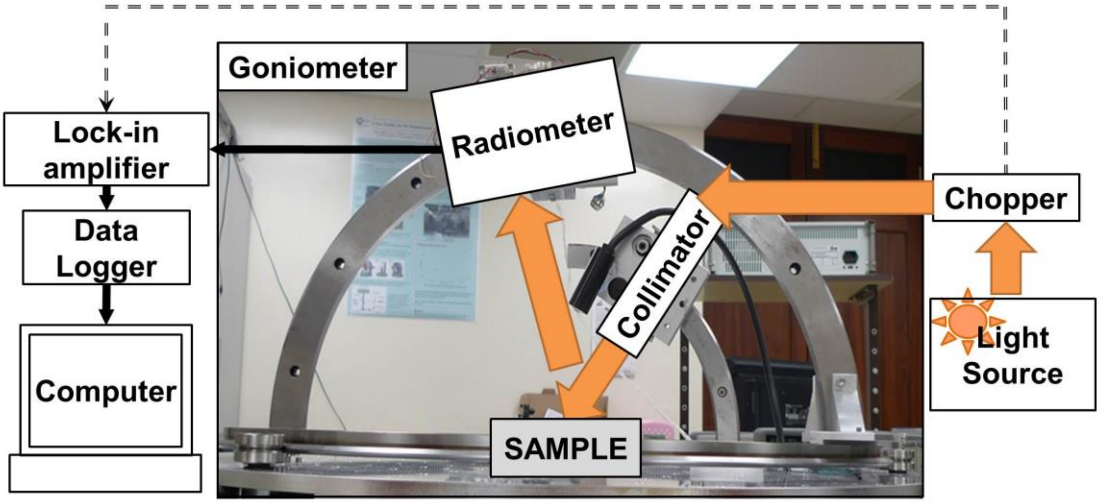

Figure 55: Block diagram of the OSEG setup on an optical bench ready to make BRDF measurements in the visible of a Spectralon sample.

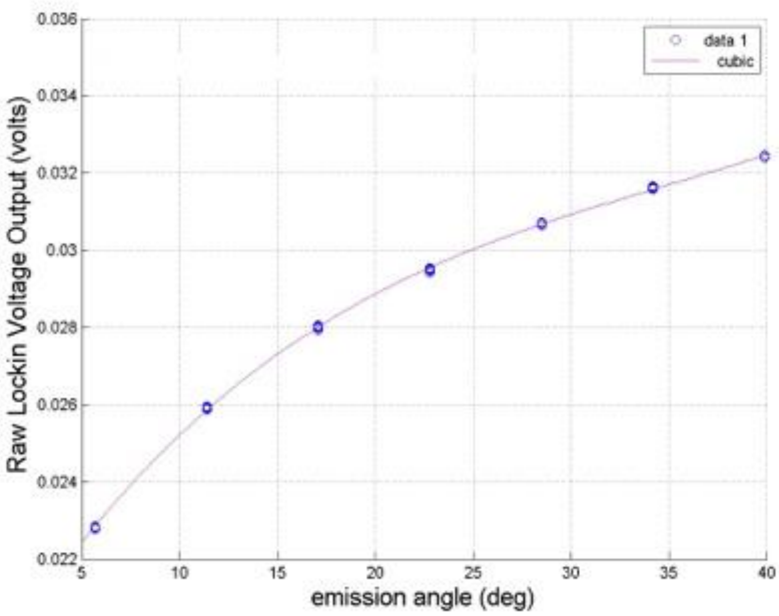

Figure 56: The output of the lock-in amplifier as recorded at seven different emission angles and fitted cubic spline (red). Using the interpolated average at each emission angle, the range of values observed at each angle, gives to a first order approximation the angular accuracy of the goniometer.

The average value recorded at each emission angle was then interpolated to give a function between the lock-in amplifier output and the emission angle (Figure 56). Using this interpolation the difference in the lock-in amplifier output at each emission angle was converted into an angular error. To a first order approximation this angular error equates to the angular accuracy of the emission angle in the goniometer setup. This procedure was then repeated to measure the accuracy of the phase angle movement. The emission and phase angular accuracy was found to be 0.03^{o} and 0.1^{o} respectively, 0.47^{o} and 0.4^{o} better than the angular accuracy laid out in the requirements for the goniometer in section 3. Table 12 compares the angular range, accuracy and resolution of the OSEG with the requirements (section 3).

Table 12: Comparing the angular resolution, accuracy and range of the OSEG to the requirements laid out in section 3. The angular resolution, accuracy and range for all the angles shown for the OSEG have been measured, except for the incident angle range which has been taken from the CAD model of the OSEG. The angular resolution was calculated by counting the number of stepper motor steps between $0^0 – 75^o$ emission angle and $0^o – 360^o$ phase angle.

	Requirement laid out in section 3	OSEG
Phase angular resolution	0.1^o	0.01^o
Emission angular resolution	0.1^o	0.003^o
Phase angular accuracy	0.5^o	0.1^o
Emission angular accuracy	0.5^o	0.03^o
Phase angle range	$0 – 360^o$	$0 – 360^o$
Emission angle range	$0 – 90^o$	$0 – 75^{o\,*}$
Incident angle range	$0 – 90^o$	$0 – 75^o$

4.4.8 Radiometer Signal to Noise Performance

The specific detectivity (D^*) is often used to characterise the performance of an infrared detector (Robinson 1993). For DE measurements in the thermal infrared, the radiometer will be a high performance pyroelectric detector (Infratec LIE-332F with D^* $10^9 cmHz^{1/2}W^{-1}$), with wavelength selection provided by spare Diviner filters. As stated in the requirements in section 3, the SNR of the goniometer must be at least 30. Based on this requirement, a D^* for the infrared detector element can be calculated using equation 34 with the parameters given in Table 13. In the requirements (section 3) it was shown that with the cold shield around the sample the emission from the sample will dominate over the reflection. As such, equation 34 assumes the only radiation source is infrared emission from the sample, which is modelled as a blackbody at 350 K (taken to be the lowest temperature the OSEG will measure at).

$$D^* = \frac{SNR\sqrt{A\Delta F}}{B_s A\Omega} \quad \textbf{34}$$

Where B_s is the radiance emitted from the sample (calculated from equation 35). A is the surface area of the detector element, Ω is the solid angle subtended by the baffle aperture as viewed from the detector (approximated for small angles by equation 36). ΔF is the inverse of the integration time and SNR is the signal to noise required.

$$B_s = \int B(\lambda, 350K)d\lambda \quad \textbf{35}$$

Where $B(\lambda, 350K)$ is given by the Planck function at a temperature of 350 K.

$$\Omega = 2\pi(1 - \cos(\theta)) \quad (36)$$

Where θ is the half angle between the baffle aperture and the detector.

Table 13: Goniometer, radiometer geometries and radiances used in calculating the required D^* for the infrared radiometer.

Quantity	Value	Notes
Distance between baffle and detector (mm)	65	See Table 11.
Diameter of baffle (mm)	2	See Table 11
Solid angle subtended by baffle in front of detector (sr)	7.43×10^{-4}	Calculated using equation 36
Diameter of infrared detector element (mm)	1	(InfraTec 2015)
Integration time (sec)	1	Assumed to be a sensible time to integrate for, but could be increased if a greater SNR is required.
Radiance emitted from the sample ($Wsr^{-1}m^{2}$)	6.45	Calculated integrating the Planck function for a hot blackbody at 350 K between the passband wavelengths (8.1 µm and 8.4 µm) for Diviners A4 filter
Required D^* ($cmHz^{1/2}/W$)	5.88×10^{8}	Calculated using equation 34

The required D^* was calculated assuming the A4 Diviner filter (8.1 – 8.4 µm) is used for wavelength selection. As stated in section 4.4.2, due to the roll off wavelength of the KBr window on the Infratec detector element only Diviner filters A3 – A6 are usable. The A4 Diviner filter was used for these calculations as it will provide the lowest amount of radiance (as it has the narrowest spectral transmission), i.e. the smallest signal, of all of the usable Diviner filters and therefore if the SNR is acceptable for the A4 filters it will be acceptable for all the usable Diviner filters. From the values in Table 13 the required D^* of the infrared detector is calculated as 3.5×10^8 $cmHz^{1/2}/W$ and the D^* given on the data sheet for the LIE-332F detector element is $10^9 cmHz^{1/2}/W$ (InfraTec 2015), three times greater. The SNR of the OSEG will therefore be acceptable.

4.4.9 Frequency stability

From the requirements the frequency stability of the chopper must be within ±0.05 Hz to ensure the systematic error introduced to the DE measurements is below 1%. When measuring the BRDF with the light source chopped on the optical bench, the chopper frequency (at 10 Hz) is very stable (±0.01 Hz). This is because the chopper is not moved; instead the chopped signal is feed down an optical fibre that is attached to the incidence carriage. However, for measuring the thermal infrared pure DE, no light source is used and the chopper is mounted on the radiometer carriage. Therefore the chopper is moved around the sample as the emission angle is changed. The chopper frequency can be read from the lock-in amplifier by communicating via RS232 with it. During the initial testing of DE measurements the stability of the chopper frequency was found to be outside the required level (±1 Hz). A proportional-integral-derivative (PID) control loop was therefore made to control the frequency of the chopper to within ±0.05 Hz as stated in the requirements (section 3.8). To ensure that the PID controller did not cause the frequency to oscillate when a measurement was made, the PID controller was turned off during a measurement.

4.5 Sample Changer

From the requirements the temperature of the sample must be controlled to ±0.25 K. A sample changer (Figure 57) that can hold up to four samples is placed in the centre of the base plate. For powdered samples a sample cup 50 mm in diameter and 3 mm deep has been designed. To meet the temperature stability requirement each sample has a platinum resistance thermometer (PRT) embedded inside to accurately monitor (±0.01 K) the temperature of the sample. A 50 W heater is placed on the back of each sample and a custom built PID controller (Appendix 3) is used to control the temperature of each sample to between 340 K and 490 K with the required accuracy of ±0.25 K.

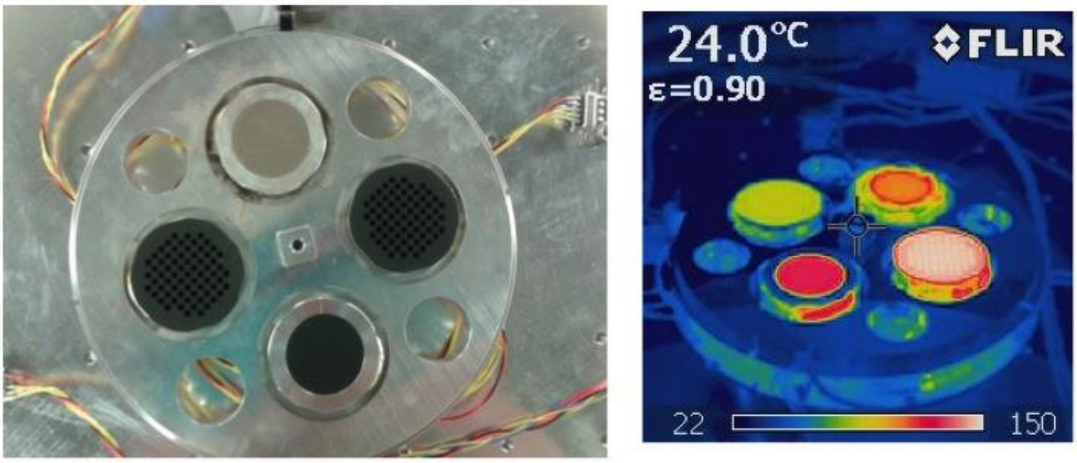

Figure 57: Sample changer in the visible on the left and in the thermal infrared on the right (taken using a FLIR IR camera). The thermal infrared image shows the same four samples shown in the visible image being controlled to four different temperatures.

4.6 Light Source for Future DE Measurements in the thermal infrared

Currently for measuring the thermal infrared DE of a sample with the OSEG, a sample is heated only from below, i.e. the light source has not been implemented in the current design. In the future the OSEG will be able to heat the sample from above using a light source. The light source must be uniform and illuminate the whole sample. As the goniometer will be under vacuum, cooling pipes will be required to cool the light source. Space for the cooling pipes has been incorporated into the design for the base plate and the light source assembly carriage (see future work, section 11).

4.6.1 Known Issue with Light Source Design

A consequence of the design required to address all the requirements for the goniometer (section 3) is that once implemented the light source will obstruct the radiometer’s view of the sample at low phase angles. This problem is illustrated in Figure 59, section 5.4 as observed when making BRDF measurements. Unfortunately, this will prevent the goniometer from observing the opposition surge, one of the primary features of the BRDF (section 1.5.1.2) and could be present in the DE of a powdered sample with low thermal conductivity. However, the measurements made will still be valuable as the literature review has shown there is no data on DE measurements for powdered samples in the thermal infrared and the current goniometer design will be able to measure most of the DE (<10^o phase angles will be obscured). Modifications can be made in later iterations of the goniometer to allow measurements at smaller phase angles. One potential solution would be to have a small secondary light source attached to the radiometer arm that would be used to measure the DE for small scattering angles. PHIRE-2 has been recently updated enabling it to record zero phase angle measurements. A 50:50 beam splitter is used on the light source arm, which allows reflected light from the surface being measured to reach the detector (Pommerol et al. 2011). BUG cannot measure zero phase angles, but can measure very small phase angles due to its large size (the arms on BUG are ~2 m long) (Johnson et al. 2013). However, the size of the OSEG must be small (<1 m) to fit inside a vacuum chamber.

4.7 Build Summary and Comparison with Requirements

The OSEG has been constructed and shown to have:

- A mechanical angular accuracy of 0.1^o compared to the 0.5^o accuracy in the requirements. However, the angular accuracy of the OSEG design will be limited by the divergence of the input beam to the radiometer – 0.4^o.
- An angular range of 0 – 75^o in emission angle and 0 – 360^o in phase angle. Compared to 0 – 90^o and 0 – 360^o outlined in the requirements.
- A required D^* performance from the SNR outlined in the requirements (section 3) that is equivalent to the D^* performance of the selected detector element.
- As required the whole setup is surrounded by a high emissivity (>0.95) cold shield <150 K and inside a vacuum chamber <10^{-6}mbar, to simulate a space environment.
- The cold shield is almost isothermal with a 2.1 ±1K temperature gradient, compared to <10 K outlined in the requirement.
- The temperature stability of the radiometer instrument is ±0.15 K, which is better than outline in the requirements ±0.25 K.

- The temperature stability of the sample is as outlined in the requirement ±0.25 K.
- The projected FOV of the radiometer instrument has been shown to be uniform circle at an emission angle of 0^o.
- Frequency stability of ±0.05 Hz meeting the required 0.05 Hz frequency stability.
- No light source arm currently implemented for use in measuring the DE.

Table 14: Summary of the comparison between the requirements (section 3) and the performance of the OSEG.

	Requirement	OSEG
Phase angle	0-360^o	0-360^o
Emission angle	0-90^o	0-75^o
Incidence angle	0-90^o	Not implement
Angular Accuracy	0.5^o	<0.37^o
Cold Shield	<150 K	<150 K
Pressure	10^{-6} mbar	10^{-6} mbar
SNR	30	>30 (depending on integration time)
Temperature stability of Radiometer Instrument	±0.25 K	±0.15 K
Temperature stability of Sample	±0.25 K	±0.25 K
FOV	Uniform circle smaller than the sample size	7.7 mm diameter circle (sample size 50 mm)
Frequency stability	±0.05 Hz	± 0.05 Hz

5 Validation of the OSEG Setup

This section outlines the work done to validate the OSEG setup by making measurements of targets with known phase functions. As most previous scattering studies have measured the BRDF in the visible, the OSEG was setup to make BRDF measurements in the visible, before making thermal infrared DE measurements. This allowed BRDF measurements of the reference target Spectralon (described in section 5.1) to made and compared to previous studies. To further validate the OSEG setup, a NIR LED was measured and compared to the value given on its datasheet (described in section 5.7).

5.1 Validation in the Visible Measuring the BRDF of Spectralon

Spectralon is a commercially available reference target in the visible. It has been measured by a number of goniometers (including the PHIRE and BUG setups described in section 1.5.4.4) before and hence has a well-studied and defined BRDF. Spectralon is often used as a reference target as it is a material that ideally exhibits near perfect lambertian scattering (i.e. equal in all directions) across all wavelength ranges in the visible and near infrared. The OSEG was constructed on an optical bench and the BRDF of a calibrated Spectralon target under atmospheric pressure in the visible was measured.

5.2 Modifications to the OSEG Setup for Measuring in the Visible

To measure the BRDF of Spectralon in the visible the OSEG was setup as described in section 4 with modifications to the light source and radiometer described in the following two subsections (5.2.1 – 5.2.2). An overview block diagram of the OSEG setup used to measure the Spectralon target is shown in Figure 55 (see section 4.4.7).

5.2.1 Light Source for BRDF Measurements in the Visible

For BRDF measurements in the visible, a 45 W quartz halogen bulb and back reflector was used to provide a uniform and collimated light source. The light source was chopped and focused down an optical fibre light guide. The output beam from the optical fibre was collimated onto the sample using a collimating lens. It was later found that the uniformity and collimation of this light source was not good enough for accurately measuring the BRDF of samples. The light source was changed to a 4.5 mW green laser to provide a uniform and highly collimated light source with a well-defined spot size on the sample (see section 5.5).

5.2.2 Radiometer for BRDF Measurements in the Visible

To measure the BRDF of Spectralon in the visible the radiometer carriage was modified by removing the thermal infrared pyroelectric detector and using a silicon photodiode detector (RS stock number 303-719). A trans-impedance (Appendix 2) amplifier was used to increase the signal strength from the photodiode before connecting it into the lock-in amplifier. As the light source is chopped the chopper was removed from the radiometer carriage.

5.3 Calibration of PHIRE using Spectralon

To compare the PHIRE and OSEG results it is first necessary to understand how PHIRE calibrate and report their BRDF data. The PHIRE goniometer has taken measurements of the BRDF of Spectralon (Figure 58). All measurements made by PHIRE are calibrated by assuming that the BRDF of Spectralon is equal to 0.99 (its hemispherical albedo) at an incidence angle of 0^o and an emission angle of 55^o over the entire visible and near-infrared (0.4 – 2.5 μm) spectral range (Labsphere 2012). All reflectance measurements performed using PHIRE are then calibrated relative to this single reference measurement.

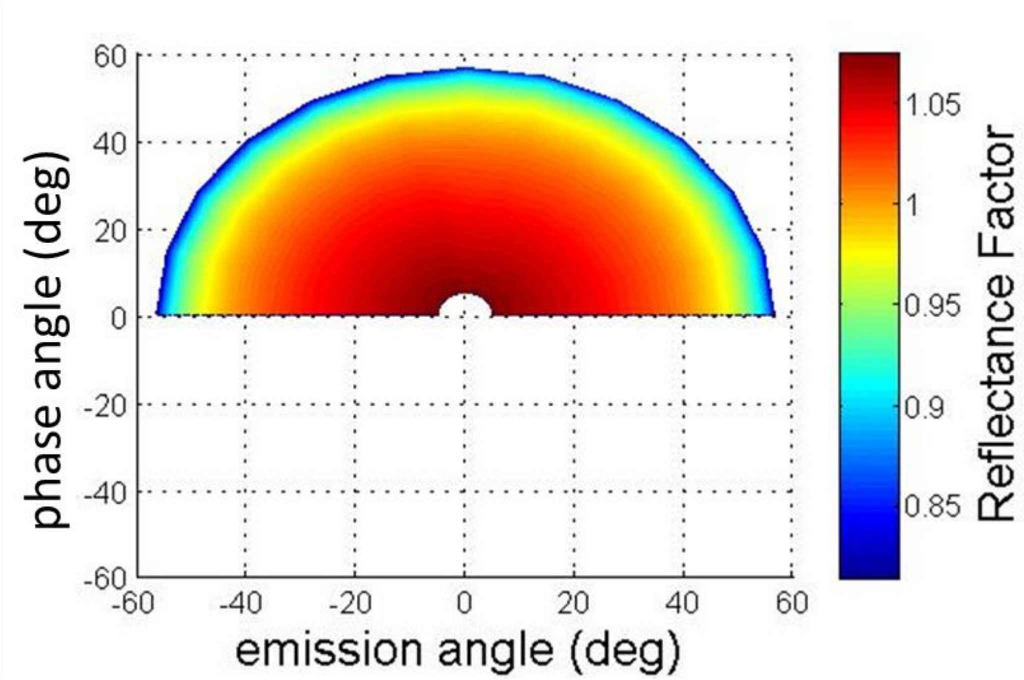

Figure 58: Measured reflectance factor of Spectralon by PHIRE at 650nm. After Pommerol et al. (2011)**. Generally PHIRE measurements are reported in reflectance factor. Reflectance factor is defined in equation 39 as π times the ratio of the BRDF to the cosine of the incidence angle. The reflectance factor of an isotropic emitter would be equal to 1 and independent of both emission and incidence angles.**

The PHIRE instruments have a modulated light source (25 Hz) that provides a small (between 2 mm – 2 cm) well defined spot size on the sample. The diameter of the sample holder is 16 cm. At an emission angle of 0^o the FOV of the radiometer is the entire surface of the sample. When the emission angle increases, the FOV becomes ellipsoidal, with the length of the semi-major axis proportional to the cosine of the emission angle. Areas outside the sample are therefore in the FOV, but do not contribute to the signal, as they are not illuminated by the modulated light source. The general optical layout chosen for the PHIRE instruments (small incident beam and large detector FOV) therefore implies a division by the cosine of the emission angle to retrieve the BRDF (equation 37) or reflectance factor values (equation 39) from the raw voltage V:

$$r(\theta_e, \theta_p, \theta_i) = C_\lambda V \frac{cos(\theta_i)}{\cos(\theta_e)} \quad \textbf{37}$$

Where C_λ is a wavelength dependent calibration constant defined in equation 38, V is the raw voltage, θ_i and θ_e are the incidence and emission angles defined in Figure 20.

$$C_\lambda = \frac{0.99\cos(55^o)}{\pi V_{Sp,55^o}} \quad \textbf{38}$$

Where $V_{Sp,55^o}$ is the raw voltage at 55^o emission angle and 0^o incidence angle.

$$\bar{R} = \pi \frac{r(\theta_e, \theta_p, \theta_i)}{\cos(\theta_i)} \quad \textbf{39}$$

Where $\bar{R}$ is the reflectance factor and θ_i is the incidence angle (Figure 20).

PHIRE calculates both BRDF and reflectance factors values from the raw voltage measurements, according to standard definitions used in equations 37 and 39. According to these formulae, the BRDF of an ideal lambertian target would be equal to $\frac{1}{\pi\cos(\theta_i)}$ and the reflectance factor of the same target would be equal to 1 independent of both emission and incidence angles. The reflectance factor values give a more intuitive representation of the photometric behaviour of a surface, and will therefore be referred to in the remainder of this thesis. Figure 58 shows the photometric measurements acquired with the PHIRE-2 goniometer of the reference surface Spectralon. The surface has been interpolated from reflectance measurements made in steps of 5^o in emission angle (from 0^o to 80^o), in steps of 15^o in phase angle (from 0^o to 165^o) and at an incidence angle of 0^o. As can be seen Spectralon does not exhibit perfect lambertian scattering, its reflectance factor increases with decreasing emission angle. However, at an incidence angle of 0^o and for a particular emission angle, the reflectance factor of Spectralon is constant for all phase angles.

5.4 Validation and Calibration of the OSEG using Spectralon and Comparison with PHIRE

The OSEG setup was used to measure the reflectance factor of Spectralon using a quartz halogen light bulb as the light source. A Matlab script was written to acquire measurements in steps of 5.7^o emission, 12^o phase and 0^o incidence angle. Some angles were not recorded (only emission angles between 20^o and 70^o were recorded and 0^o phase angle was not recorded) as the light source arm obscured the radiometers view (section 7.5). The time constant on the lock-in amplifier was set to one second with a pause of thirty seconds after the radiometer carriage had moved into position to allow the lock-in output to settle. The reflectance factor of Spectralon measured by the OSEG (Figure 59) was normalised in the same way as PHIRE (equations 37 and 39), by assuming that at an emission angle of 55^{o} and an incidence angle of 0^{o}, the reflectance factor of Spectralon is equal to 0.99.

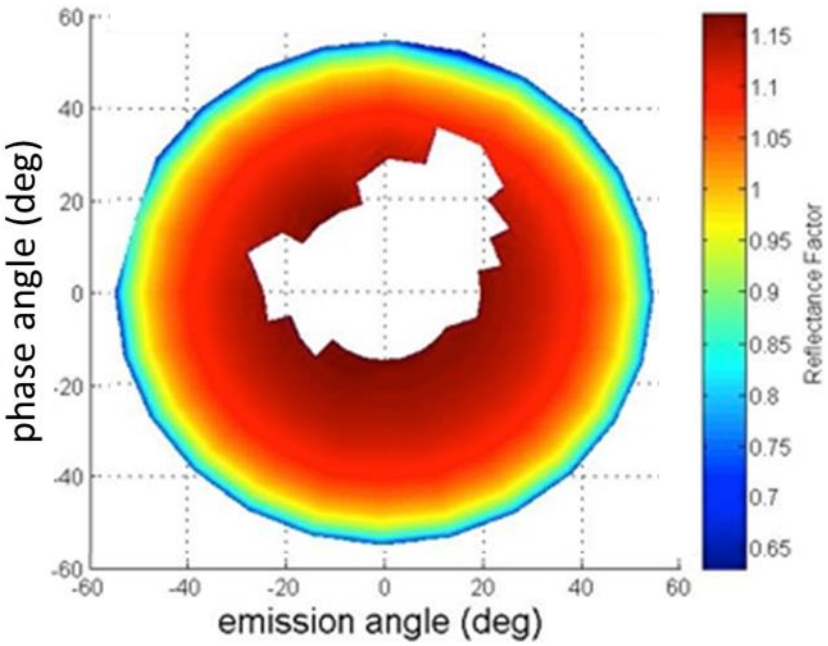

Figure 59: Reflectance factor of Spectralon measured by OSEG with a well defined detector FOV and a large light source spot size. The surface has been interpolated from reflectance measurements made in steps of 5.7^{o} in emission angle (from 20^{o} to 70^{o}), in steps of 12^{o} in phase angle (from 0^{o} to 180^{o}) and at an incidence angle of 0^{o}

Qualitatively the results show a similar function (the reflectance factor decreases with emission angle) to that observed by PHIRE, but there are major quantitative differences between the two different measured reflectance factors (Figure 61). The reflectance factor measured by OSEG falls faster with emission angle than the PHIRE measurement (Figure 61). The difference between the two was believed to be because the light source used in the OSEG setup was not uniform (see following section 5.5). PHIRE measures the reflectance factor in a fundamentally different way to the OSEG setup, by having a well-defined spot size on the sample and a poorly defined, large detector FOV (see section 5.3). This setup means the non-uniformity of the light source is reduced in the data.

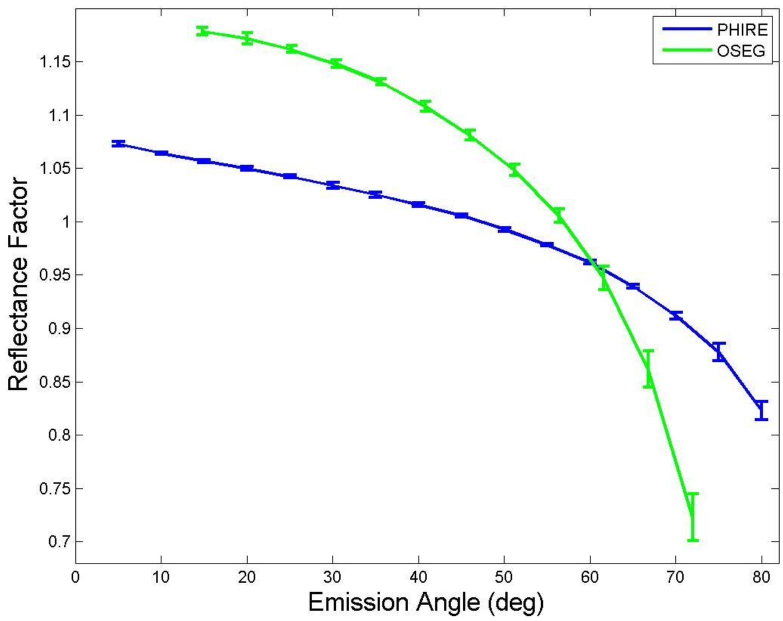

Figure 60: Comparison between OSEG and PHIRE measurements of Spectralon.

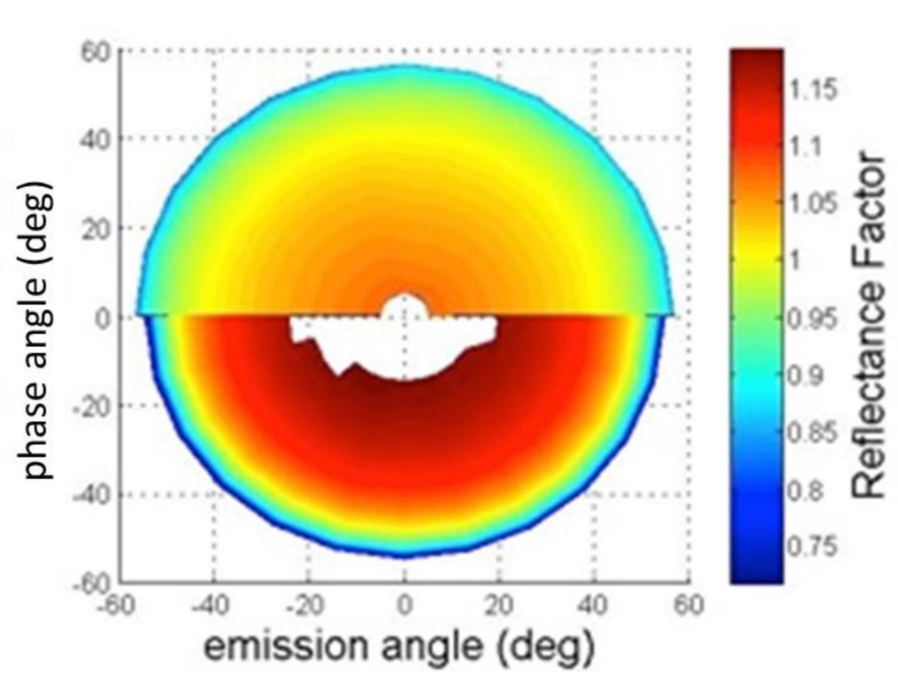

Figure 61: Comparison between the reflectance factors of Spectralon measured by PHIRE and SEG. Right top hemisphere is Spectralon measured by PHIRE and the bottom is measured by OSEG.

5.5 Light Source Uniformity

The uniformity of the OSEG light source was measured by placing a small 2 mm diameter baffle over a digital light meter (ISO-TECH ILM 1335) in the centre of the light source beam (Figure 62). The light meter and baffle were moved across the beam and the output of the meter was recorded every 0.5 mm. The results are shown in Figure 63. This measurement is not a direct function of the light source uniformity as the measurement setup has a spatial response that is convolved with the light source uniformity. However, this measurement does show that the light source is not uniform (±4 LUX). The non-uniformity of the light source would affect the reflectance factor values measured by OSEG and could explain the difference between the measured values of Spectralon by PHIRE and OSEG shown in Figure 61.

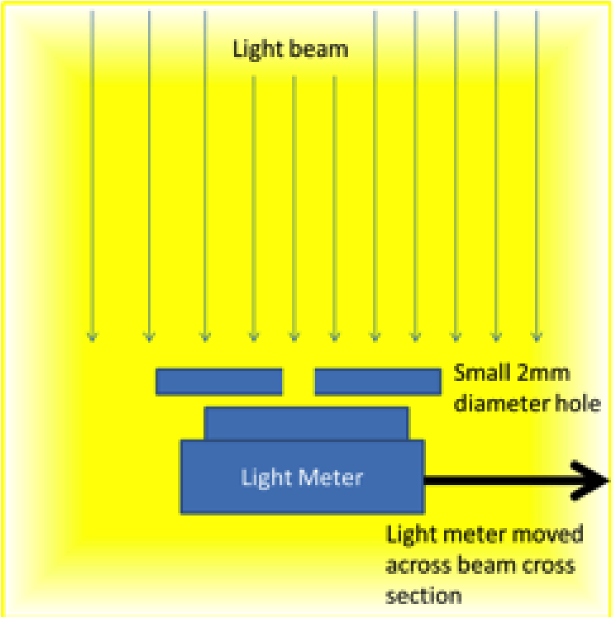

Figure 62: Setup used to measure the uniformity of the light source beam.

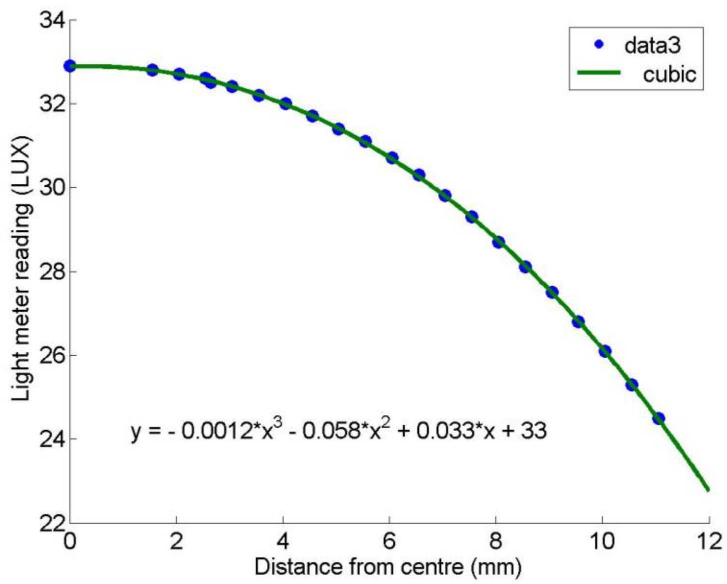

Figure 63: The measured light intensity from the centre of the light source beam, showing that the light source is non-uniform.

5.6 Using a Green Laser (532 nm) as an Improved Uniform Light Source

To reduce the effect of the light source non-uniformity on the measured reflectance factor of Spectralon, the OSEG setup was changed to a similar setup to PHIRE. The light source was replaced with a green laser (523 nm) to provide a well-defined small (10 mm) spot size on the sample (Figure 64). The green laser was setup on the optical bench and chopped before being coupled down an optical fibre. At the other end of the optical fibre the light source was collimated using a collimator lens onto the sample giving a working spot size on the Spectralon surface of ~10 mm. The incidence angle was set to be zero degrees. On the radiometer, the baffle in front of the collecting mirror was removed to enlarge the detectors FOV. The detector's FOV is larger than the target sample, but as the lock-in was used only chopped light will was detected after demodulation by the lock-in amplifier. Using this setup the BRDF and reflectance factor values for Spectralon can then be calculated from equations 37 and 39.

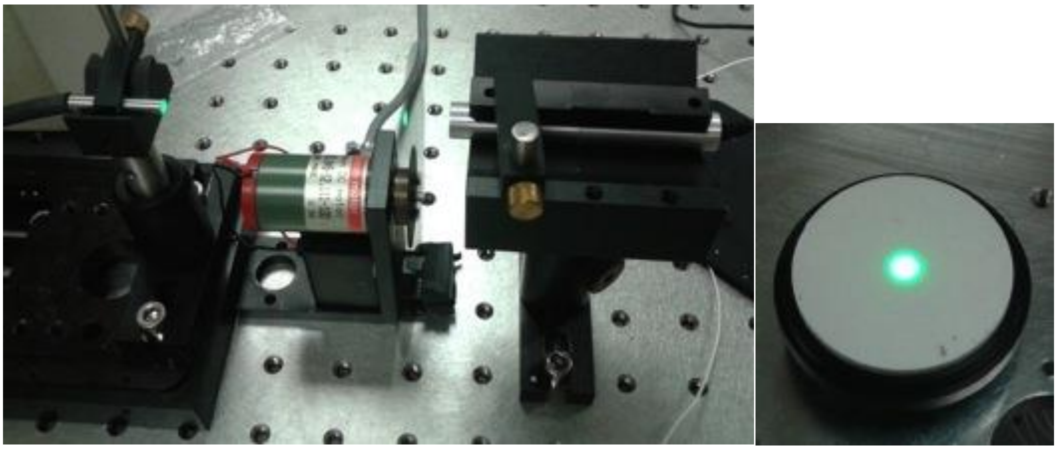

Figure 64: (Left) The green laser setup on the optical bench, chopped before being coupled down an optical fibre. This setup replaces the optics shown in Figure 54. **(Right) Photograph of the spot placed on the Spectralon by the green laser.**

Using the new light source and radiometer setup, the reflectance factor of Spectralon was measured again. The same Matlab script was used to acquire measurements in steps of 5.7^{o} emission, 12^{o} phase and 0^{o} incidence angle. The same time constant and settling time were used as before (one second time constant and thirty seconds settling time). Measurements with this setup showed that the goniometer setup is very sensitive to the tilt of the sample. Unfortunately, due to the plastic container of the Spectralon, it was difficult to get the surface of the Spectralon aligned with the frame of the goniometer. However, it was possible to correct for sample tilt using a method for removing the tilt of the sample from the measured data used by the PHIRE goniometer (Pommerol et al. 2011). A comparison between the measured reflectance factor of Spectralon (with the surface tilt removed) by PHIRE and the OSEG is displayed in Figure 65. Measurements made by the OSEG are very close to measurements made by PHIRE (R^2 of 0.95). The similarities between these two measurements validate the OSEG setup and shows it can make BRDF measurements with a comparable accuracy to PHIRE. The slight differences in the two measured values could be explained by small differences in the Spectralon targets used or be due to the different wavelengths used (the OSEG measurement was made at 523 nm and PHIRE was made at 650 nm).

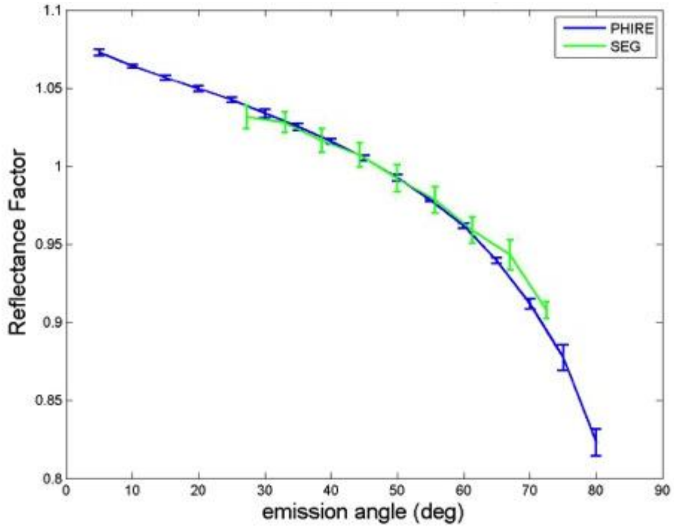

Figure 65: Comparison between measured reflectance factor values of Spectralon by OSEG and PHIRE. The sample tilt has been removed from both sets of measurements using the method described in (Pommerol et al. 2011). The error bars represent the standard deviation of all the measured reflectance factor values at a particular emission angle, but at different phase angles.

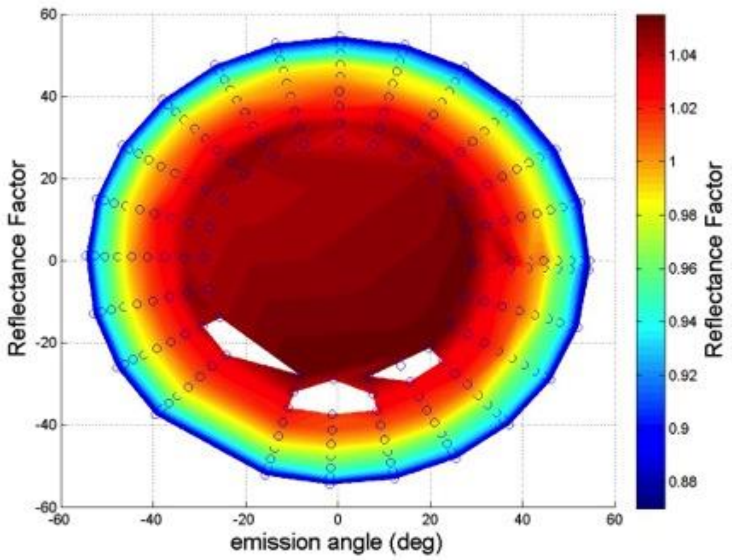

Figure 66: Reflectance factor of Spectralon measured by OSEG with a large detector FOV (>20 mm at 0^{o} emission angle) and a well-defined light source spot size ~10 mm. The surface has been interpolated from reflectance measurements made in steps of 5.7^{o} in emission angle (from 20^{o} to 70^{o}), in steps of 12^{o} in phase angle (from 0^{o} to 180^{o}) and at an incidence angle of 0^{o}. Each circle represents where a measurement point was made.

5.7 Testing the OSEG in the NIR with Throw Cone Measurements of NIR LED

Once the OSEG setup had been validate in the visible, it was tested in the near infrared (NIR) by measuring the normalised angular intensity of a NIR LED (L10660-01) and comparing to the datasheet values. The NIR LED chosen was L10660-01 (Hamamatsu Photonics 2010) with a peak emission at 1.45 μm. The sample changer was removed and a special mount was made to hold the LED in the centre of the goniometer. At 0^o emission angle the intensity of the LED was defined to be 100% and the angular intensity of the LED was then calculated using equation 40.

$$I(\theta_e, \theta_p) = \frac{V(\theta_e, \theta_p)}{V(0^o, 0^o)} \qquad \textbf{40}$$

Where I is the angular intensity of the LED output, V is the raw voltage recorded by the lock-in amplifier, θ_e and θ_p are the emission and phase angles defined in Figure 21.

The baffle and chopper were placed back on the radiometer carriage and the photodiode was replaced with the thermal infrared pyroelectric detector (LIE-332F-66). The same Matlab script used to measure the Spectralon target was run, to acquire measurements in steps of 5.7^o emission and 12^o phase angle. The lock-in amplifier was set to one second time constant and a settling time of 30 seconds was waited before recording the lock-in voltage. The measured normalised angular intensity of the NIR LED agrees within error to that stated on its data sheet (Figure 67 and Figure 68).

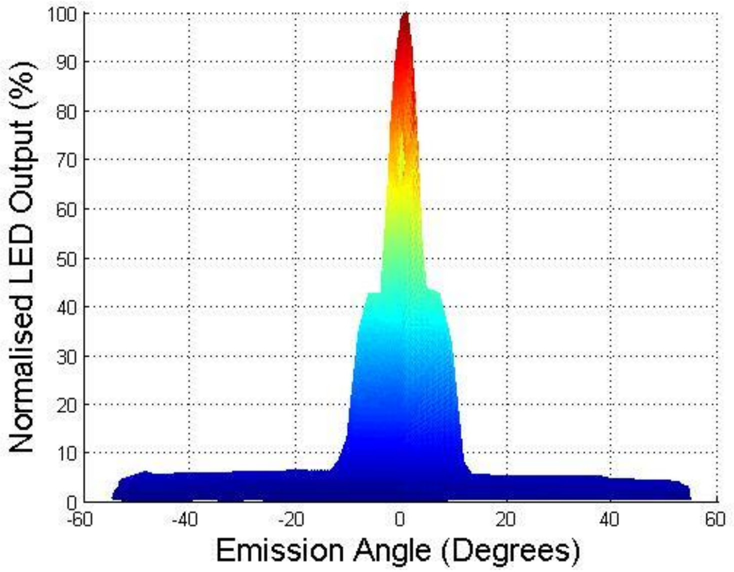

Figure 67: OSEG measured normalised angular intensity distribution of near infrared LED (L10660-01). The intensity distribution was interpolated from measurements made in steps of 5.7^o in emission angle (from 0^o to 72^o), in steps of 12^o phase angle (from 0^o to 360^o).

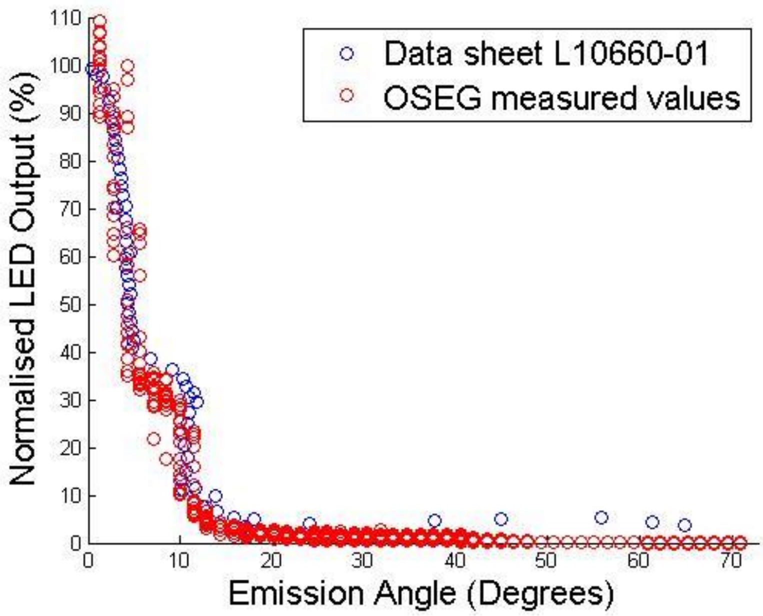

Figure 68: Comparison between the normalised angular intensity of NIR LED (L10660-01) given on data sheet (blue) and measured by OSEG (red).

5.8 Summary of Validation Work

The OSEG has made measurements of two targets with well-characterised phase functions. In the visible the reflectance factor (similar to the BRDF) of Spectralon compared well (R^2 of 0.95) with previous measurements made using the PHIRE goniometer. The PHIRE goniometer has validated its setup against Spectralon measurements from the BUG goniometer. Therefore the OSEG setup also compares well with the BUG setup. In the near infrared, angular intensity measurements of a NIR LED compared well (see Figure 68) to the values given on its datasheet. These measurements have been taken to show the validity of the OSEG setup and in the next section the OSEG is used to measure the DE of surfaces of varying roughness.

6 Infrared DE Measurements of 'Simple' Surfaces.

After completing the design, testing and validation of the OSEG, the DE measurements of solid and particulate samples were made.

6.1 Flat (micron scale roughness) Surface Nextel target.

A spray painted Nextel (Nextel paint manufactured by Mankiewicz Gebr & Co) aluminium target (Figure 69) was the first DE measurement of a surface made by the OSEG. The target was chosen as its DE has previously been characterised (Lohrengel 1987; Koirala 2004; De Silva & Jones 1987).

Figure 69: Nextel black painted aluminium target 50 mm in diameter.

6.1.1 Nextel Velvet coated aluminium target details.

The Nextel target was constructed by covering the surface of an aluminium plate with a thickness 5 mm and 50 mm in diameter with four layers of Nextel–Velvet-Coating 811-21. CSY Finishes (a professional spray painting company) applied the paint using a spray pistol to produce an almost uniform thickness over the surface. Unfortunately no data is currently available about the total thickness of the paint.

6.1.2 Surface Temperature Variation across the Nextel Painted Surface.

To make accurate DE measurements of the surface it is important there is no large (>1 K) temperature variation across the surface of the Nextel target. If there was a large temperature variation across the surface, then the assumption that the surface was a uniform temperature would be invalid and as the emission angle and FOV increases more regions of different temperatures would be observed causing the emissivity of the surface to appear to change.

To quantify this temperature variation a single thermal infrared image was taken using a FLIR thermal-IR camera (Figure 70). A 1D cross section of the image was then analysed (Figure 71) to show a small systematic increase in temperature from the edge of the target to the middle of the target of approximately 0.2^{o}. The image was taken approximately 2.5 cm above the target and therefore if the DE of the Nextel black paint is anisotropic and decreases with emission angle then the observed temperature of the target would drop towards the edge of the target. Therefore a better method for quantifying the surface temperature variation was devised, where eleven images were taken by a FLIR thermal-IR camera scanned across the Nextel surface controlled to a temperature of 100^{o}C. Starting at the edge of the target the camera was scanned across the surface in steps of approximately 5 mm. For each step the average central temperature inside the cross hair (see Figure 70) of the image was recorded. The scanned images (Figure 71) reveal that there was no systematic temperature variation across the surface and the surface temperature is uniform to 0.5^{o}C.

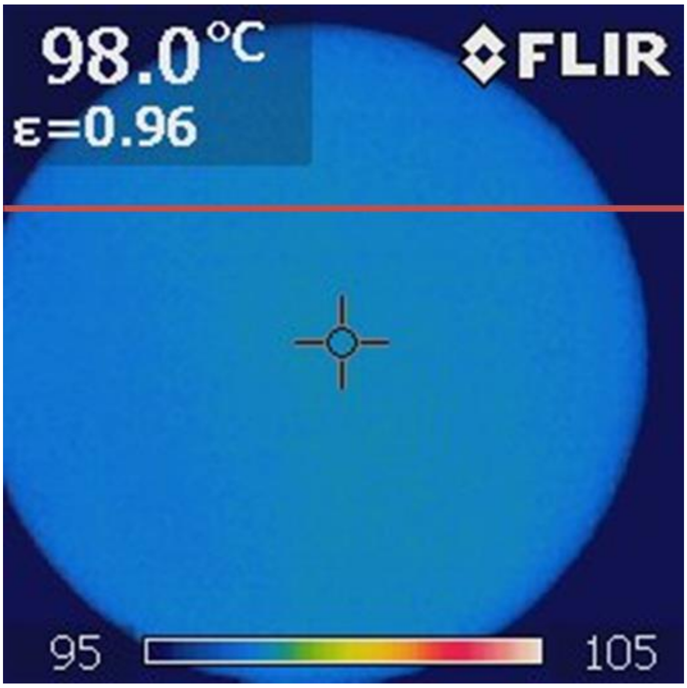

Figure 70: FLIR thermal image of the Nextel painted aluminium target. No large (>1 K) variation in surface temperature across the target is observed. The line shows where a one dimensional cross section was analysed in Figure 71.

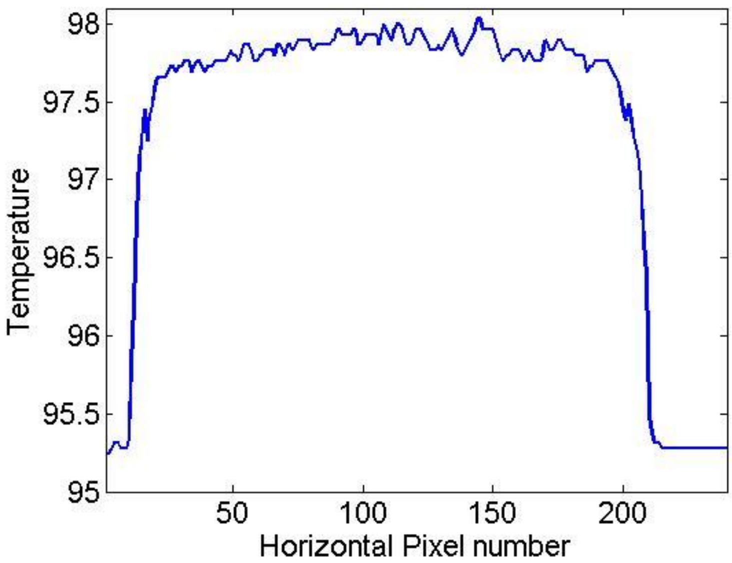

Figure 71: One dimensional cross section through the image shown in Figure 70. Showing the average surface temperature of the target is 97.8°C and there is a small increase in temperature near the middle of the target of approximately 0.2°C.

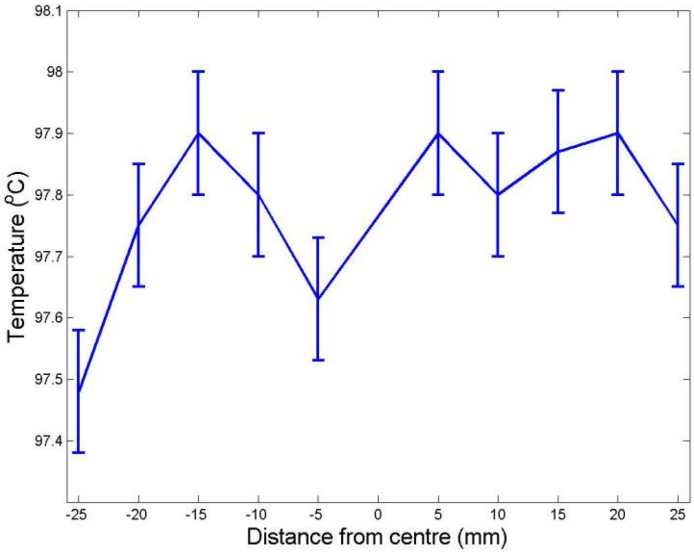

Figure 72: Scanning across the target with the FLIR camera shows the surface temperature of the target is uniform to within 0.4°C. The error bars are taken from the noise equivalent temperature difference (NETD) of the FLIR thermal IR camera (FLIR-Systems 2012)

6.1.3 Details of the DE Measurement of a Nextel Velvet Black Painted Target.

The OSEG setup used to measure the DE of the Nextel target is summarised in Table 15. Wavelength selection for these initial DE measurements was provided by the broadband KBr (0.2 – 25 µm, Figure 49) window on the front of the detector can. The sample was then heated from below and the cold shield was placed around the experiment, but was not switched on. Measurements were made at both atmospheric pressure (1 bar) and under vacuum at 10^{-6} mbar.

For each measurement a Matlab script was used to control the goniometer to take measurements in emission angle steps of 1.5^o. The radiometer carriage started at an emission angle of 0^o moving down to an emission angle of 72^o. At each 1.5^o step 30 seconds were waited to allow the lock-in amplifier to settle, then ten readings were made with five second pauses between each reading. Once an emission angle of 72^o was reached the radiometer carriage was moved back to 0^o again in steps of 1.5^o. For each measurement run at a particular phase angle this created a data set with 20 readings at each emission angle step. A total of 25 measurements runs were made at five different phase angles between 0 – 360^o and at target temperatures between 340 – 420 K. 20 measurement runs were completed under atmospheric pressure and five under vacuum.

Table 15: Summary of the OSEG setup used to measure DE of Nextel black paint

Parameter	Value
Pressure	Atmospheric (1 bar) - 10^{-6} mbar
Cold Shield Temperature	Ambient (~20^{o}C)
Wavelength Selection	0.2 – 25 μm (KBr window)
Target temperature	50-150^{o}C
Chopping Frequency	10 Hz
Settling time	30 s
Lock-in time constant	1 s
Emission angle range	0-72^o
Emission angle steps	1.5^o

6.1.4 Details of the DE Measurement Calibration

According to the definition of directional emissivity (DE) (equation 3, section 1.4.2), the radiation emitted by the sample is compared to that emitted by an ideal blackbody, under the same conditions. However, with the OSEG setup it is sufficient to compare the emitted radiation at each emission angle to the radiation emitted from the Nextel disk at 0^o emission angle. At an emission angle of 0^o, the emissivity of Nextel is assumed to be equal to 0.968,its average emissivity over the entire transmission spectral range of KBr (0.2 – 25 μm, Figure 73).

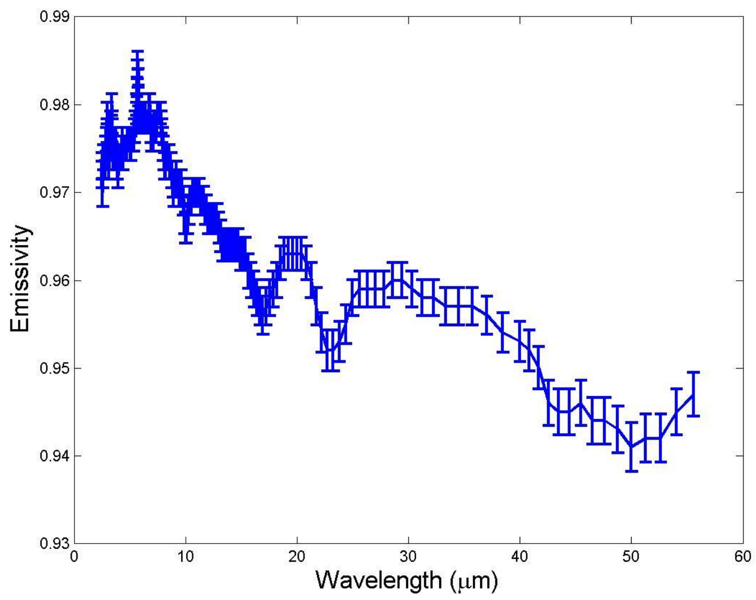

Figure 73: The total emissivity of Nextel 81-211 velvet black paint as measured by the National Physics Laboratory (NPL). After (Clarke 1997).

Using 0.968 as the normal emissivity of Nextel (emission angle of zero) the DE can then be calculated as:

$$\varepsilon_d(\theta_e, T) = 0.968\frac{V(0^o, T)}{V(\theta_e, T)} \quad \mathbf{41}$$

Where $\varepsilon_d(\theta_e, T)$ is the DE, $V(\theta_e, T)$ is the recorded raw lock-in voltage, $V(0^o, T)$ is the raw lock-in voltage recorded at 0^o emission angle. By this equation an isotropic surface emitter will have a DE of 0.968 for all emission angles.

6.1.5 Nextel Paint Emissivity Dependence with Surface Temperature

As the DE measurements made by the OSG are calibrated assuming the normal emissivity of Nextel paint is 0.968, it is important that the normal emissivity does not change over the surface temperatures measured in the OSEG. The normal emissivity of Nextel has been shown to change depending on the temperature of the Nextel paint (Figure 74). At temperatures below 150 K the emissivity decreases with temperature. However, between temperatures of 150 – 340 K the emissivity is very stable at 0.968 ±0.01. Therefore over the temperature range that the DE measurements have been made the normal emissivity of Nextel is expected to be very stable at 0.968 ±0.01.

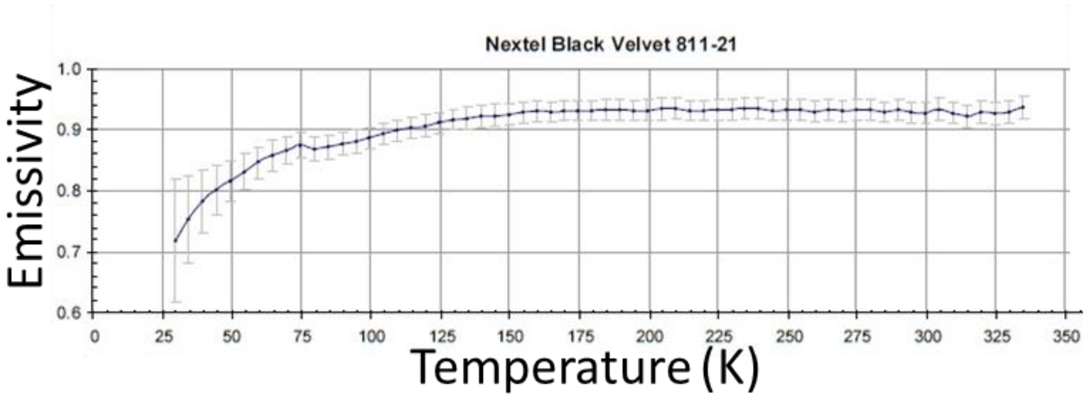

Figure 74: Changes in the broadband (0.2 – 25 μm) emissivity of Nextel with surface temperature. Taken from (Kauder 2005).

6.1.6 DE Measurements of Nextel

The measured broadband DE of Nextel-Velvet-Coating 811-21 is plotted in Figure 75 and compared to an isotropic emitter. It is clear from the measurement that Nextel is not an isotropic emitter. At emission angles greater than 40^o the emissivity of Nextel diverges significantly (Δ0.01 at 40^o and Δ0.08 at 70^o) from the expected emissivity of an isotropic emitter.

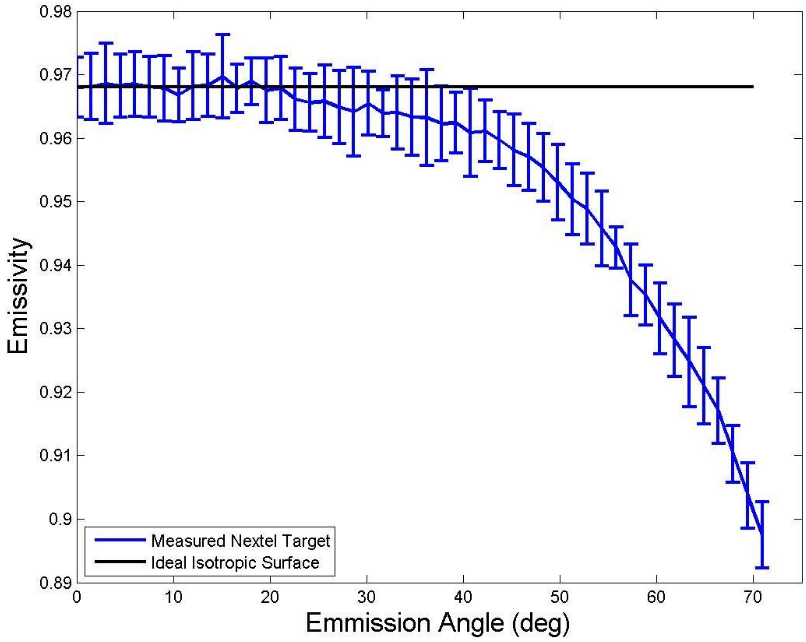

Figure 75: DE Measurement of Nextel 811-21 paint (blue). Measurements were made in 1.5^o steps of emission angle and at multiple phase angles between 0 – 360^o. At each emission angle step 20 measurements were taken, the error bars represent the standard deviation of measurements made at each emission angle. The DE of an ideal isotropic surface is shown for reference (black).

6.1.7 Measured Nextel Paint DE Dependence on Pressure

To investigate the effect of the surrounding pressure, the DE measurements of Nextel paint under ambient pressure and under vacuum (10^{-6} mbar) were made (Figure 76). Theoretically the surrounding pressure should not affect the DE of Nextel paint and from these measurements it is clear that the surrounding pressure does not have an effect on the DE. This gives confidence in the OSEG measurement setup.

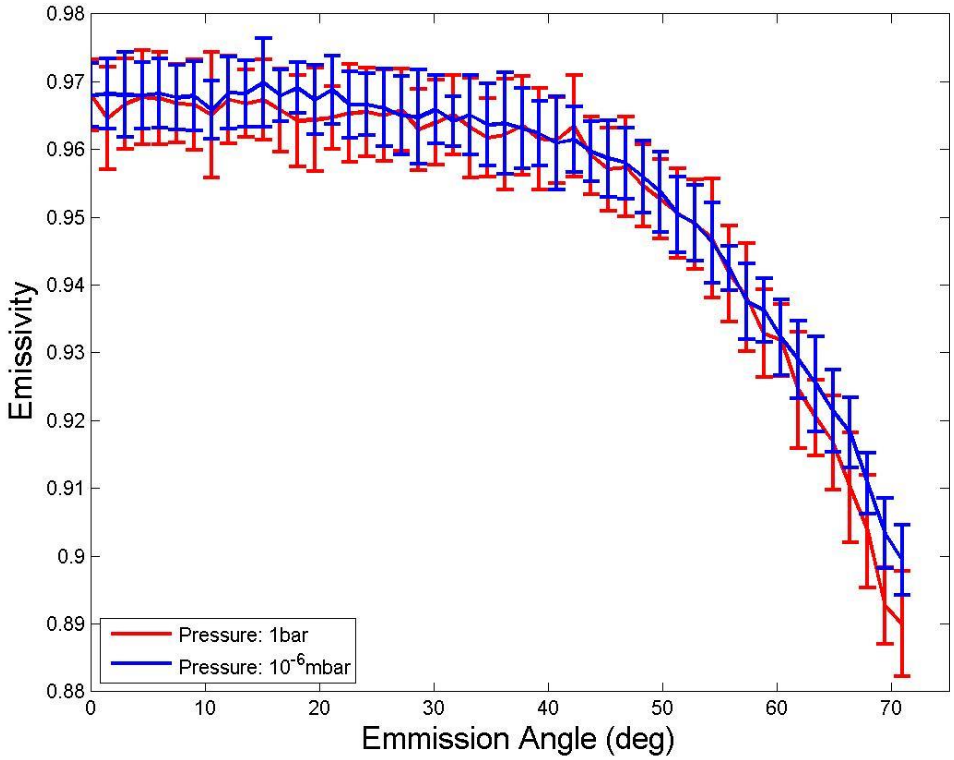

Figure 76: Two DE measurements of Nextel black paint under atmospheric (1 bar) pressure (red) and under (10^{-6} mbar) vacuum (blue).

6.1.8 Measured Nextel Paint DE Dependence on Sample Temperature

DE measurements of Nextel paint made by the OSEG also show no dependence with sample temperature within the measured sample temperature range (343 – 383 K) (Figure 77).

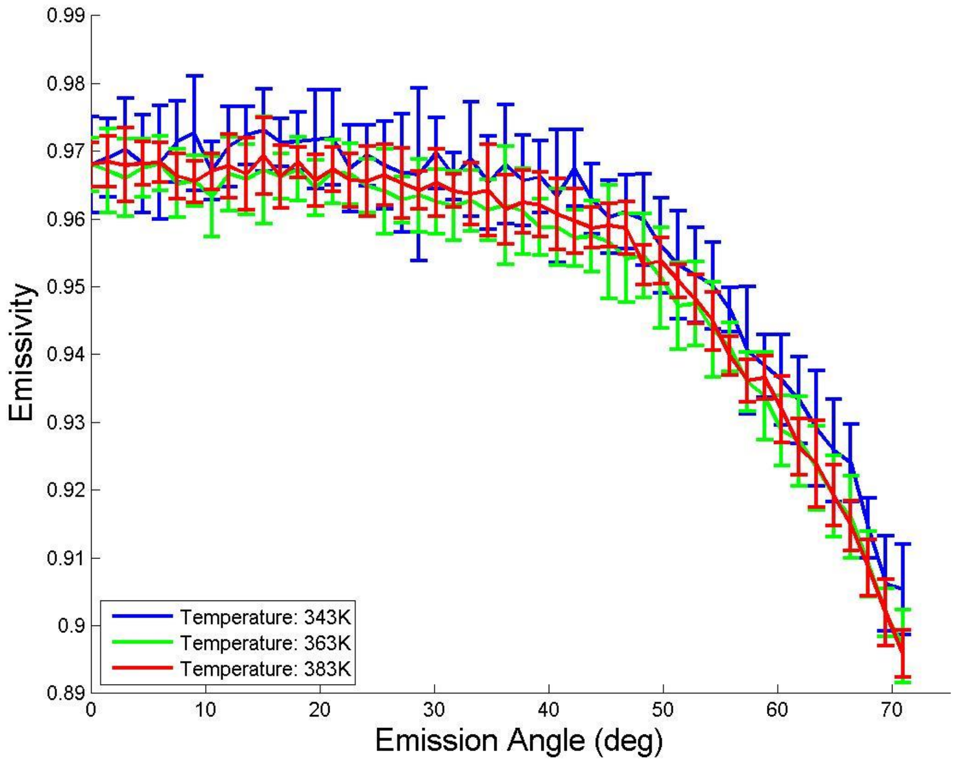

Figure 77: Three DE measurements of Nextel black paint under (10^{-6} mbar) vacuum pressure at 343 K (blue), 363 K (green) and 383 K (red).

6.1.9 Comparison of DE Measurements of Nextel Black Paint with Previous Studies

As stated before three previous measurements of the DE of Nextel painted targets have been made with three different goniometer systems similar to the OSEG setup (Lohrengel 1987; Koirala 2004; De Silva & Jones 1987). The three measurements are compared to the OSEG measurement in Figure 78. All four measurements agree within error between 0 – 50^o emission angles. However at emission angles greater than 50^o, there is some variation between the measurements and at 70^o there is a difference in emissivity of 0.04 between the measurements. The measurement made by De Silva & Jones (1987) agrees best with the OSEG measurement (R^2 >0.99, Figure 78). The variation between measurements at high emission angles could be due to slight differences in the surface texture of the Nextel paint used, the DE measurement described in the next section shows the surface texture of the paint can change the DE of the paint significantly (emissivity differences of 0.06).

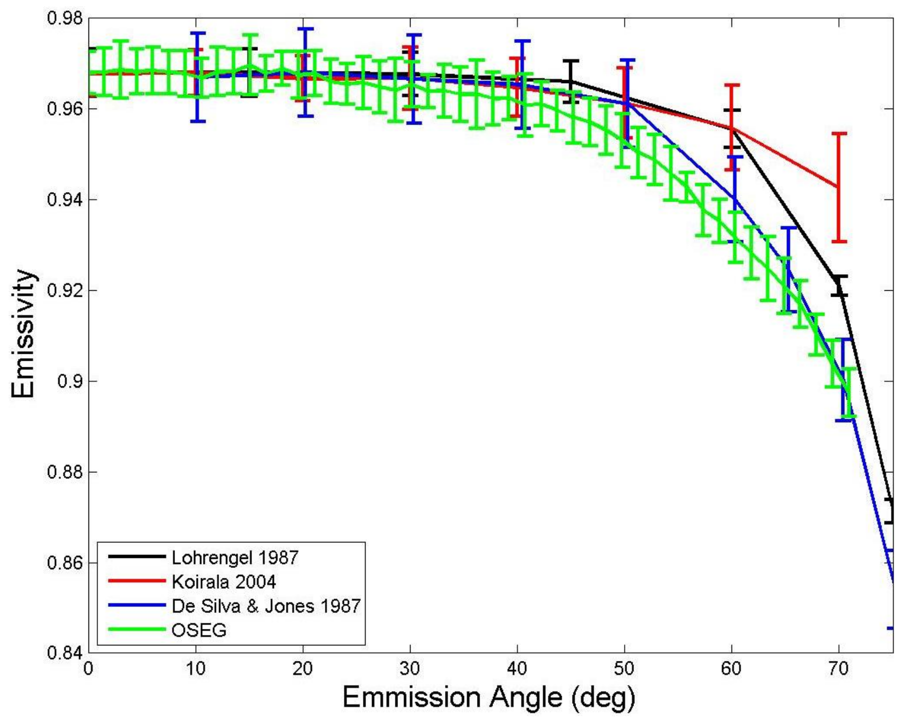

Figure 78: Comparison between DE measurements of Nextel black paint by OSEG and other IR goniometers (Lohrengel 1987; Koirala 2004; De Silva & Jones 1987)**.**

6.1.10 DE Measurements of Nextel target with Different Surface Roughness.

A second target was constructed by roughly painting with Nextel to create a rough undulating texture on millimetre and submillimetre surface scales (Figure 79). The DE of this rough target was measured using the same setup as the smooth target shown in Figure 69. Throughout this thesis the target shown in Figure 69 will be referred to as the 'smooth' target and the target shown in Figure 79 will be referred to as the 'rough' target. As seen in Figure 80 the DE of the two surfaces are in good agreement (the DE is the same within the measurement error) between 0 – 40^{o} emission angles. However, at higher emission angles the rough target shows a sharper drop in emissivity with emission angle (Figure 80). This measurement suggests that at high emission angles the DE is dependent on the roughness or the texture of the surface.

Figure 79: Roughly painted Nextel Velvet black aluminium target 50 mm in diameter.

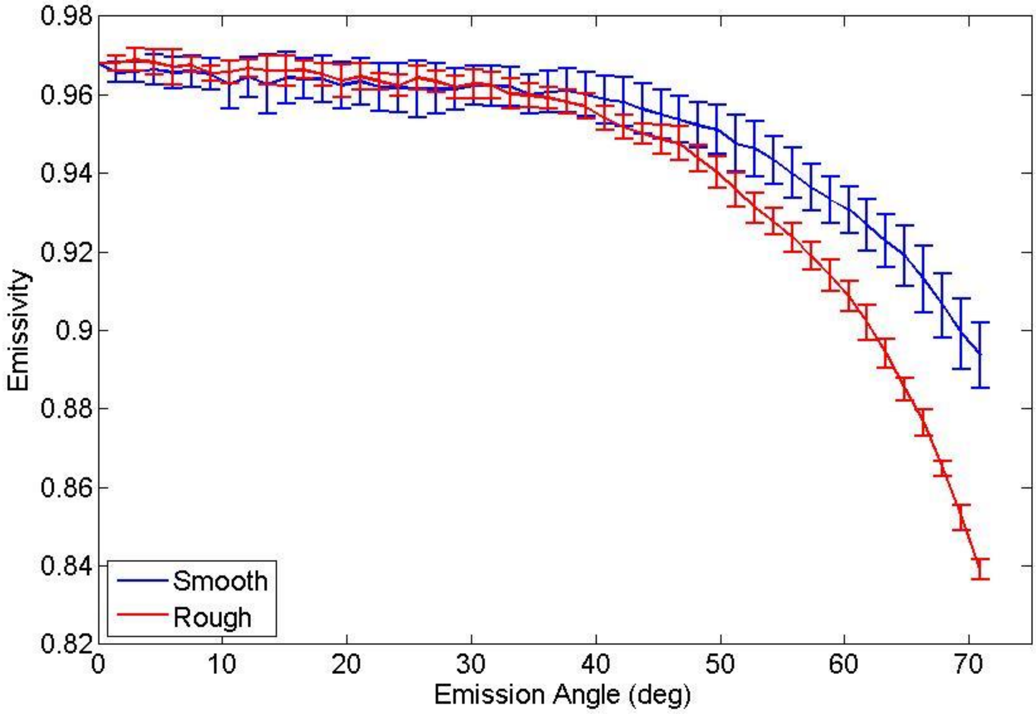

Figure 80: DE measurements of two Nextel targets with different surface roughness profiles. The error bars are calculated from the standard deviation of all measurements made at that emission angle. For each run ten measurements are made at each emission angle as the radiometer carriage moves down and ten measurements are made at each emission angle as the radiometer moves up.

7 Example of Modelling DE and the Effects of Surface Roughness: Nextel paint

In this chapter the two thermal infrared DE models described in section 1.5 (the Hapke emission model and the Fresnel emission model) are used to model the DE results of the smooth Nextel target (Figure 75).

7.1 Hapke Model

The dependence of emissivity of the Nextel surface with emission angle is predicted by Hapke (2014) (see section 1.5.2). Hapke's model is valid for any particulate medium that is at a uniform temperature; so it should be valid for the smooth Nextel target as the surface is uniform in temperature (±0.1 K – as previously described in section 6.1.2) and Nextel black paint is primarily made up of spherical polyurethane balls that range from 20 – 100 µm in diameter (described in more detail later section 7.3). However, Hapke's emission model does not fit the measured DE of Nextel black paint (Figure 81). Hapke's emission model predicts a more isotropic DE and does not capture the large (Δ 0.1) drop in emissivity observed with increasing emission angle.

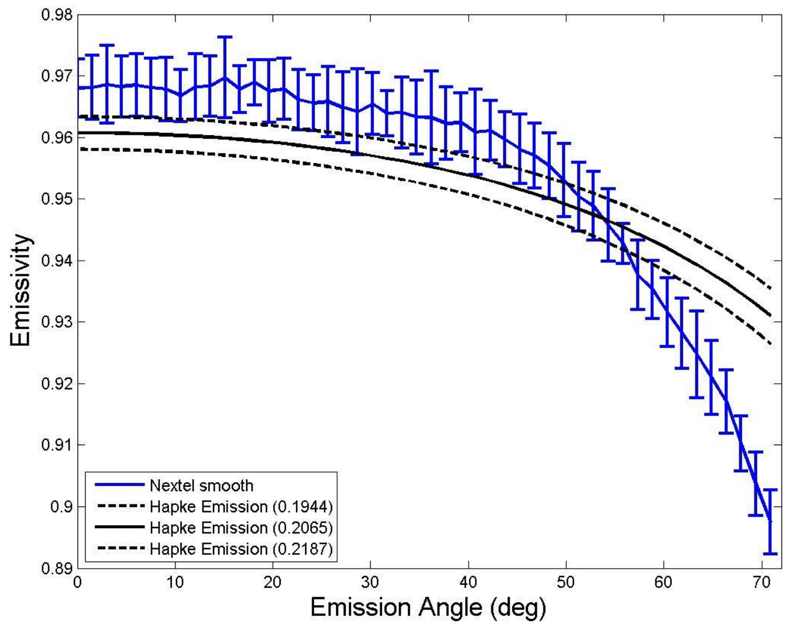

Figure 81: Best fit Hapke emission model described in section 1.5.2. An unconstrained Matlab least squares fitting algorithm was used with the single scattering albedo as a free parameter to find the best fit line. The best fit (solid black line) was found for an $\boldsymbol{w} = \mathbf{0.207}$ (single scattering albedo). The dotted black lines represent the 95% confidence interval of the unconstrained least squares fit.

7.2 Fresnel Equation

The Fresnel Equations (section 1.5.4) were also used to model the DE of Nextel black paint. The two free parameters in the Fresnel equations are the optical constants of the material n and k. Equation 12 states that the optical constant k is dependent on the electrical properties of the material and as the electrical conductivity of the material tends to zero, so the extinction coefficient (k) tends to zero.

7.2.1 Electrical Conductivity of Nextel

The electrical conductivity of Nextel was measured by creating a cylinder of Nextel paint 2 cm tall and 1.8 cm in diameter. A wire contact was embedded into the paint at both ends of the cylinder. The resistance of the paint was then measured using a Mega-ohmmeter and found to be 386 MΩ. The electrical conductivity of the paint was then calculated using equation 42 as $2 \times 10^{-7}\ \Omega^{-1}m^{-1}$. For comparison the electrical conductivity of metal conductors such as copper is $1.7 \times 10^{8}\ \Omega^{-1}m^{-1}$ and for insulators such as glass is $10^{-11}\ \Omega^{-1}m^{-1}$.

$$\sigma_e = \frac{L_c}{R_e A} \qquad \textbf{42}$$

Where σ is the electrical conductivity of the material, R_e is the electrical resistance of the cylinder of Nextel paint measured between the two wire contacts, A is the cross sectional area of the cylinder and L_c is the length of cylinder.

With a near zero electrical conductivity, from equation 12 the extinction coefficient can be approximated as zero, this simplifies the Fresnel equations to those given in equations 16 and 17 for a perfect dielectric. Using a least square fitting algorithm with the one free parameter (the index of refraction, n)

the Fresnel equations for a perfect dielectric were used to fit the DE measurements for the smooth Nextel target (Figure 82).

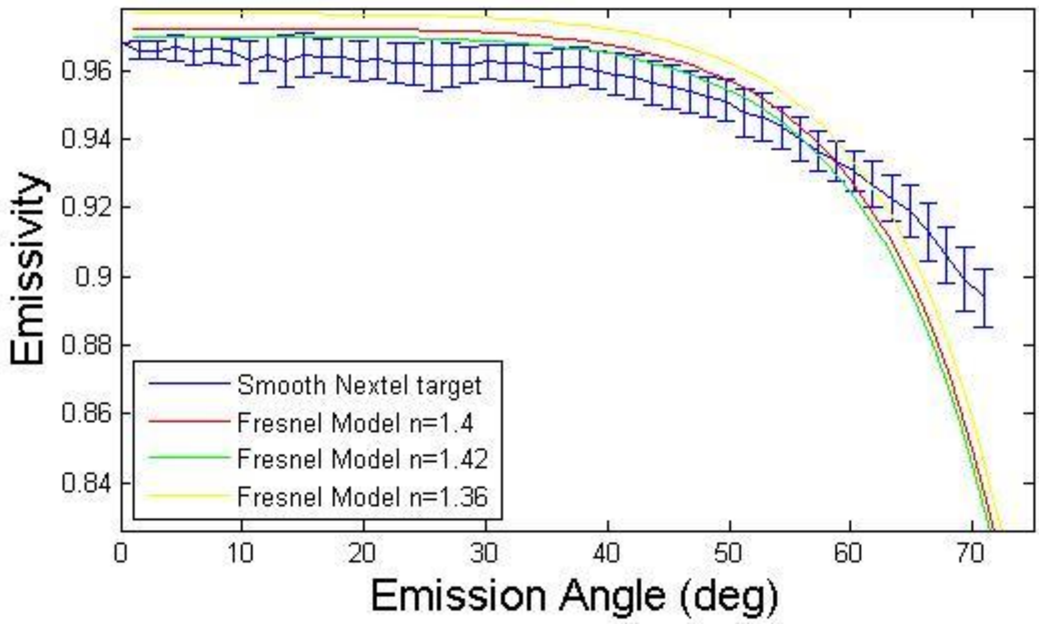

Figure 82: Best fit Fresnel model (red) for measured DE of Nextel (blue). The 95% confidence interval of the unconstrained least squares fit is shown in green and yellow.

For the smooth Nextel black target at large emission angles the values of the DE are larger than the Fresnel equations predict for an ideal dielectric. In the three previous DE measurements made of Nextel, only De Silva & Jones (1987) discuss the difference between the measured DE values and the Fresnel predicted values. De Silva & Jones (1987) suggest two possible reasons for this difference:

1. Some emission from the metal substrate below the Nextel paint could be 'seen'. The DE of aluminium increases with emission angle up to emission angles greater than 80^o.
2. The surface of Nextel black paint is sufficiently rough at the micron scale that an increase in DE with emission angle compared to an ideal dielectric is possible.

The extinction coefficient describes the attenuation of the radiation through the medium and for Nextel paint it has been shown to be almost zero. The material is therefore highly absorbing and it is unlikely that thermal radiation from the underlying metal surface is 'seen'. It was therefore believed that the surface roughness was the reason for the difference between the Fresnel predicted DE response and the measured DE. Further modelling work was completed to try to better understand the effect of surface roughness on the DE.

7.3 Multiple Slope Fresnel Model

The Fresnel model was adapted to try to account for surface roughness affects by modelling the surface as a set of slopes with a Gaussian distribution. The Gaussian slope roughness model was taken from Bandfield et al. (2015) and used to model the DE of the smooth Nextel target. The model calculates the radiance emitted from slopes of 0^o to 90^o at 1^o intervals.

The radiance of each slope is calculated using the Fresnel equations for a perfect dielectric and its contribution to the total modelled radiance is weighted by the Gaussian statistical probability of its occurrence. This reduces surfaces slopes to a single parameter – the RMS slope – that is independent of length scale.

The probability distribution P for a given slope angle is given in Bandfield et al. (2015) as:

$$P(\theta_s) = \frac{\tan(\theta_s)}{\tan^2(\theta_0)} \cdot e^{-\frac{\tan^2(\theta_s)}{2\tan^2(\theta_0)}} \qquad \textbf{43}$$

Where θ_0 is the tangent of the RMS slope angle and θ_s is the angle of the slope from the surface normal. This describes the adirectional distribution of slopes that closely approximates a Gaussian distribution of unidirectional slopes for a RMS slope angle of θ_0 (Bandfield et al. 2015).

Using the probability distribution in equation 43 the model calculates the mixture of Fresnel calculated DEs for each slope angle in proportion to their contribution to the measurement FOV based on the observational geometry. For example slopes facing away from the observer will contribute proportionally less to the observed radiance than slopes facing the observer. This factor is accounted for in the model from the dot product of the vector normal to the local surface and the observation vector (Bandfield et al. 2015).

The multiple slope model did not fit the measured DE of Nextel well (R^2 value of 0.73, Figure 83). Using a constrained least squared fit, the best fit was found to be a RMS slope value of 25^o and an n of 1.42. The RMS slope was constrained to be between 0 – 90^o and n between 0 – 10. Although the multiple slope model does account for roughness, it does not account for multiple scattering between surfaces. This can be modelled using a Monte Carlo ray tracing technique.

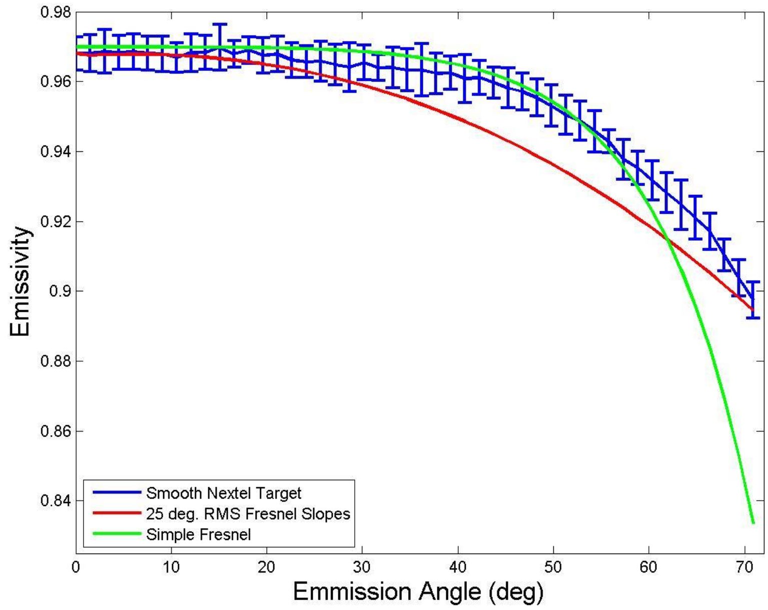

Figure 83: Best fit Multiple Slope Fresnel Model (red), measured DE of smooth Nextel target (blue) and best fit Fresnel model (green).

7.4 Monte Carlo Ray-Tracing Method

Both multiple scattering and shadowing are inherently taken into account with ray-tracing. Shadowing occurs when certain sections of a rough surface are blocked from the view of the incident ray and multiple scattering is when radiation interacts more than once against a rough surface (Figure 84) (Bergström 2012; Bergström et al. 2007; Bergström et al. 2008). Random rough surfaces are usually characterised in statistical terms using two distribution functions, the height distribution ($P(\zeta(x,y))$) in the vertical direction and the autocovariance function ($\bar{C}(\tau)$) in the lateral directions. The height distribution describes the height deviation from a certain mean reference level and the autocovariance function describes the typical distance between two similar features (e.g. hills or valleys).

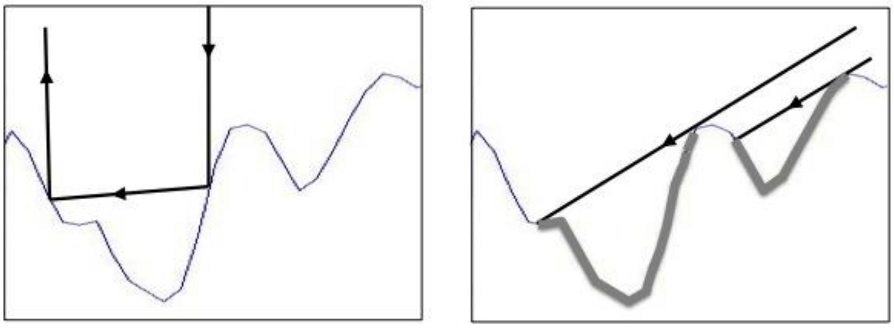

Figure 84: Multiple (double) scattering shown on left and shadowing shown on right. Both are inherently taken into account with ray-tracing.

If a random rough surface is described by the function $z = \zeta(x,y)$ then the height probability function is given in equation 44.

$$P(\zeta) = \frac{1}{H_{rms}\sqrt{2\pi}} e^{-\frac{\zeta^2}{2(H_{rms})^2}} \quad \textbf{44}$$

Where H_{rms} is the root mean square (RMS) height. The autocovariance function is normally defined using a Guassian function as:

$$\bar{C}(\tau) = H_{rms}^2 e^{-\frac{|x_1 - x_2|^2}{\tau^2}} \quad \textbf{45}$$

Where x_1 and x_2 are two difference points along the surface and τ is the correlation length (the typical lateral distance between two features on a surface). See Figure 85 for an example of surfaces with the same H_{rms} but different correlation lengths.

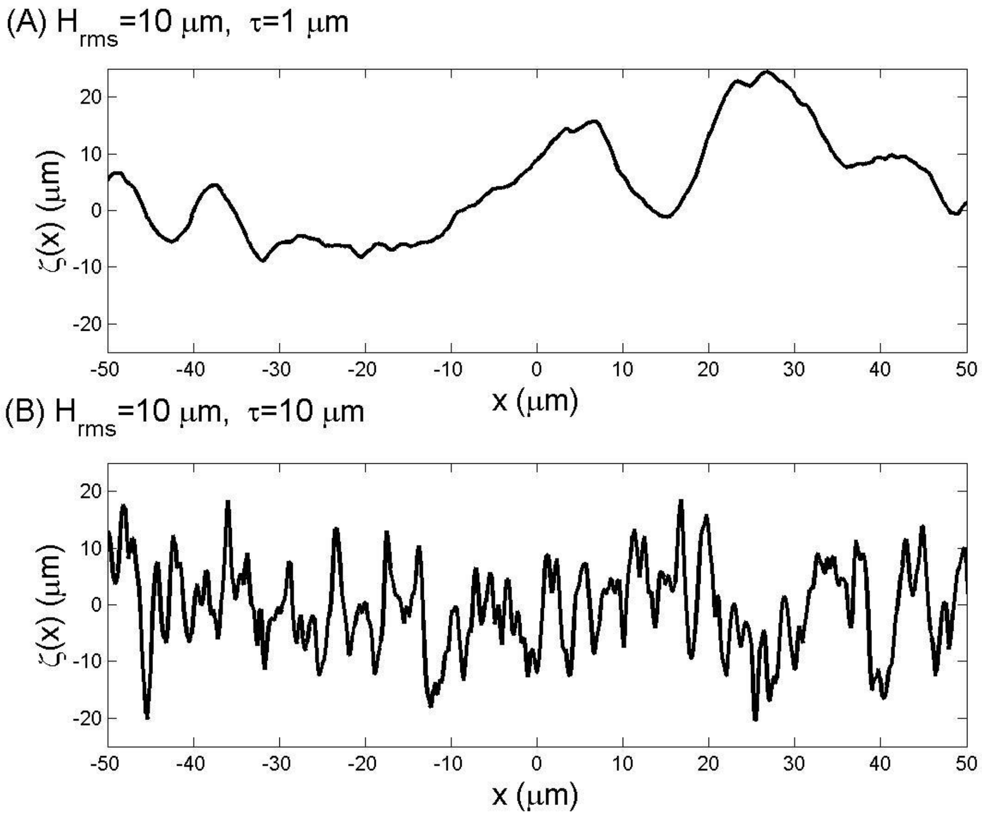

Figure 85: Two Gaussian random rough surfaces with the same H_{rms} (10 μm), but different correlation lengths. (A) Surface profile with correlation length 1 μm. (B) Surface profile with correlation length 10 μm.

In light scattering theory, ray-tracing is an energy approximation where bundles of radiation rays are traced throughout their interactions with a rough surface until they leave the surface. At each interaction the surface is treated as locally smooth so that each scattering event on the surface can be treated as a specular reflection and can be modelled using the Fresnel equations (described in section 1.5.4.3) – this is known as the Fresnel approximation (Bergström et al. 2007). Tang et al. (1996) showed that the Fresnel approximation is valid for:

$$\frac{H_{rms}\cos(\theta_i)}{\lambda} > 0.17 \qquad \frac{H_{rms}}{\tau} < 2 \tag{46}$$

Where H_{rms} and τ are the RMS height and the autocorrelation length of the surface, respectively, λ is the wavelength of the radiation and θ_i is the angle of incidence. As the DE is measured by heating the sample from below, there is no light source and the angle of incidence is defined to be unity. The wavelength selection for the DE measurements was defined by the roll off of the KBr window at 25 µm, therefore provided the H_{rms} of the sample is greater than 4.25 µm and the ratio of the H_{rms} to the correlation length is smaller than 2, the Fresnel approximation will be valid.

The ray-tracing algorithm and source code used to model the DE of the Nextel smooth black painted surface, is available to download from the internet (Bergström 2012). A full description of the algorithm is given in Bergström et al. (2007) and a brief description is repeated here (Figure 86). As this algorithm is designed to model the BRDF of samples it was slightly modified to calculate the DE from the angular reflection using Kirchhoff's law in step 7 (see Figure 86). '

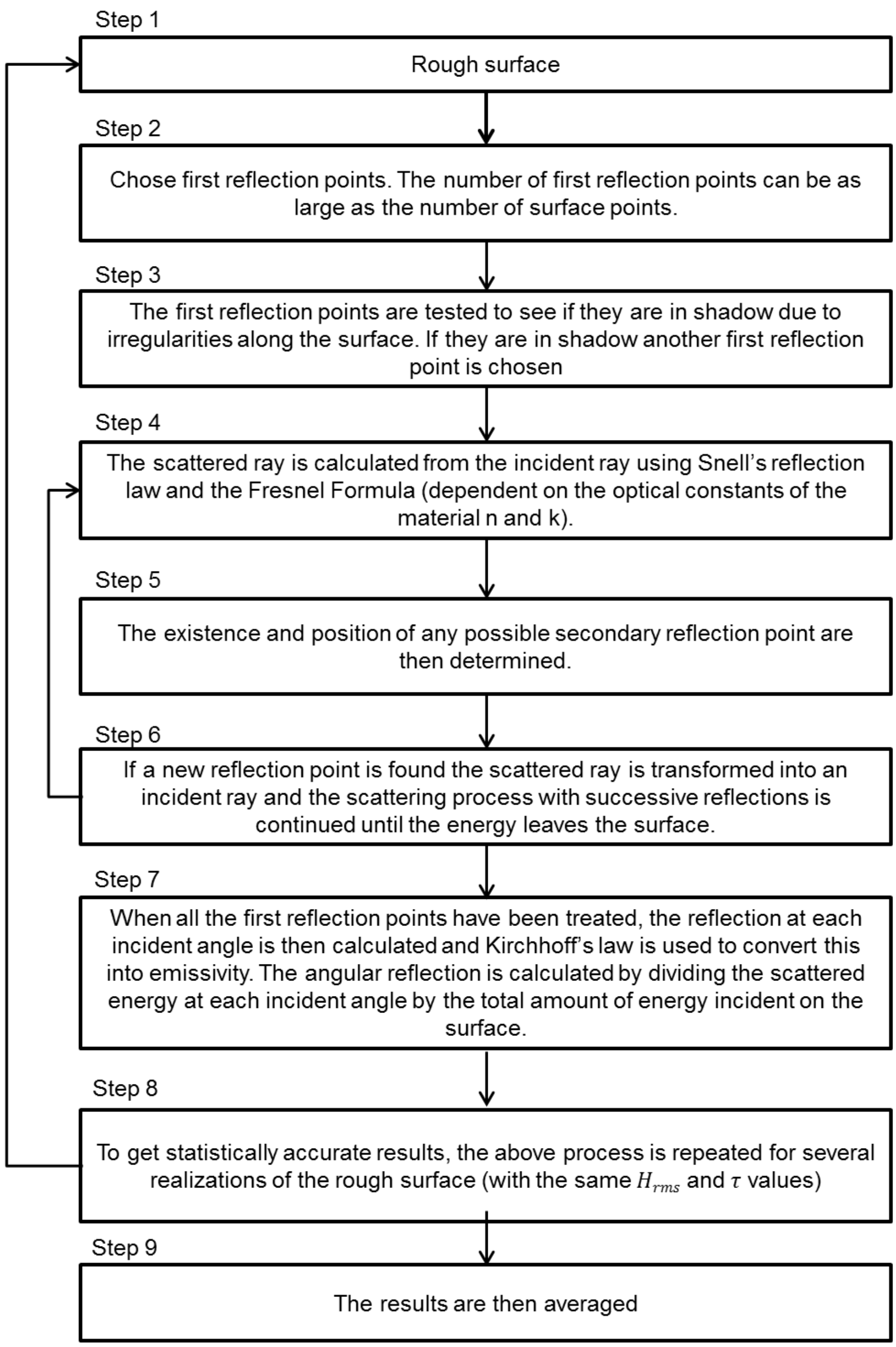

Figure 86: Flow diagram giving a brief description of the Monte Carlo ray-tracing algorithm used to model the DE of the smooth Nextel surface. Step 7 was modified to calculate the DE instead of the BRDF. A full description of the algorithm is given in Bergström et al. (2007).

7.5 Nextel Surface Roughness Measurements

To model the DE of the smooth Nextel target using the ray-tracing technique, its surface roughness profile was measured under a visible light microscope (Figure 87). Roughness features were observed on scales approximately 100 µm. When illuminated with blue (488 nm) light the polyurethane balls that make up Nextel fluoresced green (Figure 88). The image in Figure 88 is 1.1 mm across and as such can be analysed to show that the largest polyurethane ball is approximately 20 µm in diameter. The roughness profile of the smooth Nextel target was further measured using a Polytec TopSens configurable Chromatic Confocal Point Sensor (Polytec Limited 2015) that can measure surface roughness at 3 nm resolution (Figure 89 and Figure 90). Table 16 gives a summary of the measured surface roughness profile, the RMS height distribution was found to be 13.5 µm and the autocorrelation distance was 95 µm.

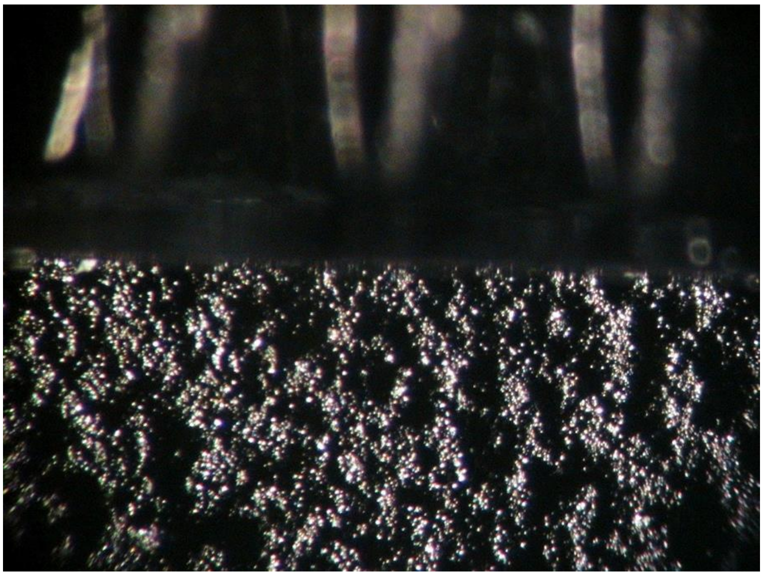

Figure 87: Visible light microscope image of smooth Nextel target illuminated by natural white light. At the top of the image is a ruler with mm grading's for reference.

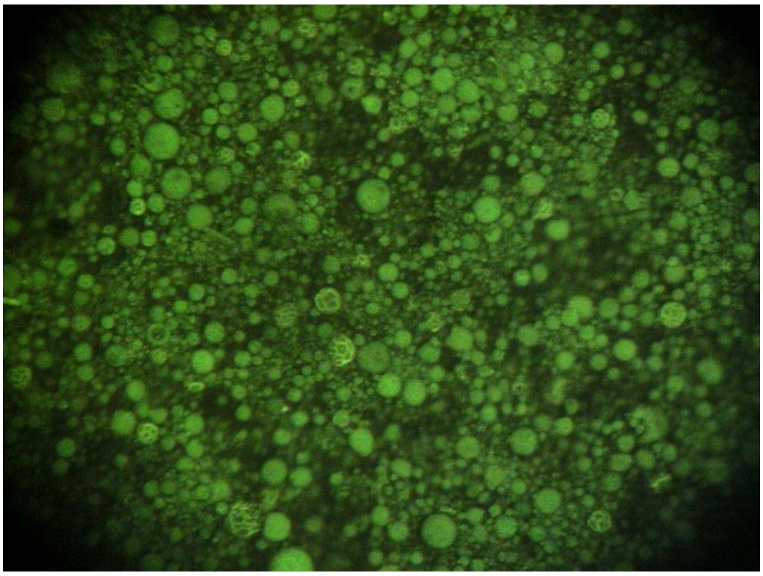

Figure 88: Visible light microscope image of Nextel painted aluminium target illuminated with blue (488 nm) light. The image is 1.1 mm across. The visible 'circles' are the polyurethane balls that make up the Nextel paint.

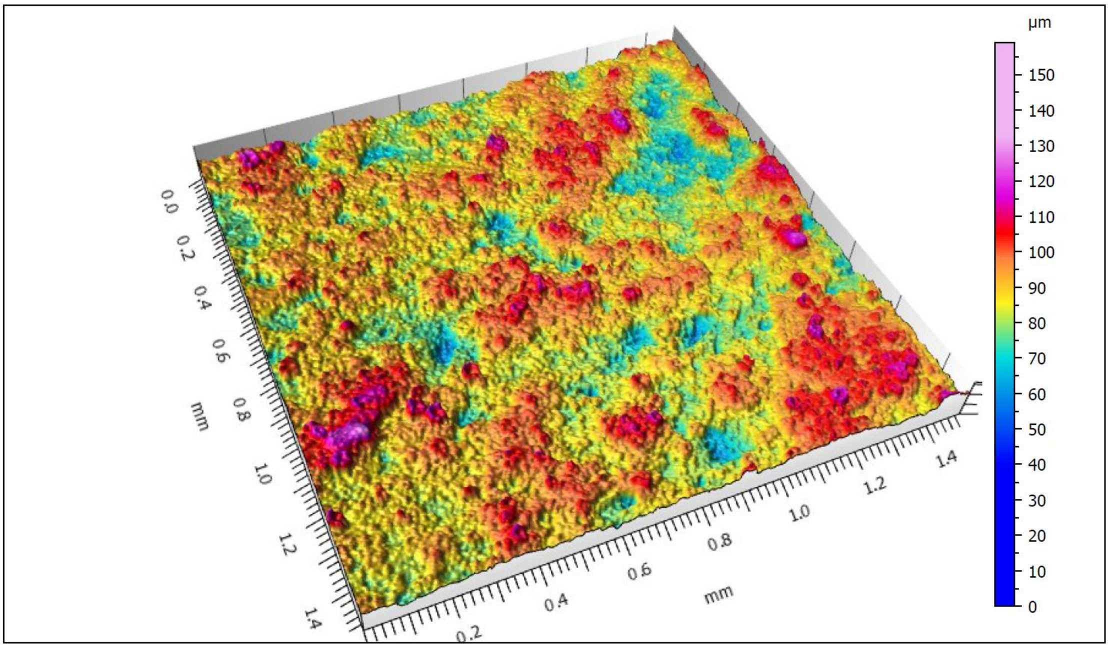

Figure 89: Three dimensional surface roughness profile of the smooth Nextel target.

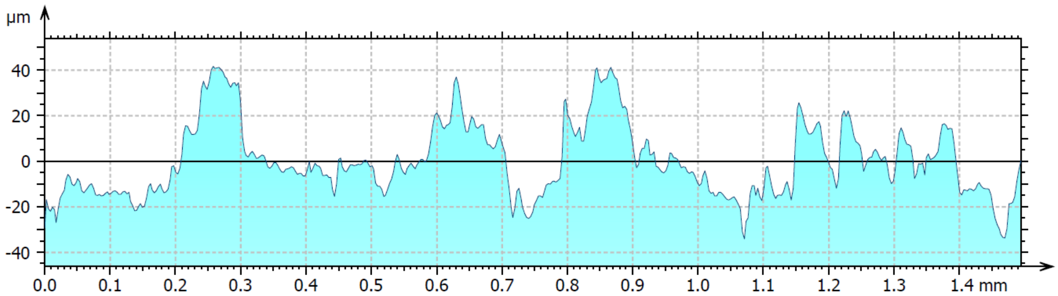

Figure 90: Two dimensional slice of the surface roughness profile of the smooth Nextel target.

Table 16: Summary of measured surface roughness profile values for smooth Nextel target.

Surface Roughness parameter	Measured value
RMS height	13.5 μm
Autocorrelation Length	95 μm

7.6 Monte Carlo Ray-Tracing Model of Nextel

The measured surface roughness profile of the smooth Nextel target was fed into the Monte Carlo ray-tracing model. As described in section 7.2.1 the extinction coefficient of Nextel was shown to be approximately zero, therefore using the measured surface roughness profile the ray-tracing model only has one free parameter, the real part of the index of refraction (n). At an emission angle of zero, it was assumed that there is no multiple scattering and the emissivity is then defined only by the Fresnel formula. This then implies that the optical constant of the material must be 1.43. Using this optical constant the ray-tracing model was run to give the DE shown in Figure 91. The ray-tracing model fits the measured DE measurements very well with an R^2 value of 0.995. The ray-tracing model also records the average number of scattering events at each emission angle (Figure 92) showing that the average number of scattering events between rough surfaces elements becomes significantly greater than unity at emission angles greater than 40^o. This could explain why the Fresnel model only deviates from the measured DE values at large emission angles (>55^o, Figure 91) as at smaller emission angles there is very little multiple scattered radiation.

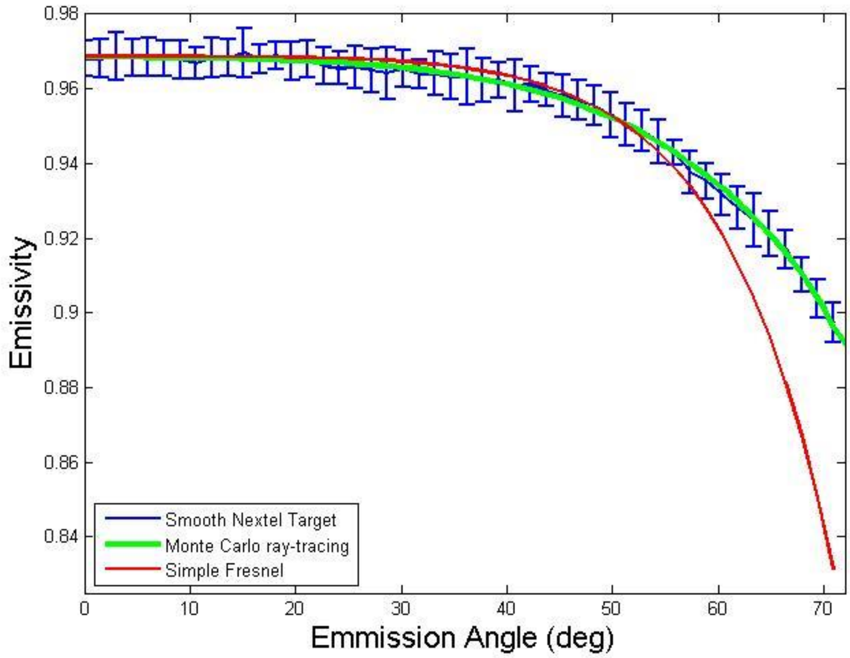

Figure 91: Monte Carlo ray-tracing model, with n=1.43, RMS height 13.5 µm and autocorrelation length 95 µm.

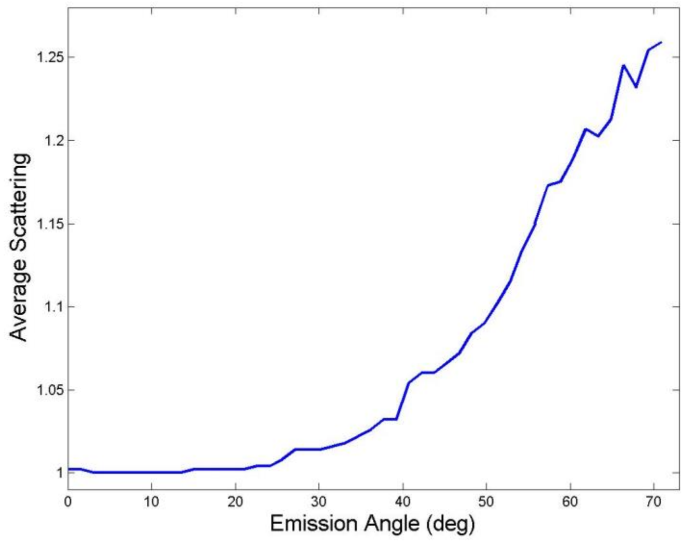

Figure 92: The average number of scattering events at each emission angle. For an average scattering of greater than unity some multiple scattering has occurred at that emission (see Figure 84)**.** One can see that multiple scattering does not become significant until ~45^{o}.

7.7 Summary of Nextel DE Measurements and Modelling

The Nextel measurements have shown that the DE is dependent on the surface roughness at lengths scales from micrometres to millimetres. The modelling work has shown that to account for the surface roughness multiple scattering between surfaces must be included. The multiple scattering becomes important at emission angles greater than 45$^{o.}$ On a rough surface the DE of an ideal Fresnel surface will drop more sharply compared to a smooth surface at emission angles greater than 45^{o} (Δ0.06 emissivity difference between Fresnel model and measured DE at 70^{o} emission angle).

8 Broadband Thermal Infrared DE Measurements of Lunar Analogue Material JSC-1AF

Measurements of the lunar analogue material JSC-1AF have been made using the OSEG. JSC-1AF is a commonly used mechanical and spectral analogue of the fine grain lunar mare regolith that has an average particle size of 25 µm (Carpenter et al. 2006). These measurements were acquired so the measured DE could be fed back into three dimensional thermal physical models. The results in this section are initial results to allow an approximation of the DE of a lunar analogue material to be made and further investigation and measurements of the DE of JSC-1AF are required. In section 1.3.2 two discrepancies were described between the Diviner measured lunar surface temperatures and the surface temperatures calculated from three dimensional thermal physical models. The larger of the two discrepancies occurred in the daytime in PSR (permanently shadowed region) and the second smaller discrepancy was during the night-time across all regions.

To measure the DE during the daytime would require an illumination arm that is not currently implemented on the OSEG. Therefore only night-time DE measurements can be made where the sample is heated up from below. These measurements should be made under vacuum with the cold shield switched on to simulate a space-like environment. However, investigations with JSC-1AF have shown the thermal conductivity of the material drops dramatically when under vacuum. For example, if the base of the sample holder is heated to 200^{o}C (the maximum temperature of the sample cup under a vacuum) the top surface of the sample reaches ~30^{o}C – just above the ambient temperature. Whereas under atmospheric pressure the thermal conductivity is better and the top surface can be heated to ~ 50^{o}C when the base of the sample holder is heated to 100^{o}C. Therefore under vacuum (10^{-6} mbar) when the cold shield is switched on the top surface of the sample would drop to ~150 K (the temperature of the cold shield). This would not provide enough thermal infrared signal to measure the DE and would be impossible to control the temperature of the sample accurately. Therefore only DE measurements under atmospheric pressure have been made. A measurement under vacuum without the cold shield switched on has also been made to demonstrate the extra noise induced in the measurement due to the low thermal conductivity of the sample.

8.1 Details of the DE measurement of JSC-1AF

The OSEG was setup in the same way as outlined in section 6.1.3 for measuring the smooth Nextel target. Details of the measurement are given in Table 17. The sample cup is 50 mm is diameter and 3 mm deep. The JSC-1AF sample was poured into the cup, pressed down and smoothed over. This created a macro (surface roughness <100 μm) scale smooth top surface.

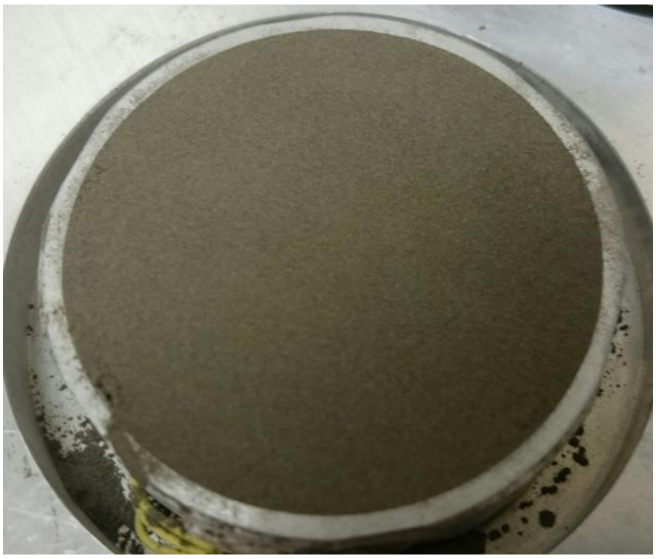

Figure 93: JSC-1AF poured into the 50 mm diameter sample cup.

Table 17: Summary of OSEG setup used to measure JSC-1AF

Measurement Parameter	**Value**
Pressure	Atmospheric (1 bar)
Cold Shield Temperature	Ambient (~20^{o}C)
Wavelength Selection	0.2 – 25 µm
Base of Sample Cup Temperature	90-120^{o}C
Chopping Frequency	10 Hz
Settling time	30 s
Lock-in time constant	1 s

8.2 Details of the DE Measurement Calibration

The calibration of the JSC-1AF sample was done in a similar fashion to the calibration of the Nextel target (section 6.1.4), except the normal emissivity of JSC-1AF was taken to be 0.876. This is its average emissivity under ambient condition across the wavelength region 4 – 25 µm (Figure 94) (Thomas et al. 2012). Equation 47 then gives the calibration used to convert the raw lock-in voltage to DE.

$$\varepsilon_d(\theta_e, T) = 0.876\frac{V(0^o, T)}{V(\theta_e, T)} \qquad \textbf{47}$$

Where $\varepsilon_d(\theta, T)$ is the DE, $V(\theta_e, T)$ is the recorded raw lock-in voltage, $V(0^o, T)$ is the raw lock-in voltage recorded at 0^o emission angle. By this equation an isotropic surface emitter will have a DE of 0.876 for all emission angles.

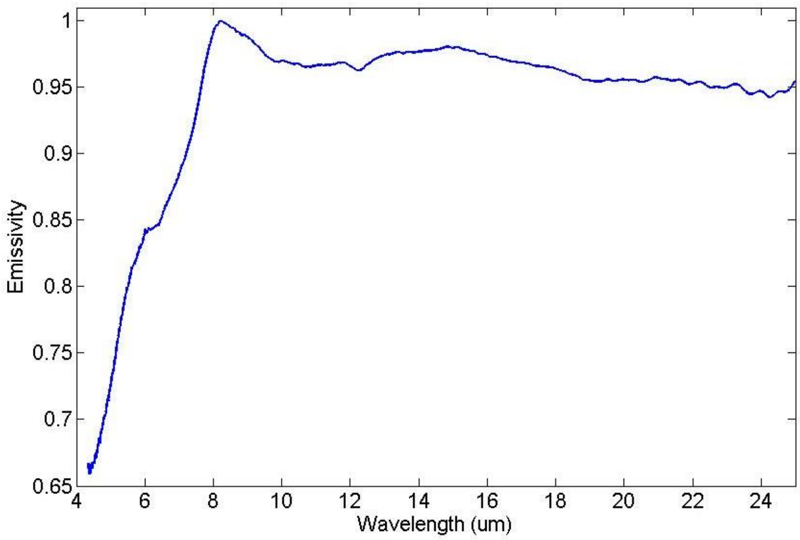

Figure 94: JSC-1AF emissivity spectra measured under ambient conditions. After (Thomas et al. 2012)**.**

8.3 DE Measurement of JSC-1AF

Figure 95 shows the DE of JSC-1AF measured under ambient conditions using the setup outlined in Table 17 and Figure 96 shows the same measurement was made under 10^{-6} mbar vacuum. Unfortunately as described before, the SNR is greatly reduced under vacuum due to the poor thermal conductivity of JSC-1AF. At emission angles greater than 35^{o} the measured DE of JSC-1AF is anisotropic and decreases with increasing emission angle (Figure 95). This is a very important result for three dimensional thermal physical models that try to replicate the surface temperatures of airless bodies using isotropic scattering.

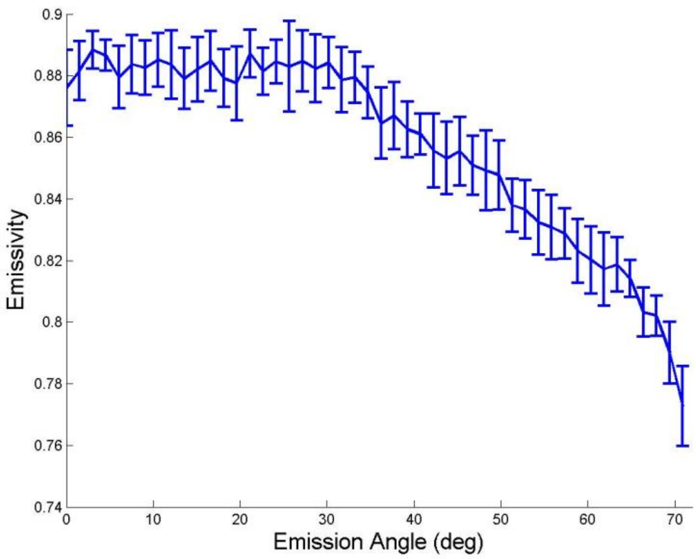

Figure 95: DE measurement of JSC-1AF made by the OSEG under ambient pressure. Measurements were made in 1.5^{o} steps of emission angle. At each emission angle step 20 measurements were taken, the error bars represent the standard deviation of measurements made at each emission angle.

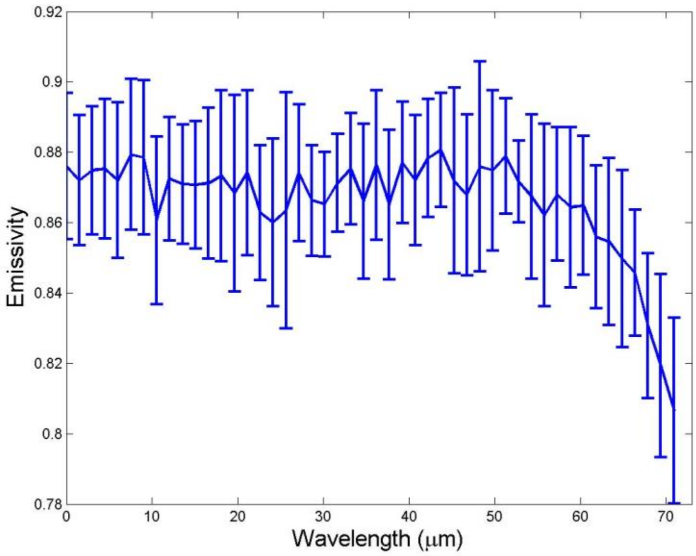

Figure 96: DE measurement of JSC1-AF made under 10^{-6} mbar. The SNR is greatly reduced under vacuum due to the poor thermal conductivity of the powder. The temperature of the top surface of the powder is ~10 K above the ambient temperature despite the base of the sample cup being controlled to 180^{o}C. Therefore the top surface of the sample will vary in temperature as the temperature cannot be controlled by the PID loop.

8.4 Hapke DE Model of JSC-1AF

The Hapke DE emission model was fitted to the DE measurement of JSC-1AF using an unconstrained Matlab least squares fitting algorithm with the single scattering albedo as a free parameter. The Hapke model found to fit the measured DE reasonably well (R^2 value of 0.91) was for a single scattering albedo of 0.4978. The fitted single scattering albedo value would imply an albedo factor ($\gamma = \sqrt{1-\omega}$) of 0.72 that is similar to previously measured values ($\gamma = 0.75$) in the wavelength range of 8 – 25 µm (Gaier et al. 2011). This similarity gives further confidence in the Hapke DE model.

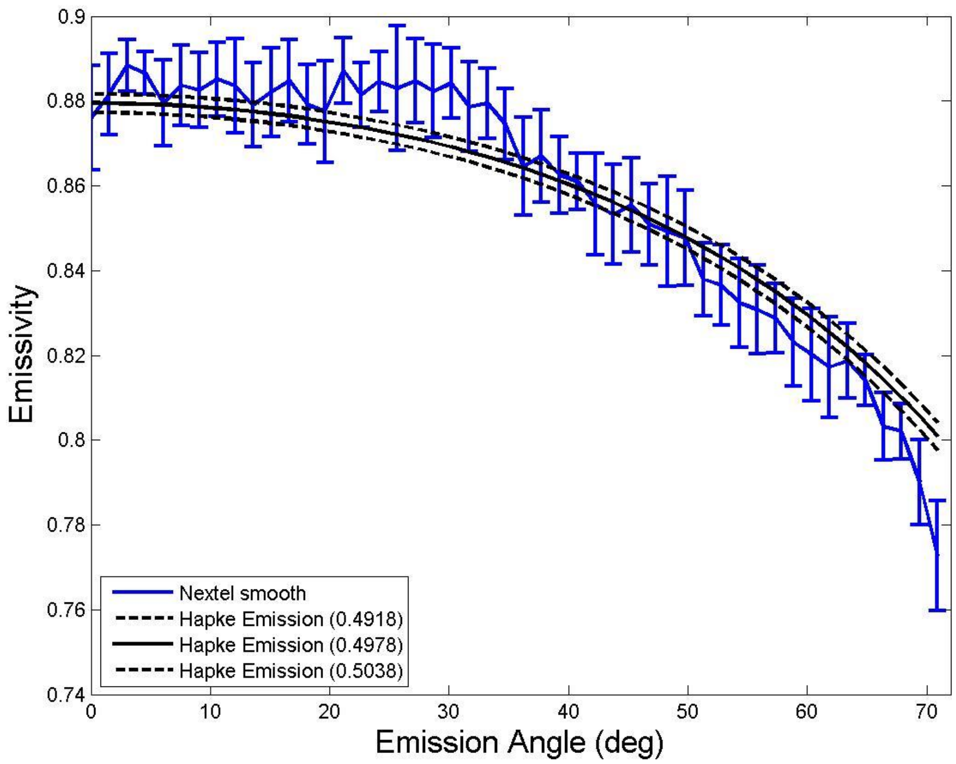

Figure 97: Best fit Hapke modelled DE (described in section 1.5.2) to the measured DE for JSC-1AF. The fit was made using an unconstrained least squares fitting algorithm with the single scattering albedo as a free parameter. The best fit (R^2 value of 0.91) was found with a single scattering albedo of 0.5 (solid black line). The 95% confidence bounds are shown in the dotted black line with a single scattering albedo of 0.49 and 0.51.

8.5 Monte Carlo Ray-Tracing Modelling the DE of JSC-1AF

The measured DE of JSC-1AF was also modelled using the same Monte Carlo ray-tracing approached used to model the smooth Nextel target (section 7.4). In the case of the smooth Nextel target the surface roughness profile was measured and then used in the model. However, for the JSC-1AF sample the surface roughness profile has not been measured and must be assumed using its particle size distribution given in Carpenter et al. (2006). Therefore a random rough surface must be generated with Gaussian surface roughness statistics (H_{rms} and τ) that can then be fed into the Monte Carlo ray-tracing algorithm.

8.5.1 Surface Generation of Randomly Rough Surfaces with Gaussian Statistical Roughness Values

A random rough surface with Gaussian roughness statistics (H_{rms} and τ) was required for modelling the JSC-1AF surface using the ray-tracing algorithm. For modelling and simulative purposes random rough surfaces with Gaussian statistics can be generated by convolving a set of random surface points (e.g. white noise) with a Gaussian filter of the required statistics (Garcia & Stoll 1984). This was achieved using the Matlab function rsgeng1D (downloaded from Bergström (2012)).

8.5.2 Optical Constants of JSC-1AF

To model the DE of JSC-1AF using the Monte Carlo ray-tracing technique the optical constants of the medium are also required as well as the surface roughness profile. The real index of refraction of JSC-1AF has been measured using the Becke line technique and reported to be 1.592 ±0.01 at a wavelength of 659 nm (Reed 2013). Assuming there is no multiple scattering at an emission angle of zero and the emissivity is controlled only by the Fresnel formula (Equation 20 and 21), the extinction coefficient can be calculated as 0.72. As the average particle size of JSC-1AF is 25 µm, the H_{rms} is assumed to be of the order tens of microns and the correlation length slightly larger at a hundred microns (Figure 98).

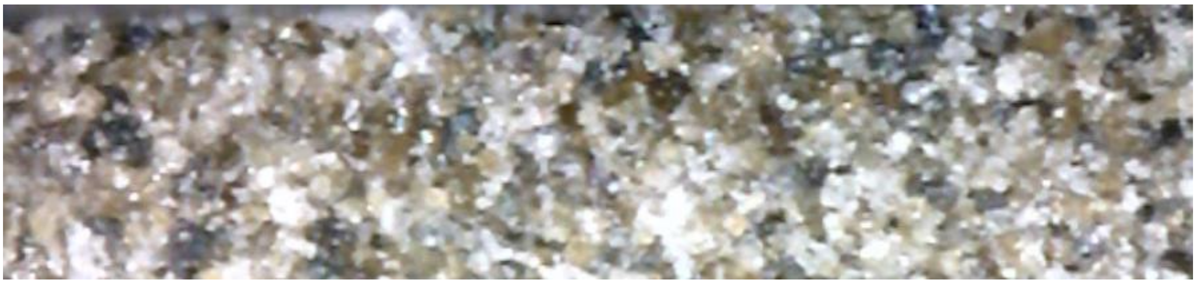

Figure 98: Microscope image of the JSC-1AF sample. The image is 1 mm in width and roughness scales of the order 10 – 100 µm can be observed.

A fit was found using a Matlab constrained least squares algorithm assuming an index of refraction of 1.59, extinction coefficient of 0.72 and allowing the values of the H_{rms} and correlation length to be constrained free parameters (Figure 99). H_{rms} was limited to between 10 – 30 µm and the correlation length between 50 – 100 µm, a best fit DE was achieved when H_{rms} was 15 µm and τ was 100 µm. The Monte Carlo ray-tracing model gave an R^2 value of 0.95 compared to an R^2 value of 0.64 for the Fresnel only model.

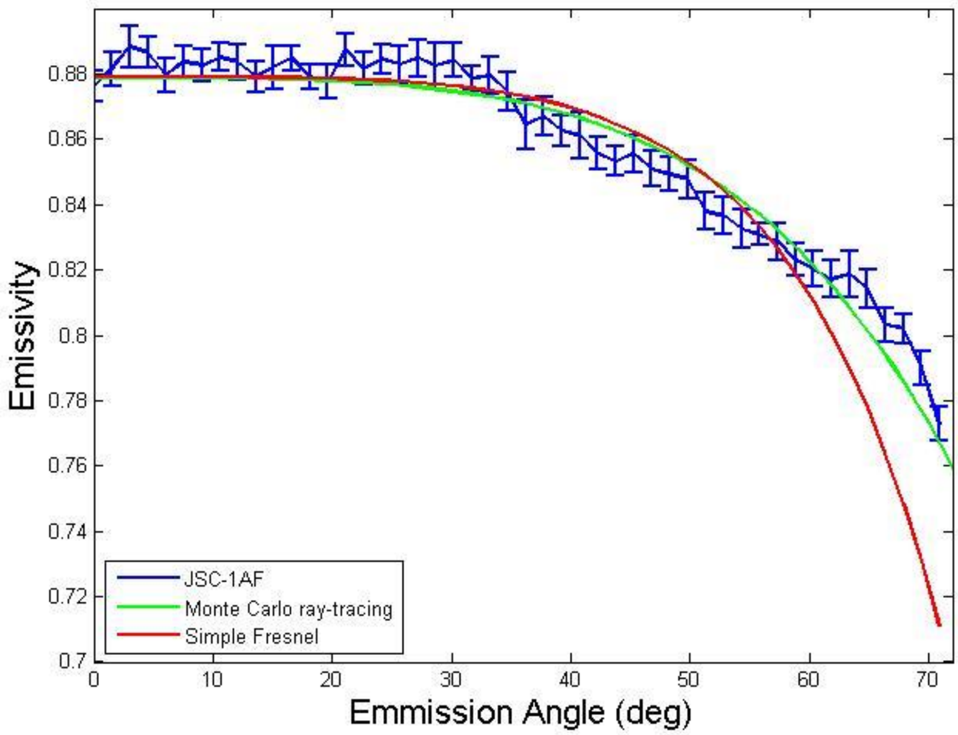

Figure 99: Monte Carol ray-tracing model of measured DE for JSC-1AF (blue).

8.6 Diviner Measured Large Scale DE of Lunar Surface

Recently large scale broadband DE measurements of the lunar surface measured using Diviner have been published (Figure 100) (Bandfield et al. 2015). In this subsection these measurements are briefly described and compared to the laboratory measured DE of JSC-1AF. These measurements were made by rolling the Diviner instrument to make off nadir measurements to change the emission angle observed from the lunar surface. Measurements were made of a target surface region from a series of emission orientations ~0, 53, 62, 69 and 76^{o}. The emissivity calculated was the apparent emissivity.

This was calculated by assuming that the nadir emissivity was 0.99, all other emissivity values are then reference to this emissivity by assuming the surface temperature has not changed.

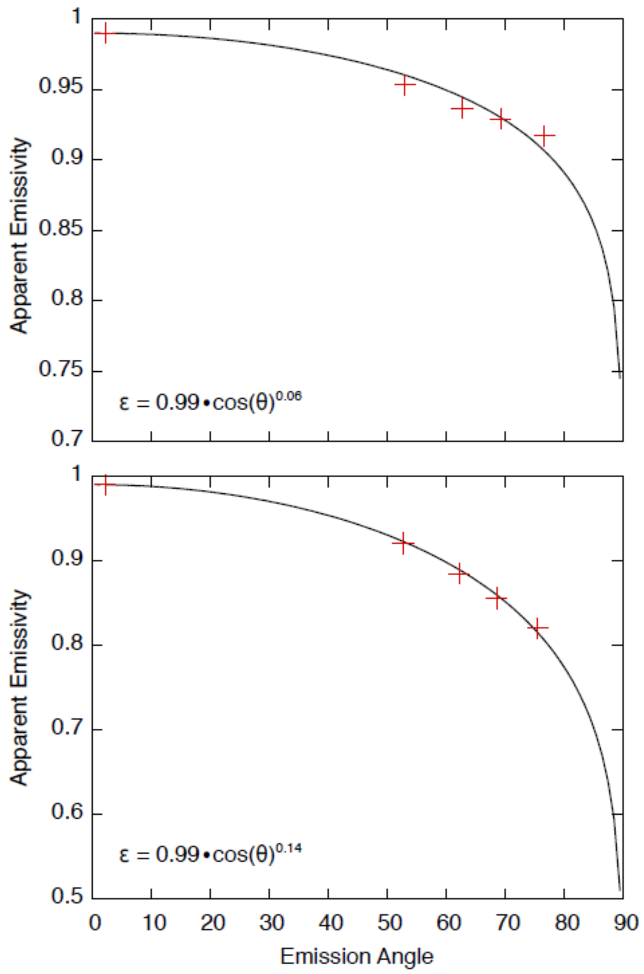

Figure 100: Diviner broadband apparent emissivity as a function of emission angle (red crosses) for daytime (top) and night-time (bottom) DE observations. Nadir emissivity is assumed to be 0.99. The equations (black lines) are fits to the data. Taken from (Bandfield et al. 2015).

The increased distance and the oblique projection of the measurement FOV on the surface result in a much larger FOV footprint at increased emission angles. For example from the 50 km LRO mapping orbit, the projected FOV on the surface grows to ~650 m by 1320 m at an emission angle of 76^o compared to 160 m by 320 m at 0^o. As a consequence only target areas that were relatively homogeneous in composition and flat in topography were chosen. Two broadband DE measurements were made, one during the daytime and one during the night-time. The DE measurement for the daytime was made using Diviner channels B3 – B9 (8 – 400 µm). The DE measurement for the night-time was made only using channels B6 – B9 (25 – 400 µm) as there was no signal in channels B3 – B5 (8 µm channels) due to the cold surface (<100 K) temperatures of night-time. The lunar soil was assumed to have an emissivity of 0.99 between (8 – 400 µm), consistent with laboratory measurements of emission spectra of lunar samples (Salisbury et al. 1997).

It can be seen that the emissivity decreases with increasing emission angle in both the night-time and daytime measurements. However, the night-time emissivity measurements decrease more quickly with emission angle than the daytime emissivity (Figure 100). The difference between the night-time and daytime measurements could be due to problems with the Diviner channels 8 and 9. In these channels there is potentially a source of extra radiance present that interferes with the analysis of acquired measurements (Bandfield et al. 2015). The difference could also be due to the lunar surface cooling down during the night-time measurements.

The DE of JSC-1AF measured by the OSEG is compared to the broadband measurement made by the Diviner instrument of the lunar soil in Figure 101. The measurement made by OSEG of JSC-1AF has been re-calibrated such that the normal emissivity is 0.99. This was done to allow easy comparison between the two measurements, as the Diviner measurement was calibrated in a similar way to the OSEG measurements but to a normal emissivity of 0.99. It can be seen that the measured DE of the lunar soil fails more sharply with emission angle than the night-time measured DE of JSC-1AF, but less sharply than the daytime measurement (Figure 101). This could be due to a number of reasons:

- The optical constants of the lunar soil is different to that of JSC-1AF.
- The millimetre-micrometre surface roughness of the lunar soil is different to the sample of JSC-1AF measured.
- The large scale roughness (>1 m) has an effect on the DE.
- The Diviner DE measurement was made in a wavelength region that rolled off ~400 μm compared to the 25 μm for the OSEG DE measurement. Different scattering regimes may dominate at longer wavelengths.

Future measurements of Apollo soils in the OSEG will help narrow down possible reasons. The most likely explanation is that large scale surface roughness does have an effect on the DE.

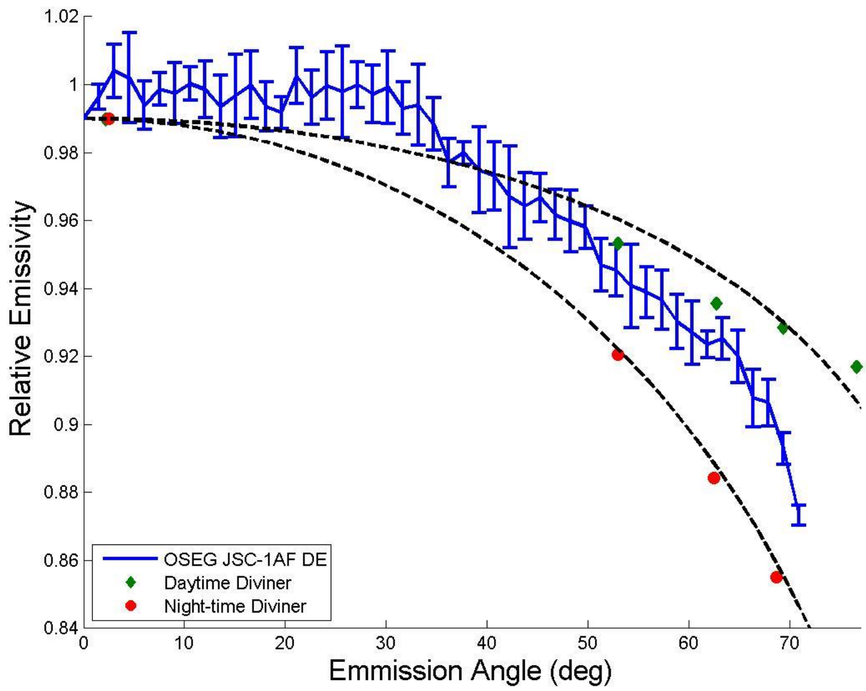

Figure 101: Comparison between the measured DE for JSC-1AF and the broadband night-time diviner measurement of DE of the lunar surface. The OSEG measured DE of JSC-1AF has been scaled so that the normal emissivity is 0.99 to allow comparison.

8.7 Summary of Broadband DE measurements and models of JSC-1AF

The broadband DE of JSC-1AF has been measured and shown to be anisotropic under ambient pressure. This is a significant result for three dimensional thermal physical models that try to reproduce the surface temperature of airless bodies and assume that surfaces re-radiate isotropically. Compared to an isotropic emitter the emissivity of JSC-1AF is 0.04 different at an emission angle of 45^o and 0.1 different at an emission angle of 70^o.

The measured DE has been modelled using the Monte Carlo ray-tracing technique. Using a Matlab constrained least squares fitting algorithm the roughness profile of the JSC-1AF sample was estimated to be $H_{rms} = 15\ \mu m$ and $\tau = 100\ \mu m$. The Hapke DE model (described in section 1.5.2) also fits the measured DE well (R^2 of 0.91). Using a Matlab unconstrained fitting algorithm the Hapke DE model suggests a single scattering albedo between 0.49 and 0.51 that compares remarkably well to previously measured single scattering albedos of JSC-1AF (0.4385) (Gaier et al. 2011).

The measured DE of JSC-1AF is in good qualitative agreement with broadband DE measurements of the lunar surface (Figure 101). However there are some quantitative differences between the two measurements. More measurements are required to understand these differences, but if there are differences between the small scale (millimetres) laboratory DE measurements and the large scale (hundreds of meters) measurements of the lunar surface that would suggest large scale surface roughness features dominate the DE. This could be further investigated by measuring the DE of an Apollo soil sample to rule out small-scale roughness.

9 Applying the Measured DE to Three Dimensional Thermal Physical Models

With the initial DE measurements of JSC-1AF completed the next step is to apply these measurements to three dimensional thermal physical models of airless bodies. The Advanced ThermoPhysical Model (ATPM) is one such three dimensional thermal physical model that can be used to model the surface temperature of any airless body and has primarily been used to investigate the surface temperatures of asteroids (Rozitis & Green 2011). It is similar to the three dimensional thermal physical model described in section 1.3 that has globally modelled the temperature of the lunar surface (e.g. Paige et al. (2010)).

The ATPM was originally developed to interpret thermal-infrared observations of planetary surfaces without an atmosphere (Rozitis & Green 2011), in particular the thermal inertia and bulk density of asteroids (e.g. 1950 DA) (Rozitis & Green 2012). The model was verified by making accurate interpretations of the thermal infrared observations of the moon (Rozitis & Green 2011). and has successfully interpreted the thermal and physical properties of asteroid surfaces Apollo (Rozitis et al. 2013) and Bennu (Chesley et al. 2014) from thermal infrared observations.

To summarise how it works the ATPM uses a mesh to grid the surface into elements, the surface temperature of each element is calculated by solving the one dimensional heat conduction with a surface boundary condition that includes direct and multiply scattered sunlight, shadowing and re-absorbed thermal radiation from interfacing surface elements. Like the Paige et al. (2010) model, the ATPM also assumes that the surface of the airless body emits in an isotropic fashion. In this section the ATPM is used to compare the difference between the modelled surface temperature distribution inside an imaginary PSR (permanently shadowed region) near the pole of the Moon assuming isotropic emission and more realistic DE's similar to the measured DE of JSC-1AF in section 8.

Three dimensional thermal physical models divide the surface into facets usually based on triangles. The emission from a surface element is calculated as:

$$E = \varepsilon_d(\theta_e) * \cos(\theta_e) \qquad (48)$$

Where E is the radiance emitted by the surface element, ε_d is the DE and $\theta_e$is the emission angle. For isotropic emission ε_d is equal to the normal emissivity for all emission angles and the emission from the surface element is therefore dependent only on $\cos(\theta_e)$. When the DE is approximated using a cosine power law the emission from a surface element becomes:

$$E = \varepsilon_n cos^x(\theta_e) \quad \mathbf{49}$$

Where the DE is approximated as $\varepsilon_d(\theta_e) = \varepsilon_n cos^{1-x}(\theta_e)$, x is the cosine power and ε_n is the normal emissivity. Isotropic emission occurs when $x = 1$. The DE measurement of JSC-1AF has been modelled using a cosine law to allow for easy integration into three dimensional thermal physical models (Figure 102).

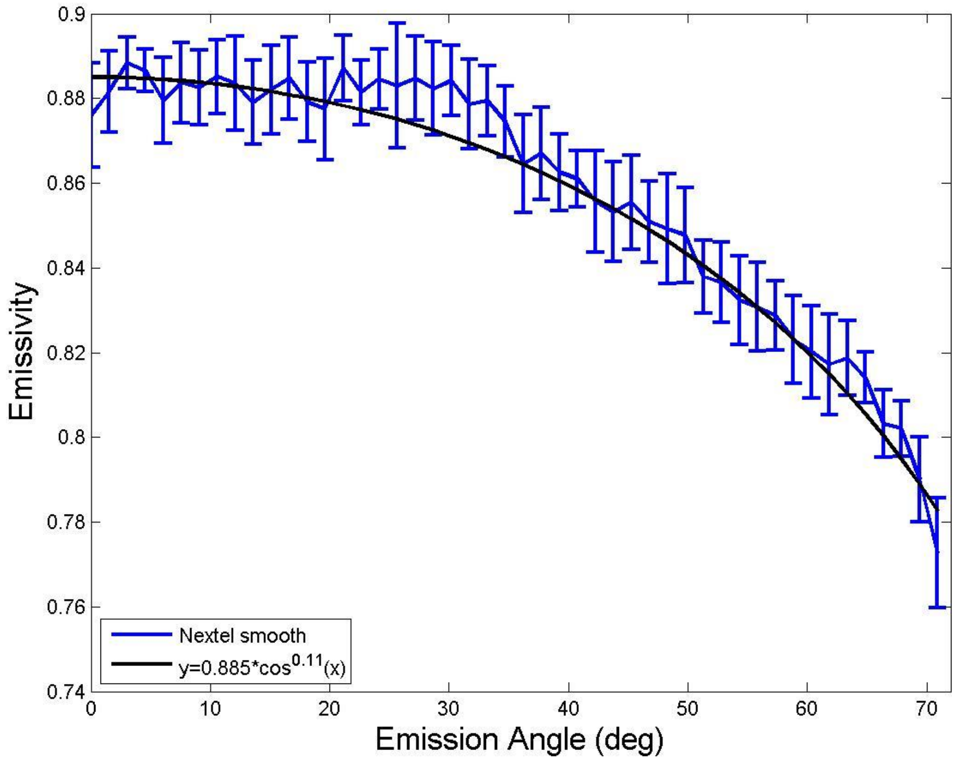

Figure 102: Best fit cosine power law to the measured DE of the JSC-1AF sample. The best fit was found using an unconstrained Matlab least squares fitting algorithm with the cosine power as a free parameter.

Serval ATPM model runs were carried out by B. Rozitis (Open University, UK) to investigate how the changes in the assumed scattering affect the temperature distribution of a lunar-like bowl shaped crater. The ATPM utilised a low resolution (131 facets) crater shape model that was sufficient to show the changes in the surface temperature distribution assuming different cosine powers for the DE. The modelled assumed a lunar-like thermal inertia of 50 $Jm^{-2}K^{-1}s^{-1/2}$ and the model was run until the temperature difference between each time step was less than 0.01 K (taking roughly 50 – 100 steps to converge). The model also assumed a lunar-like normal emissivity of 0.89 and used a static solar position (the sun was facing the right hand side carter wall in Figure 103) to generate a permanently shaded region, as found at the lunar poles. The modelled surface temperature distribution inside a bowl shaped crater assuming isotropic scattering is shown in Figure 103. Two further modelled surface temperature distributions assuming higher cosine powers of scattering are shown in Figure 104.

9.1 ATPM Model Results

The modelled surface temperatures within the crater get increasingly colder as the cosine power increases above unity (isotropic scattering). However, the surface temperature difference is less at the crater walls than at the crater base. The cosine law fitted to the measured DE of JSC-1AF would suggest that the base of the PSR could be ~>10 K colder than the surface temperature modelled assuming an isotropic scattering. This is an important result, as it shows there are significant differences between assuming isotropic scattering and realistic scattering in three dimensional thermal physical models of surface temperatures on airless bodies. With further measurements of the DE of lunar samples and analogue materials three dimensional thermal physical models can be significantly improved.

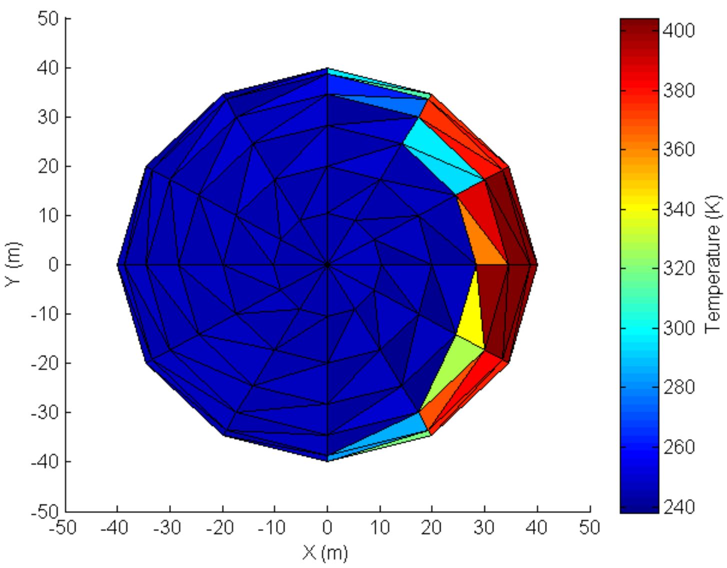

Figure 103: ATPM surface temperature distribution inside a crater assuming isotropic scattering near the terminator. After (Rozitis 2011)**.**

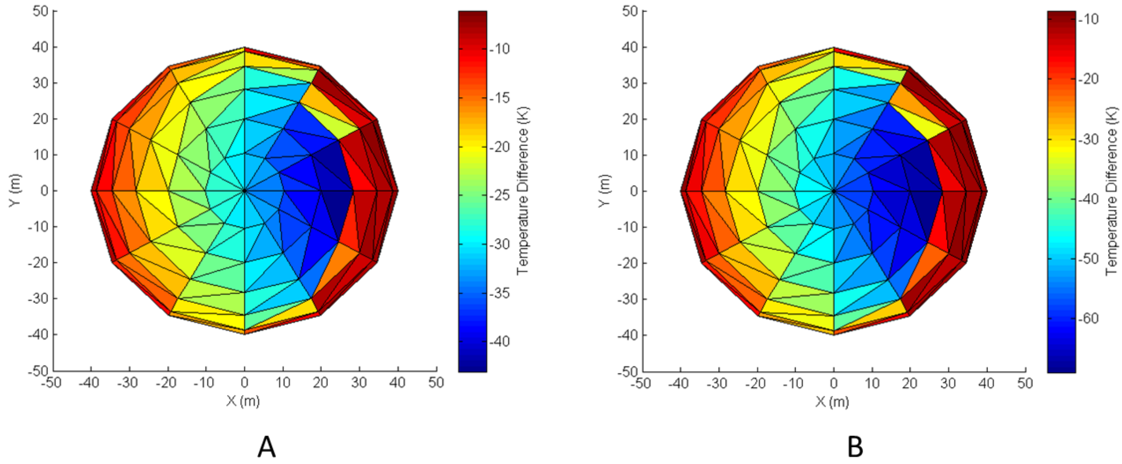

Figure 104: Difference in predicted surface temperature inside a crater for a three dimensional thermal physical model (ATPM) assuming isotropic ($\cos(\theta_e)$) and non-isotropic scattering. (A) shows the difference between isotropic ($\cos(\theta_e)$) and $\cos^2(\theta_e)$ scattering. (B) shows the difference between isotropic and $\cos^3(\theta_e)$. After (Rozitis 2011)**.**

10 Summary and Conclusions

Three dimensional thermal physical models require realistic phase functions across wavelengths from the visible to the far infrared to accurately predict the surface temperatures of airless bodies. Although there have been many phase function measurements of suitable analogue materials in the visible, there have been no equivalent measurements made in the thermal infrared. To fill this gap a goniometer has been designed and constructed that is able to make phase function measurements of powdered samples from the visible to the far infrared. The setup has been validated by measuring targets with known phase functions, such as the BRDF of the reference target Spectralon and comparing to measurements made by established goniometer systems (such as the PHIRE and BUG).

Thermal infrared DE measurements of Nextel painted surfaces have shown that the DE is dependent on the optical properties and the surface roughness of the medium. Surface roughness down to order 10 μm scale has an effect on the DE. A DE model must include multiple scattering between surfaces to accurately model the DE of a rough surface. Simplified models such as the Hapke thermal emission model and a model based on geometric optics using the Fresnel equations do not fit the measured DE of Nextel paint (R^2 <0.66). Only when the Fresnel model is incorporated with a Monte Carlo ray-tracing technique that accounts for the multiple scattering between surfaces can the measured DE of Nextel be modelled accurately (R^2 >0.99).

The DE of the lunar analogue material JSC-1AF was measured and shown to be similarly anisotropic. Coupled with the measurements of Nextel, this is a very important result that needs to be included in three dimensional thermal physical models that try to recreate the surface temperature distributions on airless bodies. This work shows that the assumption that the regolith of the airless body is an isotropic emitter is incorrect and could lead to inaccuracies of up to 10 K in modelled surface temperatures. For example if the measured JSC-1AF DE function was used instead of assuming the regolith was an isotropic emitter then surface temperatures could be reduced in some regions depending on the local topography.

This could explain the 15 – 20 K difference between the lunar surface night-time temperatures that are modelled using a three dimensional thermal physical model and the observed surface temperatures by the Diviner radiometer (Paige et al. 2010). In a simulated crater at the lunar pole the surface temperature at the base of the crater was found to be ~10 K colder when modelled using non-isotropic scattering compared to isotropic scattering. However further investigation is required to fully understand the difference. Topographical information about the night-time lunar surface temperatures that are both underestimated and overestimated by the three dimensional thermal physical model are required. For example if the model is systematically overestimating the temperatures of PSR regions, then using the measured DE instead of isotropic emission would improve the model.

Currently the OSEG setup can only heat samples from below and does not have an illumination source for DE measurements. Therefore the DE data presented in this thesis is only applicable to modelling the night-time DE (i.e when there is no illumination on the lunar surface). DE measurements of illuminated surfaces are required to investigate the ~15 K underestimation of the daytime surface temperatures in PSR by the three dimensional model.

11 Suggestions for Future Work

The next major step is measuring the broadband DE of samples by heating them from above using an illumination source. Illuminating the surface with a light source will create a temperature gradient across the sample that could change the DE of the sample compared to heating from below. Due to the inherent surface roughness of the sample illuminating it at a particular phase angle will preferentially heat slopes that face the light source to a greater temperature than slopes that face away from the light source. This will create an opposition effect similar to that described in section 1.5.3. Hapke states that a thermal infrared opposition effect cannot occur on the lunar surface as the thermal conduction of the lunar soil is too great (Hapke 2014). However, it was found that across the 3 mm depth of the lunar simulant JSC-1AF sample a temperature gradient of the order 170 K is maintained under vacuum (10^{-6} mbar). This shows that the thermal conductivity of JSC-1AF is low enough to create an appreciable temperature gradient between slopes that are illuminated and slopes that face away from the illumination source. Therefore, a DE thermal opposition effect is expected to be observed with JSC-1AF.

In order to achieve these measurements the goniometer would require a light source. To heat the sample up to 300 K the light source would have to provide >3 W of heating power. As the seen during testing in the visible with the Spectralon target (section 5.1) the measured scattering function is highly dependent on the uniformity of the light source. So the light source would also be required to be uniform and high collimated. Such a light source could be achieved using a high power halogen light filament or high power LED with an aspherical diffuser lens.

As discussed in section 4.6.1 when a light source is installed in the OSEG setup, it is not possible to view at low phase angles as the light source obscures the radiometers view of the sample. There are serval possible solutions to this:

1. A secondary light source could be mounted on the radiometer for use at low phase angles.
2. A 50:50 beam splitter could be used (similar to the setup used on the PHIRE goniometer)
3. It might be possible to align the radiometer behind the light source and then switch the light source off before move it away allowing the radiometer to view the sample. It would then be possible to watch the sample cool and from the cooling curve calculate the radiance when the light source was on.

All DE measurements with the OSEG have been made with broadband wavelength selection (0.2 – 25 μm). It would be interesting to investigate the DE of lunar analogue powders using the Diviner filters for wavelength selection, particularly the Diviner 8 µm filters with the illumination source installed. The 8 µm Diviner filters were designed to characterise the Christiansen feature (CF), a feature found in the emission spectrum of the Moon. It occurs because on the Moon the visible and near infrared incident solar radiation penetrates and heats the top few millimetres of the lunar regolith. The lunar regolith re-radiates the absorbed solar radiation in the thermal infrared, where the absorption depth is much shorter. So only the top few 100 µm of the lunar regolith radiates out to cold space, creating a large (40 – 50 K per 100 µm depth) thermal gradient in the top ~500 µm of the lunar soil. The CF is an emissivity maximum or reflectivity minimum feature in the IR emission spectrum. It is formed when the more transparent thermal infrared radiation from hotter layers deeper (due to the thermal gradient) within the surface are able to radiate out (

Figure 105). Hence different temperatures are effectively observed at different wavelengths and as the surface is assumed to be isothermal in temperature the emissivity appears to increase. The DE around the CF could be very different compared to the broadband DE as at different emission angles the radiometer could be expected to sound to different depths.

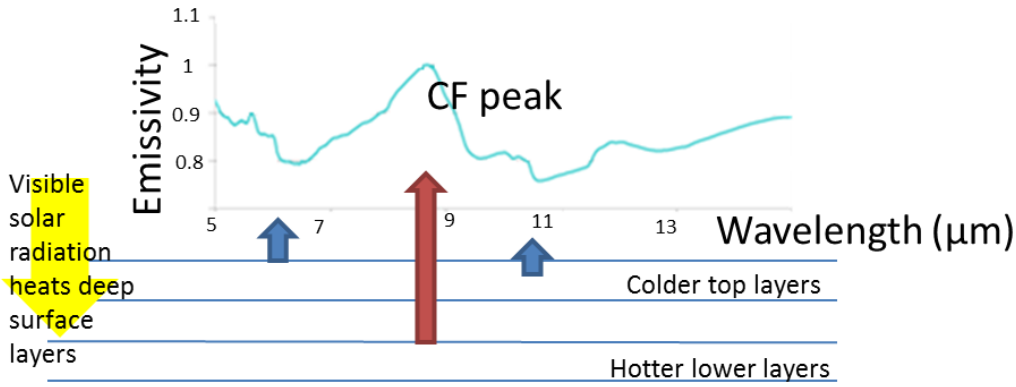

Figure 105: The effective emissivity of non-isothermal sample is affected by its transparency. The solar radiation heats the top few millimetres of the lunar soil at short wavelengths and is re-emitted from the top few hundred microns at longer wavelengths. The CF is where the medium is more transparent and radiation from the deeper hotter layers radiates out increasing the measured emissivity. After (Thomas 2012)

Further investigation of the effect of surface roughness on the DE would also be very interesting. In section 6.1.10 it was shown that there is a significant difference between the measured DE of a smooth Nextel painted surface and a rough Nextel painted surface. A set of machined targets could be made that have different roughness parameters on millimetre scales. These could then be spray painted black to investigate how the surface roughness affects the DE.

The emission angular range of the goniometer could be extended by anguarling the input mirror of the radiometer carriage. From the CAD model of the goniometer this would increase the emission angular range by 10^o, from 75^o to 85^o. However, the semi major axis of the radiometers FOV increases inversely proportional to the cosine of the emission angle. Currently the FOV is a circle with diameter 10 mm at 0^o emission angle and therefore at 85^o emission angle the sample would need to at least 115 mm in diameter.

The wavelength range of the goniometer could be extended by removing the KBr window on the front of the detector can, this would then allow the longer wavelength Diviner filters (B3-6) to be used.

To further develop this project a 3D Thermal physical model will be required, this will then allow how the thermal emission of the surface influences the surface temperature distribution of an airless body to be fully investigated.

11.1 Applications to Future Missions

The need for DE measurements in the thermal infrared is currently required to help support measurements being made by the Diviner radiometer. However, in the coming few years several new missions flying thermal infrared spectrometers are being launched and these will increase the demand for thermal infrared DE measurements. For example the OSIRIS-REx mission is due to rendezvous with the carbonaceous asteroid Bennu (101955) in 2018 (Lauretta & Team 2012; Chesley et al. 2014). The OSIRIS-REx mission will attempt to fly close enough to Bennu to deploy a robotic arm to retrieve a sample of its regolith. The spacecraft includes a comprehensive suite of remote sensing instruments with both visible and near infrared (OVIRS, 0.4 – 4.3 μm) and thermal infrared (OTES, 4 – 50 μm) (Lauretta & Team 2012). Sample acquisition will be a delicate procedure and the thermal stability of the spacecraft will be critical during proximity operations near the asteroid. DE measurements of carbonaceous meteorite samples are therefore urgently required to allow the thermal load on the spacecraft to be accurately modelled using three dimensional thermal physical models generated from the remote sensing instrument datasets.

The Bepicolombo mission is due to launch 2017 to Mercury with the IR spectrometer MERTIS on-board (Hiesinger & Helbert 2010). One of the main science goals of the thermal infrared MERTIS (7 – 40 μm) instrument is to globally map the surface temperature of Mercury (Hiesinger & Helbert 2010). Like the Moon, Mercury has a very low axial tilt and PSR’s exist at its poles (Zhang & Paige 2009; Paige et al. 2013). Such regions have very low surface temperatures and to accurately model the surface temperatures using three dimensional thermal physical models would require realistic DE functions that could be measured by using Mercury analogue samples in the OSEG.

12 References

Arnold, J., 1979. Ice in the Lunar Polar Regions. *Journal of Geophysical Research: Solid Earth*, 84(9).

Bandfield, J.L. et al., 2011. Lunar surface rock abundance and regolith fines temperatures derived from LRO Diviner Radiometer data. *Journal of Geophysical Research*, 116, p.E00H02.

Bandfield, J.L. et al., 2015. Lunar surface roughness derived from LRO Diviner Radiometer observations. *Icarus*, 248, pp.357–372.

Bergström, D., 2012. Mysimlabs. Available at: http://www.mysimlabs.com/ [Accessed January 25, 2015].

Bergström, D., Powell, J. & Kaplan, a. F.H., 2007. A ray-tracing analysis of the absorption of light by smooth and rough metal surfaces. *Journal of Applied Physics*, 101(11).

Bergström, D., Powell, J. & Kaplan, H., 2008. The absorption of light by rough metal surfaces-A three-dimensional ray-tracing analysis. *Journal of Applied Physics*, 103(10).

Bohren, C. & Huffman, D., 1998. *Absorption and Scattering of Light by Small Particles*, Wiley-VCH Verlag GmbH and Co.

Bryson III, E., Cazcarra, V. & Levenson, L., 1974. Sublimation rates and vapor pressures of H2O, CO2, N2O, and Xe. *J. Chem.*, 19, pp.107–110.

Carpenter, P. et al., 2006. Characterization of Standard Lunar Regolith Simulant

Materials. *NIST Particle Workshop April 2426*, (2004), p.9.

Chesley, S.R. et al., 2014. Orbit and bulk density of the OSIRIS-REx target Asteroid (101955) Bennu. *Icarus*, 235(September 1999), pp.5–22.

Chin, G. et al., 2007. Lunar reconnaissance orbiter overview: The instrument suite and mission. *Space Science Reviews*, 129(4), pp.391–419.

Clarke, F., 1997. *Certificate of Calibration Hemispherical, diffuse and regular spectral reflectances of one sample*,

Donaldson Hanna, K.L. et al., 2012. Thermal infrared emissivity measurements under a simulated lunar environment: Application to the Diviner Lunar Radiometer Experiment. *Journal of Geophysical Research*, 117(V), p.E00H05.

Duke, M.B. et al., 2006. Development of the Moon. *Reviews in Mineralogy and Geochemistry* , 60 (1), pp.597–655.

Finckenor, M.M. & Dooling, D., 1999. *Multilayer Insulation Material Guidelines*,

FLIR-Systems, 2012. Technical Data FLIR i50. , 1, pp.1–2. Available at: http://support.flir.com/DsDownload/Assets/39903-1301_en_40.pdf [Accessed September 7, 2015].

Foote, E. & Paige, D., 2009. The Bidirectional Reflectance of Apollo 11 Soil Sample 10084. *Lunar and Planetary*, pp.3–4.

Gaier, J.R., Ellis, S. & Hanks, N., 2011. Thermal Optical Properties of Lunar Dust Simulants and Their Constituents. *American Institute of Aeronautics and Astronautics*, (June), pp.1–11.

Garcia, N. & Stoll, E., 1984. Monte Carlo Calculation for Electromagnetic-Wave Scattering from Random Rough Surfaces. *Physical Review Letters*, 52(20), pp.1798–1801.

Glotch, T.D. et al., 2011. The Mairan domes: Silicic volcanic constructs on the Moon. *Geophysical Research Letters*, 38(21), p.n/a–n/a.

Greenhagen, B., 2015. LRO Diviner: Viewing the Moon in a Different Light. *EPSC*, 10(380), pp.1–2.

Greenhagen, B.T. et al., 2010. Global silicate mineralogy of the Moon from the Diviner lunar radiometer. *Science (New York, N.Y.)*, 329(5998), pp.1507–1509.

Hamamatsu Photonics, 2010. Infrared LED L10660 Datasheet. Available at: https://www.hamamatsu.com/resources/pdf/ssd/l10660_series_kled1055e.pdf [Accessed April 4, 2015].

Hapke, B., 2014. *Theory of reflectance and emittance spectroscopy*, Cambridge University Press.

Hapke, B., 1993. *Theory of Relectance and Emission Spectroscopy*, Cambridge University Press.

Hapke, B. & Van Horn, H., 1963. Photometric Studies of Complex Surfaces, With Applications To the Moon. , 68(15).

Hapke, B.W., 1968. On the particle size distribution of lunar soil. *Planetary and Space Science*, 16(1), pp.101–110.

Hapke, B.W., 1964. Packing properties of fine powders and the depth of the lunar dust layer. , 69(6), pp.1147–1151.

Hapke, B.W., Nelson, R.M. & Smythe, W.D., 1998. The Opposition Effect of the Moon: Coherent Backscatter and Shadow Hiding. *Icarus*, 133, pp.89–97.

Helfenstein, P. & Shepard, M.K., 1999. Submillimeter-Scale Topography of the Lunar Regolith. , 131, pp.107–131.

Helfenstein, P. & Shepard, M.K., 2011. Testing the Hapke photometric model: Improved inversion and the porosity correction. *Icarus*, 215(1), pp.83–100.

Hiesinger, H. & Helbert, J., 2010. The Mercury Radiometer and Thermal Infrared Spectrometer (MERTIS) for the BepiColombo mission. *Planetary and Space Science*, 58(1-2), pp.144–165.

InfraTec, 2015. LIE-332F Datasheet. , pp.1–2. Available at: http://www.infratec.de/fileadmin/media/Sensorik/pdf/LIE-332f.pdf [Accessed December 13, 2014].

Johnson, J., 2008. Spectrogoniometric measurements and models of Lunar analog soils. *Lunar and Planetary*, pp.2–3.

Johnson, J. & Shepard, M., 2009. Spectrogoniometric measurements and modeling of Apollo 11 Soil 10084. *Lunar and Planetary*, (2009), pp.4–5.

Johnson, J.R. et al., 2013. Spectrogoniometry and modeling of martian and lunar analog samples and Apollo soils. *Icarus*, 223(1), pp.383–406.

Kauder, L., 2005. *Spacecraft Thermal Control Coatings References*,

Keihm, S.J. & Langseth, M.G., 1973. Surface brightness temperatures at the Apollo

17 heat flow site - Thermal conductivity of the upper 15 cm of regolith.

Koirala, L.R., 2004. *FTIR-Spectroscopic Measurement of Directional Spectral Emissivities of Microstructured Surfaces*. University of the Federal Armed Forces Hamburg.

Labsphere, 2012. Spectralon Datasheet. Available at: www.labsphere.com [Accessed January 10, 2014].

Lauretta, D. & Team, O., 2012. An Overview of the OSIRIS-REx Asteroid Sample Return Mission. *Lunar and Planetary Institute Science*, pp.5–6.

Lide, D.R., 1993. *CRC Handbook of Chemistry and Physics* 74th ed., CRC Press.

Lohrengel, J., 1987. Gesamtemissionsgrad von Schwiirzen. *Springer-Varlag*, 21, pp.311–315.

LROC team, 2014. South Pole Illumination Map. , (27/08). Available at: http://lunarsceince.nasa.gov/articules/lroc-produces-south-pole-illumination-map/.

McKay, D. et al., 1991. The lunar regolith. In *Lunar sourcebook*. pp. 285–356.

Millán, L., Thomas, I. & Bowles, N., 2011. Lunar regolith thermal gradients and emission spectra: Modeling and validation. *Journal of Geophysical Research*, 116(E12), p.E12003.

Moses, J.I. & Nash, D.B., 1991. Phase transformations and the spectral reflectance of solid sulfur - Can metastable sulfur allotropes exist on Io? , 304, pp.277–304.

NASA, 1972. Image of Apollo 17 landing site. Available at:

http://science.nasa.gov/science-news/science-at-nasa/2000/as17mar_1m/ [Accessed August 2, 2014].

Paige, D. et al., 2010. Diviner Lunar Radiometer Observations of Cold Traps in the Moon’s South Polar Region. *Science (New York, N.Y.)*, 330(6003), pp.479–82.

Paige, D., 2015. Diviner Maps and Data. *Diviner Website*. Available at: http://www.diviner.ucla.edu/map_gallery.shtml [Accessed September 6, 2015].

Paige, D. et al., 2009. The Lunar Reconnaissance Orbiter Diviner Lunar Radiometer Experiment. *Space Science Reviews*, 150(1-4), pp.125–160.

Paige, D.A., Wood, S.E. & Vasavada, A.R., 2013. The Thermal Stability of Water Ice at the Poles of Mercury. , 258(5082), pp.643–646.

Pieth, S. & Kohler, U., 2009. *Our Solar System*, German Aerospace Center.

Polytec Limited, 2015. TopSens Series Confi gurable Chromatic Confocal Point Sensors Datasheet. Available at: www.polytec.com [Accessed September 25, 2015].

Pommerol, a. et al., 2011. Photometry and bulk physical properties of Solar System surfaces icy analogs: The planetary ice laboratory at university of Bern. *Planetary and Space Science*, 59(13), pp.1601–1612.

Reed, B.E., 2013. *Aerosol Optical Properties Second Year Report AOPP*,

Robinson, S.R., 1993. *The Infrared and Electro-Optical Systems Handbook*,

Rozitis, B. et al., 2013. A thermophysical analysis of the (1862) Apollo Yarkovsky and YORP effects. *Astronomy & Astrophysics*, 555, p.A20.

Rozitis, B., 2011. *Physical and Dynamical Characterisation of Near Earth Asteroids via Thermophysical Modelling*. The Open University.

Rozitis, B. & Green, S., 2012. The influence of rough surface thermal-infrared beaming on the Yarkovsky and YORP effects. *Monthly Notices of the Royal Astronomical Society*, 423(1), pp.367–388.

Rozitis, B. & Green, S.F., 2011. Directional characteristics of thermal-infrared beaming from atmosphereless planetary surfaces - a new thermophysical model. *Monthly Notices of the Royal Astronomical Society*, 415(3), pp.2042–2062.

Salisbury, J., Basu, A. & Fischer, E., 1997. Thermal infrared spectra of lunar soils. *Icarus*, 139, pp.125–139.

Salisbury, J.W. & Wald, A., 1992. The role of volume scattering in reducing spectral contrast of reststrahlen bands in spectra of powdered minerals. *Icarus*, 128, pp.121–128.

Shepard, M., 2002. Initial results from the Bloomsburg University Goniometer laboratory. *Astrophysics and Space Science Library*, 17815(2002).

Shepard, M.K. & Helfenstein, P., 2007. A test of the Hapke photometric model. *Journal of Geophysical Research*, 112(E3), p.E03001.

Siegler, M. a., Bills, B.G. & Paige, D. a., 2011. Effects of orbital evolution on lunar ice stability. *Journal of Geophysical Research*, 116(E3), p.E03010.

Silva, a a De & Jones, B.W., 1987. Bidirectional Spectral Reflectance and Directional-Hemispherical Sprectal Reflectance of Six Materials used as

Absorbers of Solar Energy. , 15(1987), pp.391–401.

De Silva, A. & Jones, B., 1987. The directional-total emittance at 368 K of some metals, solar absorbers and dielectrics. *Journal of Physics D: Applied Physics*, 20(9), pp.1102–1108.

Stanford Research Systems, 2011. SR830 DSP Lock-in Amplifier Manual. *20/04/2014*, 0. Available at: http://www.thinksrs.com/downloads/PDFs/Manuals/SR830m.pdf.

Tang, K., Dimenna, R. a. & Buckius, R.O., 1996. Regions of validity of the geometric optics approximation for angular scattering from very rough surfaces. *International Journal of Heat and Mass Transfer*, 40(1), pp.49–59.

Thomas, I., 2012. *Measurement of Properties of the Lunar Surface Using the Diviner Lunar Radiometer Experiment on the NASA Lunar Reconnaissance Orbiter*. Oxford University.

Thomas, I.R. et al., 2012. A new experimental setup for making thermal emission measurements in a simulated lunar environment. *The Review of scientific instruments*, 83(12), p.124502.

Vasavada, A. et al., 2012. Lunar equatorial surface temperatures and regolith properties from the Diviner Lunar Radiometer Experiment. *Journal of Geophysical Research E: Planets*, 117(4), pp.1–12.

Vasavada, A.R. et al., 2012. Lunar equatorial surface temperatures and regolith properties from the Diviner Lunar Radiometer Experiment. *Journal of*

Geophysical Research, 117(June 2009), p.E00H18.

Vasavada, A.R., Paige, D.A. & Wood, S.E., 1999. Near-Surface Temperatures on Mercury and the Moon and the Stability of Polar Ice Deposits 1. , 193, pp.179–193.

Ward, W.R., 1975. Past Orientation of the Lunar Spin Axis. *Science* , 189 (4200), pp.377–379.

Watson, K., Murray, B. & Brown, H., 1961. The Behavior of volatiles on the lunar surface. *Journal of Geophysical ...*, 66(9).

Williams, J., 2011. Interpreting LRO Diviner surface temperatures : Modeling lunar re- golith thermophysical properties and topography in three-dimensions. *Lunar and Planetary ...*, pp.2–3.

Zhang, J.A. & Paige, D. a., 2009. Cold-trapped organic compounds at the poles of the Moon and Mercury: Implications for origins. *Geophysical Research Letters*, 36(16), p.L16203.

Appendix 1 Motor control board Circuit Diagram

PIC690's were used with custom code to control the stepping of all five motors on the OSGE. A main controller PIC690 was used to interface via RS232 with a computer. It was then serially connected to five different motor control PIC690's each one controlling a single stepper motor.

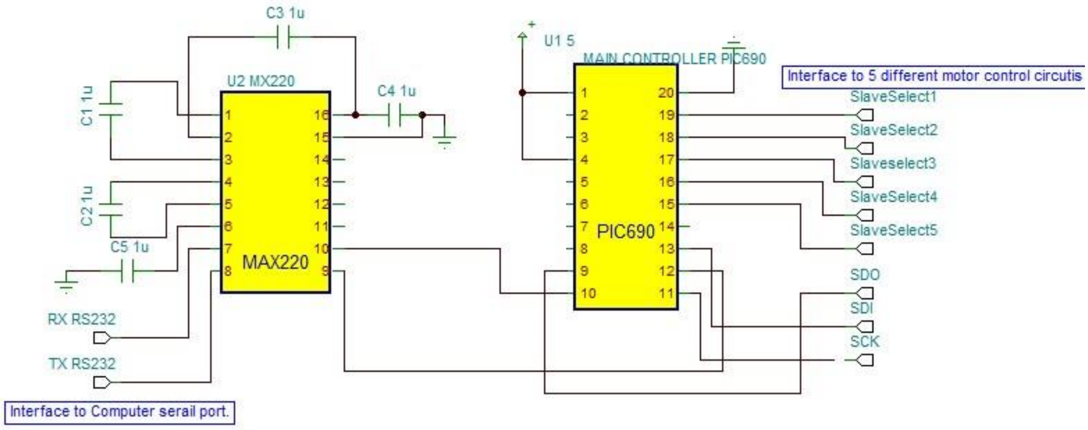

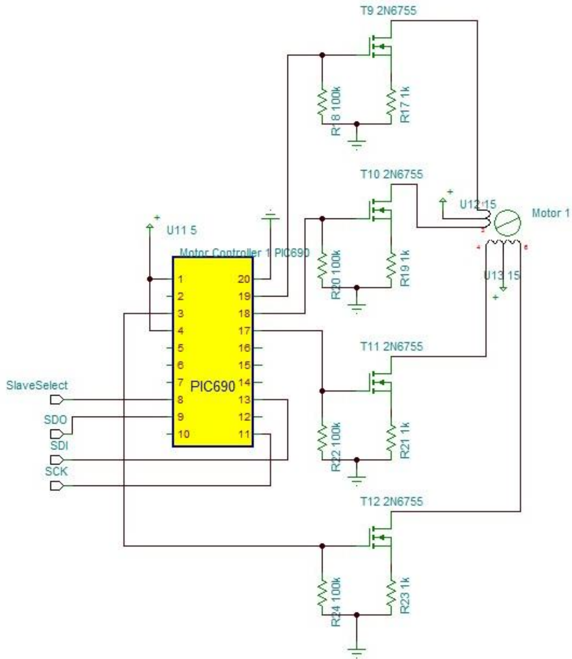

Appendix 2 Pre-amplifier Circuit Diagram

The Source, Drain GND/Casing are all output pins from the detector and the output pin from the pre-amp is connected to the input of the lock-in amplifier.

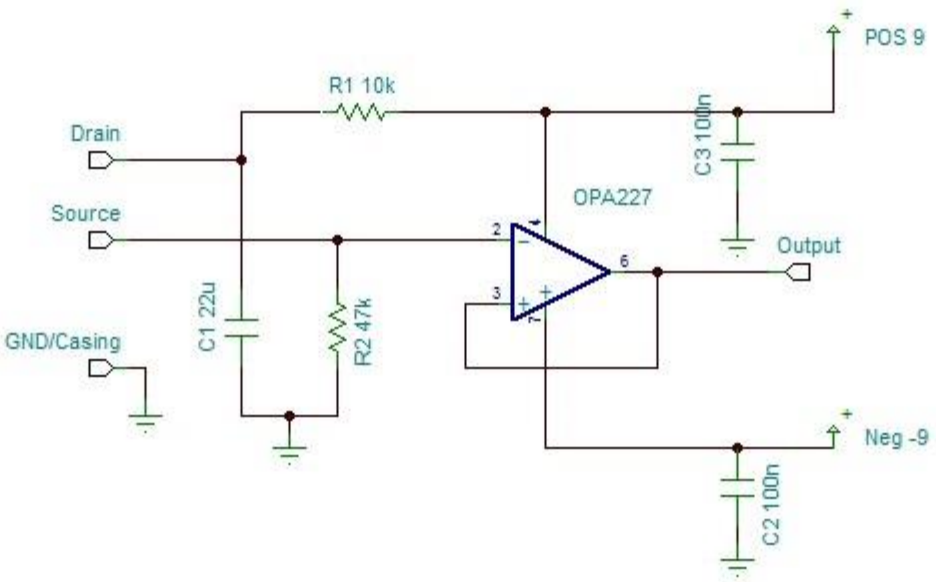

Appendix 3   PID controller Circuit Diagram

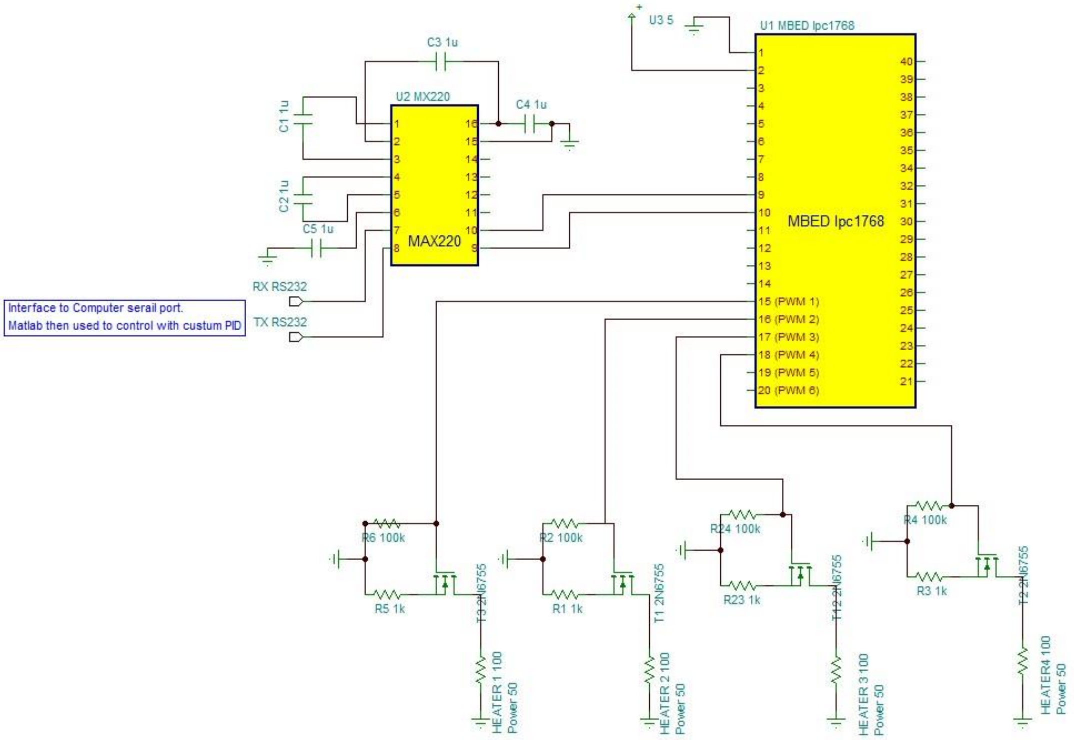

Appendix 4 CAD drawing of Radiometer carriage and filter wheel

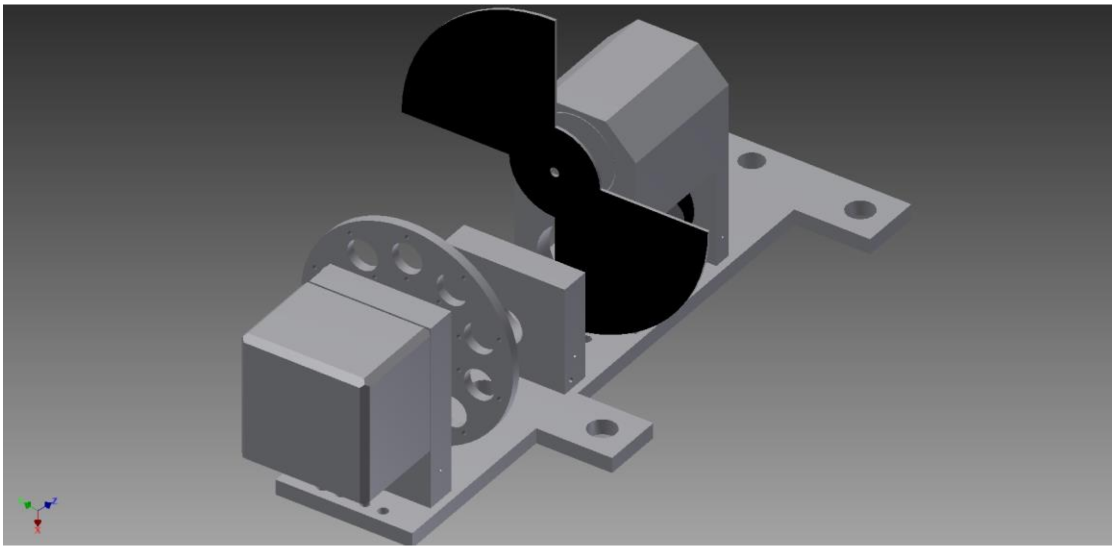

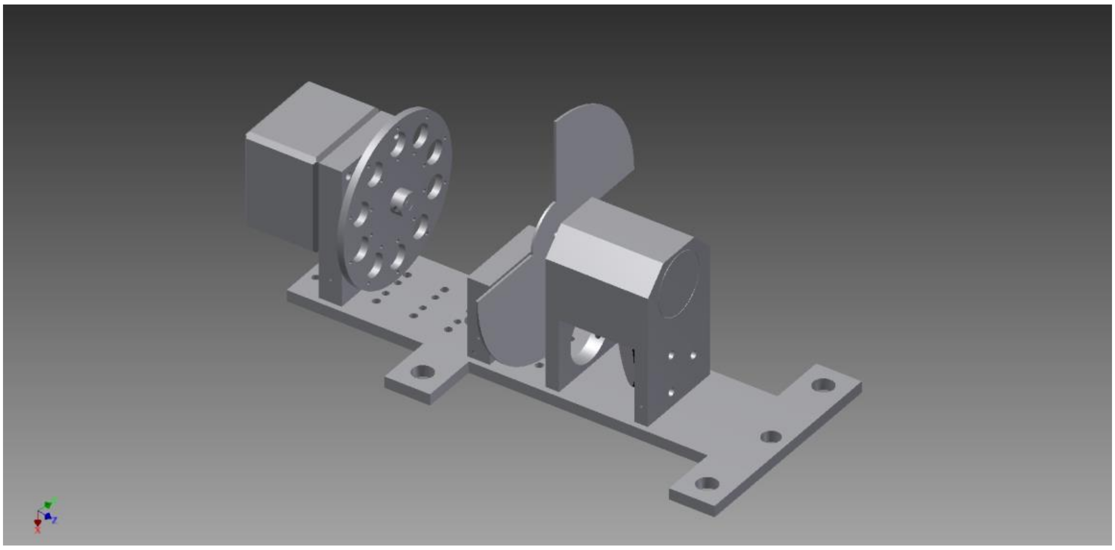

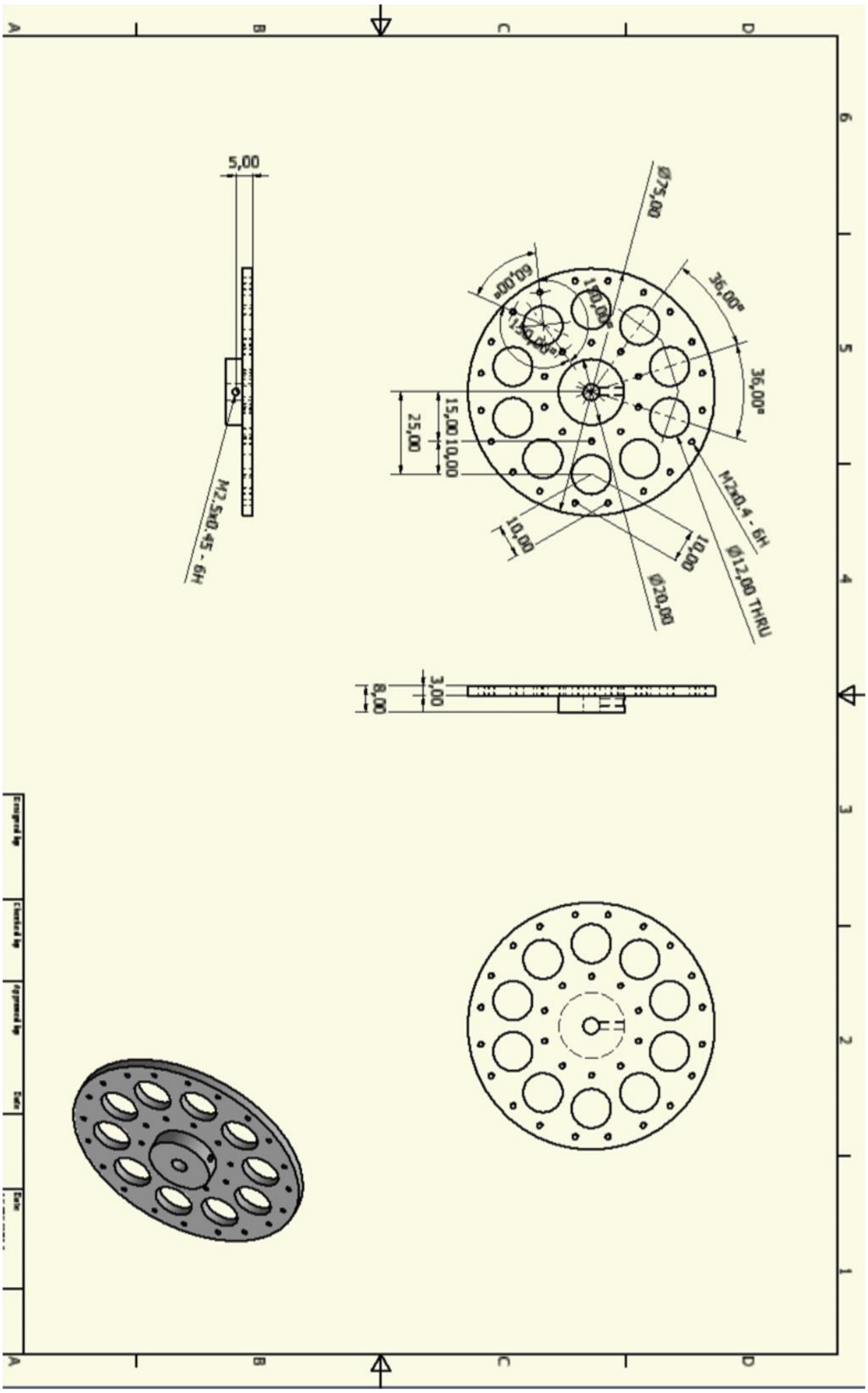
5,00
Ø75,00
36,00°
36,00°
60,00°
15,00
10,00
25,00
M2x0.4 - 6H
Ø12,00 THRU
Ø20,00
10,00
10,00
M2.5x0.45 - 6H
3,00
8,00

Appendix 5 Table of Commonly used Symbols

A	Cross-sectional area
$B(\lambda, T)$	Planck function
B_0	Amplitude of Opposition surge
$\bar{B}$	Opposition surge function
B_s	Radiance emitted by sample
$\bar{C}$	Auto covariance function
C_λ	Wavelength dependant constant
C_{AL}	Specific heat capacity of aluminium
D^*	Specific detectivity
$E_{p,i}$	Perpendicular component of the incidence beam
$E_{p,r}$	Perpendicular component of the reflected beam
$E_{s,i}$	Parallel component of the incidence beam
$E_{s,r}$	Parallel component of the reflected beam
E	emitted radiance
E_r	Reflected radiance
$\bar{f}$	Effective focal length of parabolic mirror
H	H function
H_{rms}	Root Mean Squared height
I	Angular intensity
L_{CS}	Length of cold shield
L_i	Irradiance incident
P_{CH}	Cooling power of cold shield
P	Probability function
ΔQ	Radiative power
R_e	Resistance
$\bar{R}$	Responsivity of radiometer instrument in volts per watt per m2
R_m	Reflectivity of mirror
S	Hapke surface roughness function
SNR	Signal to noise
T	Temperature
T_a	Temperature of ambient
T_c	Temperature of chopper
T_m	Temperature of mirror
U_b	Total radiance emitted from a blackbody
V	Voltage
V_{CS}	Volume of cold shield
a	Auxiliary parameter used in the Fresnel Equation
b	Auxiliary parameter used in the Fresnel Equation
e_x	Error term
f	Three term Henyey-Greenstein parameter
g_1	Three term Henyey-Greenstein parameter
g_2	Three term Henyey-Greenstein parameter
h	Angular half width (radians) opposition effect

k	Imaginary part of the index of reflection. The extinction coefficient.
n	Optical constant real part index of refraction
r	BRDF
$\bar{R}$	Reflectance factor
r_p	Reflected perpendicular component
r_s	Reflected parallel component
r_t	Average of perpendicular and parallel components
u	Distance
v	Distance
Δ	Change in
ΔF	Inverse of integration time
Ω	Solid angle
γ	Albedo factor
α_c	Thermal conductivity
ε_c	Emissivity of chopper
ε_{dr}	DE emissivity for the re-radiated
ε_e	Relative Electrical permittivity
ε_{e0}	Electrical permittivity of free space
ε_m	Emissivity of mirror
ε_d	Pure Directional emissivity
ε_s	Emissivity sample
ζ	Surface function
θ	Hapke's Average slope angle
θ_e	Emission angle
θ_i	Angle of incidence
θ_p	Angle of phase
θ_r	Angle of reflection
θ_s	Angle of the slope from the surface normal
θ_t	Angle of refraction
θ_0	Tangent of RMS slope angle
λ	Wavelength
μ	$cos(\theta_r)$
μ_m	$cos(\theta_i)$
μ_m	Relative Magnetic permeability
μ_{m0}	Magnetic permeability of free space
ρ	Density of aluminium
σ	Stephan-Boltzmann constant
σ_{abs}	Absorption coefficient
σ_e	Thermal conductivity
σ_{sca}	Scattering coefficient
τ	Correlation length
ω	Single scattering albedo
ω_f	Angular frequency